Experimental Study on the Response of Fine Sediments

to Wave Agitation and Associated Wave Attenuation

by

Paul Mathisen

Bachelor of Science in Civil Engineering
University of Massachusetts at Amherst
(1984)

Submitted in Partial Fulfillment
of the Requirements for
the Degree of

Master of Science in Civil Engineering

at the

Massachusetts Institute of Technology

September 1989

© Massachusetts Institute of Technology 1989

Signature of Author _____ _ _____
Department of Civi: Engineering
Auȷ ust 14, 1989

Certified by _____
Ole S. Madsen
Professor of Civil Engineering
Thesis Supervisor

Accepted by ___ _____
Ole S. Madsen
Chairman, Department Graduate Committee
Department of Civil Engineering

EXPERIMENTAL STUDY ON THE RESPONSE OF FINE SEDIMENTS
TO WAVE AGITATION AND ASSOCIATED WAVE ATTENUATION

by

PAUL MATHISEN

Submitted to the Department of Civil Engineering
on August 10 in partial fulfillment
of the requirements for the degree of
Master of Science in Civil Engineering

Abstract

In this thesis, results of laboratory experiments are presented with the purpose of exploring the interaction between fine-grained sediments and water waves. These experiments were conducted in a 28-meter-long wave flume with a 10-cm layer of .12-mm silica sand on the bottom, and were intended to complement previous experiments using .20-mm sand, which were presented in M. Rosengaus's Sc.D. Thesis in 1987. In addition, modifications of the experimental setup and extensive accuracy analyses were completed to further verify the results of Rosengaus (1987). The experiments included tests of initiation of motion of sediment under oscillatory flow, the transient response of the sediment bed, and the steady state or fully developed characteristics of wave/sediment interaction for both spectral and monochromatic waves.

The initiation-of-motion characteristics are found to be reasonably well described by Shields criterion, and the transient response of the bed appears to be well characterized by the Relative Shields Parameter for both monochromatic and spectral waves. The fully developed bed for monochromatic waves is found to exhibit the feature of a breakoff. Slightly modified forms of the relationships originally proposed by Stefanick (1979) are found to model bedform geometry, equivalent bottom roughness, and friction factors reasonably well for monochromatic waves. On the other hand, the fully developed bed for spectral waves does not exhibit a breakoff. In addition, a notable difference between the monochromatic and spectral attenuation is apparent. This difference is attributed to the occasional large bottom velocities associated with random waves, which serve to round off the ripple crests and thus reduce their effectiveness as energy dissipators. Therefore, the use of an equivalent monochromatic wave to model spectral bedform geometry and relate this to the spectral attenuation is found to be inappropriate. However, the spectral attenuation is found to be independent of spectral shape. Thus, the representative Shields Parameter is found to be effective in separately characterizing the spectral bedform geometry and the attenuation. Predictive formulas for friction factors and effective roughness for spectral waves propagating over a movable bed of cohesionless sediments are presented.

Thesis supervisor: Ole S. Madsen
Title: Professor of Civil Engineering

ACKNOWLEDGMENTS

Throughout the duration of this research project, Professor Madsen has always been available to answer any questions or provide insight in solving any problems that may arise. In addition, through his outstanding courses and knowledgeable advice, I have learned an immeasurable amount. Certainly, his support and advice have been invaluable and are greatly appreciated.

The assistance of other people who have helped in the successful completion of this project is also appreciated. First, I sincerely thank Mike Rosengaus for taking the time to get me started in the lab. Also, Chris Rehman, the "UROP" student associated with the project, provided much help in completing experiments and analyses. In addition, the work of the laboratory technician, Jack Crocker, was essential in successful operation of the wavemaker system. I also thank Professor Ken Melville, for allowing the use of a great deal of equipment for the project, and Read Schusky, for his expert typing skills needed to complete this thesis. Finally, I sincerely thank both my family and my wife Sue for their unwavering support.

Table of Contents

List of Figures

List of Tables

List of Symbols

A_b	bottom fluid particle excursion amplitude
a	amplitude of surface wave
b	width of flume
C	wave celerity
C_1	constant
C_b	expansion speed of ripple patches
C_g	group velocity
C_m	apparent mass coefficient
D	energy dissipation
D_b	energy dissipation due to bottom friction
d	sediment grain size
E	wave energy
E_f	wave energy flux
E_{PM}	Pierson-Moskowitz spectrum
E_{JON}	JONSWAP deep water spectrum
FDB	fully developed bed
FMM	fast measuring method
f_w	wave friction factor
g	acceleration of gravity
H	wavemaker transfer function
h	water depth
i	imaginary unit
k	wave number
k_b	equivalent roughness of the bed
ker,kei	Kelvin functions of 0th order

k_s	Nikuradse equivalent sand roughness
L	wave length
M_ϕ	mean grain size in ϕ units
$M_{d\phi}$	median grain size in ϕ units
m	slope of the incident wave amplitude along x
m_b	m associated with bottom friction
m_{nl}	m associated with nonlinear energy transfers
m_w	m associate with side wall friction
N	number of frequency components in spectrum simulation
N_{FB}	number of bedforms still experiencing growth behind the ripple patch front
n_1	$c_g/c = \frac{1}{2}(1 + 2kh/\sinh 2kh)$
n_2	$\frac{1}{2}(1 + 2k_f h/\sinh 2k_f h)$
$S_{u_b u_b}$	near-bottom velocity spectrum
$S_{\eta\eta}$	surface amplitude spectrum
S_*	sediment parmeter
s	sediment grain's relative density (ρ_s/ρ)
T	wave period
T_f	Time required to fully develop the bed
t	time
t_f	time required for full development of a single bedform
t_{new}	time required for appearance of a new incipient ripple
U	Ursell parameter
U_b	amplitude of harmonic near bottom horizonatal fluid velocity
U_*	amplitude of harmonic near bottom shear velocity
U_{10}	reference wind velocity (measured 10 meters above water surface)
u_b	near bottom horizontal fluid velocity
x	horizontal coordinate along length of flume

y	horizontal coordinate across width of flume
z	vertical coordinate
α	bedform asymmetry, or in context of a wave spectrum, the Phillip's Constant
α_ϕ	skewness of sediment grain size distribution
β	phase angle
χ	parameter associated with shallow water transformation function for use with JONSWAP spectum
γ	phase angle of H, or in context of JONSWAP spectrum, the peak enhancement factor
Δa	difference in wave amplitude between stations
$\Delta m/\Delta x$	ripple "roundedness" parameter
η	bedform height, or free surface displacement
θ	phase angle for a surface wave (or a frequency component)
κ	Von Karman's Constant
λ	bedform length
ν	fluid kinematic viscosity
ξ	wavemaker displacement
ξ_0	amplitude of harmonic ξ (for the first harmonic)
ρ	fluid density
ρ_s	sediment grain density
σ	standard deviation, or in context of JONSWAP spectrum, the spectral width parameter
σ_ϕ	standard deviation of log-normal sediment grain size distibution
τ_b	bottom shear stress
τ_{bm}	maximum value of τ_b during a wave cycle
ϕ	phase of a surface wave (or frequency component), or grain size in ϕ units ($-\log_2 d$ (in mm))
$\phi(\omega_h)$	Shallow water tranformation function, for use with a JONSWAP spectrum
ψ	Shields Parameter

ψ_c Critical Shields Parameter for initiation of motion

ψ'/ψ_c Relative Shields Parameter

ω radian frequency of wave (or frequency component)

ω_h radian frequency of maximum spectral energy, transformed for propagation into shallow water

Subscripts

BEAT   second harmonic beat

b   break off (in context of $(\psi'/\psi_c)_b$), or bottom or bed

B   bound wave of second harmonic

F   second harmonic free wave

I   incident wave (the first harmonic)

i   frequency component index

in   input signal

max   maximum value

out   output signal

R   reflected wave (first or second harmonic)

rep   representative monochromatic wave

rms   root mean square

T   total

t   transmitted wave

16,50,84   16%, 50%, and 85% of sediment (in weight) coarser than . . .

+   +x side of ripple patch

-        -x side of ripple patch

superscripts

′   associated with skin friction (flat bed)

(1)   first harmonic

(2)   second harmonic

*   modified

1 Introduction

As concerns of global warming increase, fears of rising sea levels will grow. If these fears are realized, coastal erosion and coastal processes resulting in damage to coastal structures will be of the utmost concern. Therefore, knowledge of these coastal processes is tremendously important.

To thoroughly understand near-shore coastal processes, a quantitative description of the wave characteristics is essential. Wave characteristics in the coastal region are determined by a number of physical processes. Normally, the primary energy input is from the wind. Wind-generated waves, or wind waves, propagating into coastal waters are realistically described as random waves and are characterized by a wave spectrum, which expresses the distribution of wave energy over a frequency and directional domain.

As a spectrum of wind waves propagates into shallower waters over the continental shelf, the bottom of the shelf will affect the waves. These bottom effects include such processes as wave shoaling, depth refraction, and energy dissipation due to bottom friction. This bottom friction is extremely important due to the presence of bedforms that appear on the sediment/water interface as a result of the action of waves. These bedforms increase the hydraulic roughness of the bottom, and ensure the development of a turbulent wave boundary layer, resulting in significant energy dissipation and wave attenuation.

Therefore, it is apparent that the response of the sediment bottom to wave agitation and associated wave attenuation can have an important impact on the wave characteristics that may be found in shallow waters. Bearing this in mind, Madsen and Rosengaus completed a two-year investigation of the response of .20-mm silica sand to wave agitation and corresponding wave attenuation. In that study,

relationships were first developed for monochromatic waves. Then wave groups with two wave components, and finally wave spectra were studied. Experiments were designed to characterize initiation of motion, ripple development and wave attenuation over an initially flat bed, and wave/sediment interaction over a fully rippled bed. The results are presented in M. Rosengaus's doctoral thesis, entitled "Experimental Study on Wave Generated Bedforms and Resulting Wave Attenuation," completed in 1987.

While that experimental study provided a tremendous amount of insight into bedform response and wave attenuation, more work was necessary for a number of reasons. First, a number of nagging problems in the experimental setup remained. One of these problems was a software problem and was referred to as the "dropout" problem. In this problem, in an apparently random manner, a single sampled voltage from one of the wave gauges would be skipped or "dropped out" of the sampling record, with the remainder of the record being shifted up one data point because of it. This dropout problem was found to occasionally affect the experimental results, and preempted extensive data quality analysis to ensure acceptable results. Additional concerns included a problem with the wave gauges, in which the voltage readings of the gauges would steadily drift after calibration. Also, a more complete general accuracy analysis of the experimental setup and procedures was necessary. While the effects of these accuracy concerns were minimized using extensive data quality review, additional analyses and improvements were deemed necessary.

In addition to these concerns, another experimental limitation was associated with the wave generation capacity of the wavemaker. This limitation restricted the spectral experiments to those with relatively low spectral energy. A complete characterization of the spectral wave/sediment interaction still required experiments of higher spectral energy. Therefore, modifications to the settings of the wavemaker, along with a recalibration of the wavemaker, were necessary.

Finally, in addition to the limitations and problems associated with the experimental setup noted above, additional experiments had to be completed using sediment with a different, preferably finer, grain size. This was essential because the experiments completed only used one type of sand. To show that the dimensionless parameters defined in Rosengaus's study actually characterize wave/sediment interaction for both monochromatic and spectral waves, experiments using at least two types of sand are necessary.

Therefore, the purpose of this thesis is to answer the questions related to the experimental apparatus and provide additional information regarding the use of existing dimensionless parameters and relationships to characterize wave/sediment interaction. To accomplish this goal, a brief summary of the basic theory is first presented in Chapter 2, followed by a description of the experimental setup and the new .12-mm sand in Chapter 3. In this chapter, the wavemaker calibration, and complete analysis of experimental accuracy are also discussed.

The actual experiments completed in this study are summarized in Chapter 4. Most experiments made use of the new sand, which has a grain size of .12 mm, while some additional experiments were completed using the .20-mm sand. In addition, the experimental procedures for both the monochromatic and spectral wave experiments are summarized in this chapter.

Finally, the results related to the response of the sediment bed and associated wave attenuation are presented and discussed in Chapters 5 and 6. In these chapters, proposed improvements and modifications to existing relationships are presented. These proposed expressions are also summarized in Chapter 7.

2 Brief Summary of Basic Theory

2.1 Qualitative Description of Bottom Sediment Motion

To better understand the basic physics of the interaction between waves and the sand, one might consider a flat bed of sand with waves of relatively small amplitude passing over it. In this case, the shear due to the waves passing over the sand would not be enough to dislodge the sand particles. However, if we start increasing the amplitudes of the waves, sand grain motion will eventually occur. This motion would first be observed at any irregularities in the sand bed. Next, if we increase the wave amplitude some more, a general rolling motion might be observed at these irregularities, which will eventually lead to the formation of small ripple crests. Once these ripple crests attain a height that can significantly affect the flow in the bottom boundary layer, vortices will develop that will form more ripples. The resulting ripple "patch" will expand and eventually cover the entire sand bed. After some time, the ripple formations on the sand bed will reach a statistically steady or "fully developed" state. Continued increase in wave energy will eventually lead to a regime of sand/wave interaction known as the "breakoff range." In this regime, the ripples lose their organized structure and attain a random chaotic appearance in which the high wave conditions appear to shave off the tops of the ripples. The theory to describe the wave/sand interaction in terms of the associated energy dissipation is outlined in the next section for the fully developed state and breakoff range.

2.2 Wave Attenuation

2.2.1 Monochromatic Waves

Wave attenuation over a movable sand bed is normally quantified by making use of conservation of energy. A one-dimensional energy conservation equation given by Madsen (1976) is:

$$\frac{\partial E}{\partial t} + \frac{\partial(c_g E)}{\partial x} = E_{diss} \tag{2.1}$$

Here, c_g is the group velocity, E is the wave energy per unit surface area, and E_{diss} is the energy dissipation in the bottom boundary layer. Considering the steady-state case, we can define the wave energy in terms of the wave amplitude. Assuming this energy is associated with a monochromatic wave, we have:

$$E = \tfrac{1}{2}\rho g a^2 \tag{2.2}$$

The dissipation term for the case of a monochromatic wave includes energy losses due to bottom friction and, in the case of a wave flume, sidewall friction. As noted in Rosengaus (1987), sidewall dissipation can be characterized by making use of an expression developed by Hunt (1952). The energy dissipation due to bottom friction can be determined from the bottom shear stress and horizontal bottom orbital velocity associated with the wave passing over the bed, and was defined by Kajiura (1968) as

$$D_b = \overline{-\tau_b(t) U_b(t)} \tag{2.3}$$

We can relate the maximum bottom shear stress to the bottom velocity by using the equation:

$$\tau_{bm} = \tfrac{1}{2}\rho f_w U_b^2 \qquad (2.4)$$

in which we have introduced the concept of a wave friction factor.

Neglecting the phase difference between the bottom shear stress and velocity (due to its small effect on energy dissipation), we can use these two relationships to get an equation for the energy dissipation due to friction in a turbulent boundary layer associated with monochromatic waves:

$$D_b = - \frac{2}{3\pi}\rho f_w U_b^3 \qquad (2.5)$$

As detailed in Rosengaus (1987), when applying our conservation of energy approach over relatively short distances (a few wavelengths, say) we can approximate the resulting $\partial(c_g E)/\partial x$ term of the energy conservation equation as:

$$\frac{\partial(c_g E)}{\partial x} = \rho g c_g a \frac{\partial a}{\partial x} \qquad (2.6)$$

Assuming steady-state, this leads us to:

$$\rho g c_g a \frac{\partial a}{\partial x} = - \frac{2}{3\pi}\rho f_w U_b^3 \qquad (2.7)$$

This equation provides us with a relationship between the wave attenuation and wave friction factor. As a result, bottom friction and an associated friction factor can be obtained by measuring the change in amplitude of a monochromatic wave propagating over a sand bed in a wave flume. Again, the details of this theory can be found in Rosengaus (1987).

2.2.2 Extension to a Wave Spectrum

A random sea is commonly characterized by its wave spectrum, which represents the distribution of the wave energy over a range of frequencies and directions. For a wave flume, we may simulate a wave spectrum in one direction over a finite number of discrete frequencies by taking advantage of the concepts of linear superposition. In terms of the near-bottom orbital velocity, we expect:

$$U_b(t) = \sum_{i=1}^{N} U_{b,i}\cos(\omega_i t + \phi_i) \tag{2.8}$$

In practice, the energy dissipation within the turbulent boundary layer of a wave spectrum is often simulated by simply expressing the spectrum of interest in terms of a representative monochromatic wave. Madsen et al. (1988) showed that this may be completed by assuming the proportionality:

$$D_i \propto U_{b,rep} \cdot U_{b,i}^2 \tag{2.9}$$

Here, the representative bottom velocity, U_b, is taken to be a root mean square value

$$U_{b,rep} = \left[\sum_{i=1}^{N} [U_{b,i}^2] \right]^{\frac{1}{2}} \tag{2.10}$$

The representative radian frequency is taken as

$$\omega_{rep} = \sqrt{\frac{\sum\limits_{i=1}^{N} U_{b,i}^2}{\sum\limits_{i=1}^{N} U_{b,i}^2/\omega_i^2}} \qquad (2.11)$$

and the representative horizontal bottom excursion amplitude, A_{brep}, can be obtained by dividing $U_{b,rep}$ by ω_{rep}.

When we incorporate these equations into the energy conservation equation, we find that:

$$\rho g c_{g,i} a_i \frac{\partial a_i}{\partial x} = -\frac{2}{3\pi}\rho f_{w,i} U_{b,rep} U_{b,i}^2 \qquad (2.12)$$

This equation can be used to relate friction factor and attenuation as discussed above. In this case, however, the equation is applied to each individual frequency component of a wave spectrum. Presently, the limited data available for spectral wave attenuation have indicated the validity of these assumptions.

2.3 Characterization of Sediments

One would expect that the wave friction factor defined above would be related to the characteristics of the sand bed. Therefore, our goal is to determine this relationship.

Previous studies by Stefanick (1979) and Rosengaus (1987) have had some success with implementation of a dimensionless sediment parameter to represent the wave-sediment interaction for oscillatory flow over cohesionless sediments. This parameter is

developed by comparing the fluid force acting on a single sand particle in a flat bed of sand to the submerged weight of that sand particle as follows:

$$\psi' = \frac{\tau_b' d^2}{\rho g(s-1) d^3} = \frac{\frac{1}{2} f_w' U_b^2}{(s-1) g d}$$ (2.13)

Furthermore, Madsen and Grant (1975, 1977) demonstrated the validity of application of a modified Shields Criterion (similar to the unidirectional Shields Criterion) to describe the initiation of motion criteria for monochromatic oscillatory flow over a flat bed of sand. While this initiation of motion is normally taken as a function of Reynolds number, it can instead be expressed as a function of a dimensionless sediment parameter:

$$S_* = \frac{d}{4\nu} \sqrt{(s-1) g d}$$ (2.14)

The Critical Shields Parameter as an indicator of initiation of motion is shown in Figure 2.1.

The ratio of the two parameters discussed above, ψ'/ψ_c, has successfully been used by Stefanick and Rosengaus to characterize results for a wide range of data.

2.4 Bedform Geometry

This relative Shields parameter has helped to define relationships characterizing bedform geometry and regimes of wave/sediment interaction (such as the wave intensity associated with the breakoff range.)

For bedform geometry, a number of empirical relationships were defined by Stefanick (1979). For wave intensities that are below the breakoff range, he found that:
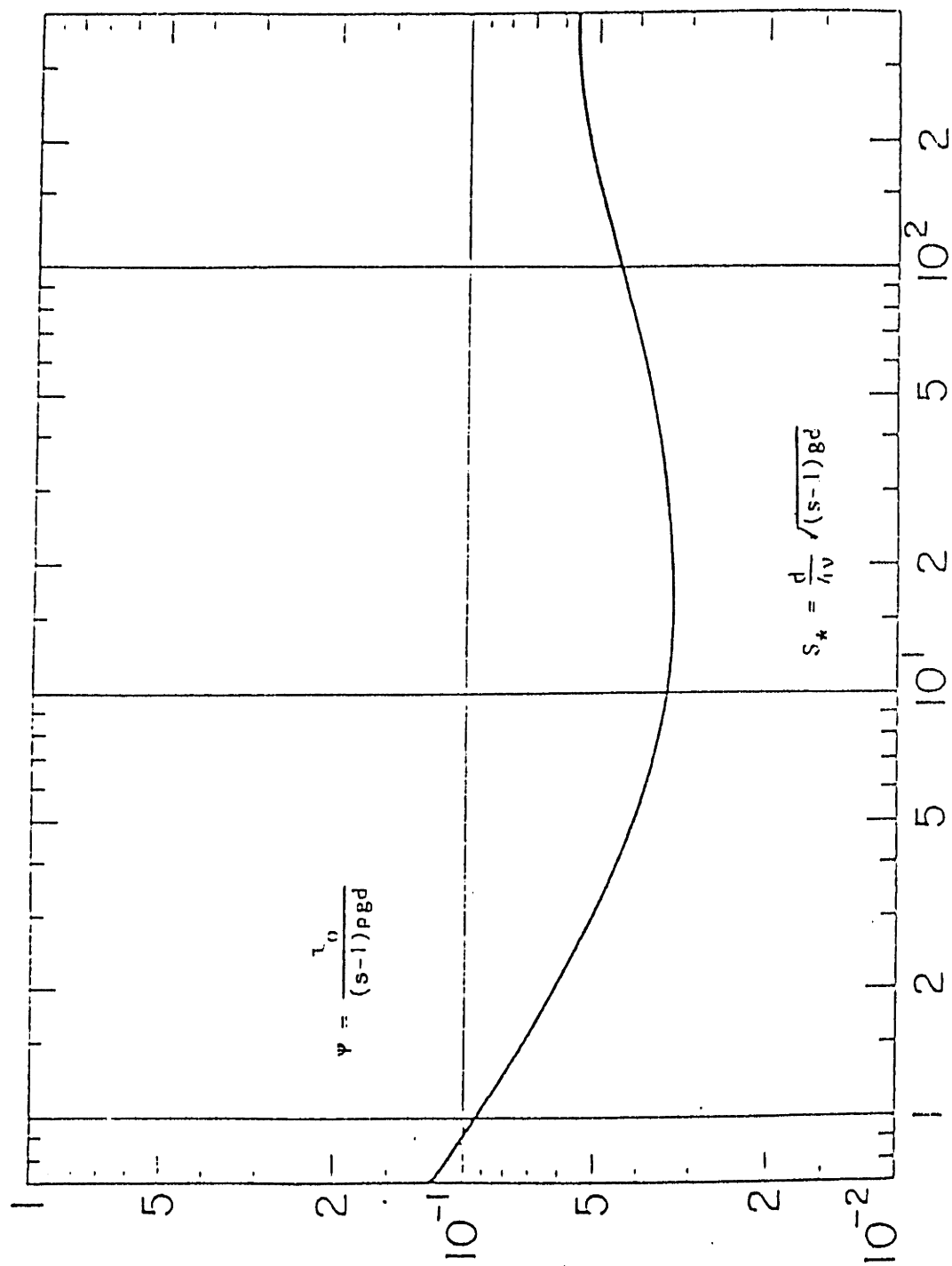
Figure 2.1   Critical shields parameter for initiation of motion in steady flow, from Madsen and Grant (1976).

$$\psi = \frac{\tau_0}{(s-1)\rho g d}$$

$$s_* = \frac{d}{4\nu} \sqrt{(s-1)g d}$$

$$\eta / A_b = .22[\psi' / \psi_c]^{-.16} \tag{2.15}$$

$$\eta / \lambda = .16[\psi' / \psi_c]^{-.04} \tag{2.16}$$

For wave intensities that were above the breakoff point, defined by

$$(\psi' / \psi_c)_b = 1.8 S_*^{0.6} \tag{2.17}$$

the parameters representing bedform geometry were found to have an additional dependence on S_*:

$$\eta / A_b = .48 S_*^{.82}[\psi' / \psi_c]^{-1.5} \tag{2.18}$$

$$\eta / \lambda = .28 S_*^{.59}[\psi' / \psi_c]^{-1.0} \tag{2.19}$$

In addition, Rosengaus (1987) proposed some simple relationships to fit experimental bedform data obtained for .20-mm sand. The relationships of interest include

$$\eta / A_b = 0.3094 - 0.0607(\psi' / \psi_c) \tag{2.20}$$

and

$$\eta / \lambda = 0.1864 - 0.0136(\psi' / \psi_c) \tag{2.21}$$

These expressions would apply to values of ψ' / ψ_c that are below $(\psi' / \psi_c)_b$ as defined by Equation 2.17.

2.5 Relative Roughness

For determination of the bottom roughness, the bedform characteristics noted above have been found to be physically relevant parameters. For example, in 1982, Grant and

Madsen used data from Bagnold (1946) and Carstens et al. (1967) to develop a relationship between relative roughness, k_b/A_b, and bedform characteristics and wave intensity (as characterized by ψ'/ψ_c):

$$\frac{k_b}{A_b} = 28\frac{\eta}{A_b}\frac{\eta}{\lambda} + 160(s + c_m)\frac{d}{A_b}\psi_c\left[\left[\frac{\psi'}{\psi_c}\right]^{\frac{1}{2}} - 0.7\right]^2 \qquad (2.22)$$

The behavior of this relationship is shown in Figure 2.2. As can be seen in that figure, the second term in Equation 2.22 represents the effects of sediment transport and can be neglected for relatively low ψ'/ψ_c. Therefore, for our purposes, we may rewrite Equation 2.22 as:

$$\frac{k_b}{A_b} = 28\frac{\eta}{A_b}\frac{\eta}{\lambda} \qquad (2.23)$$

A common experimental procedure has been to use the general form of this equation and vary the numerical coefficient to fit experimental data. For example, in Rosengaus (1987), a better fit to the data was found if the coefficient, 28, was replaced by 23.

2.6 Relating Friction Factor to Relative Roughness

A number of relationships have been proposed for relating the wave friction factor to the relative roughness. Figures 2.3 and 2.4 (from Stefanick, 1979) show some of the theoretical results that relate friction factors to wave conditions and roughness parameters. In Figure 2.3, Jonsson's Wave Friction Factor Diagram shows the friction factor as a function of a Reynolds Number and relative roughness, covering a variety of flow regimes. For rough turbulent flow, a number of curves that relate the friction factor to the relative roughness are plotted in Figure 2.4. Two of these include Jonsson's expression for rough turbulent flow:

Relative roughness (Grant & Madsen 1982)
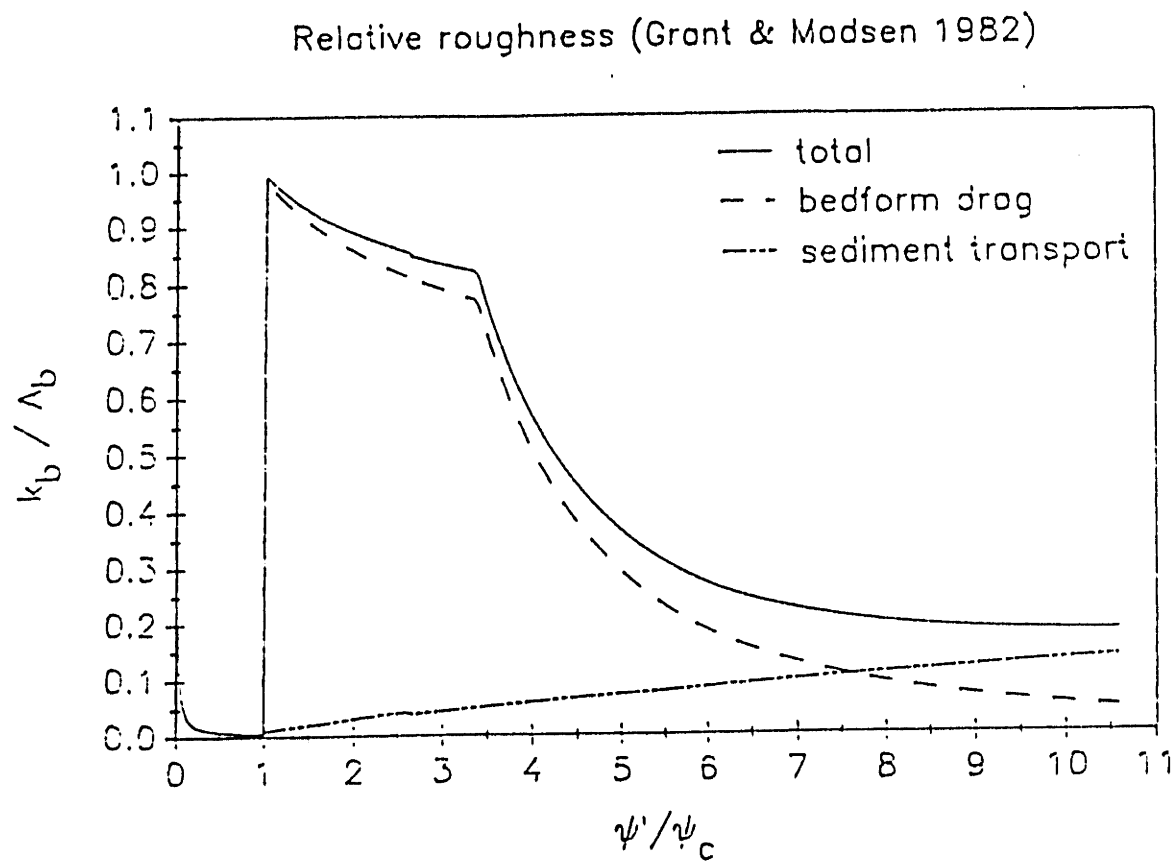
Figure 2.2   Relative roughness according to Grant and Madsen (1982), from Rosengaus (1987).
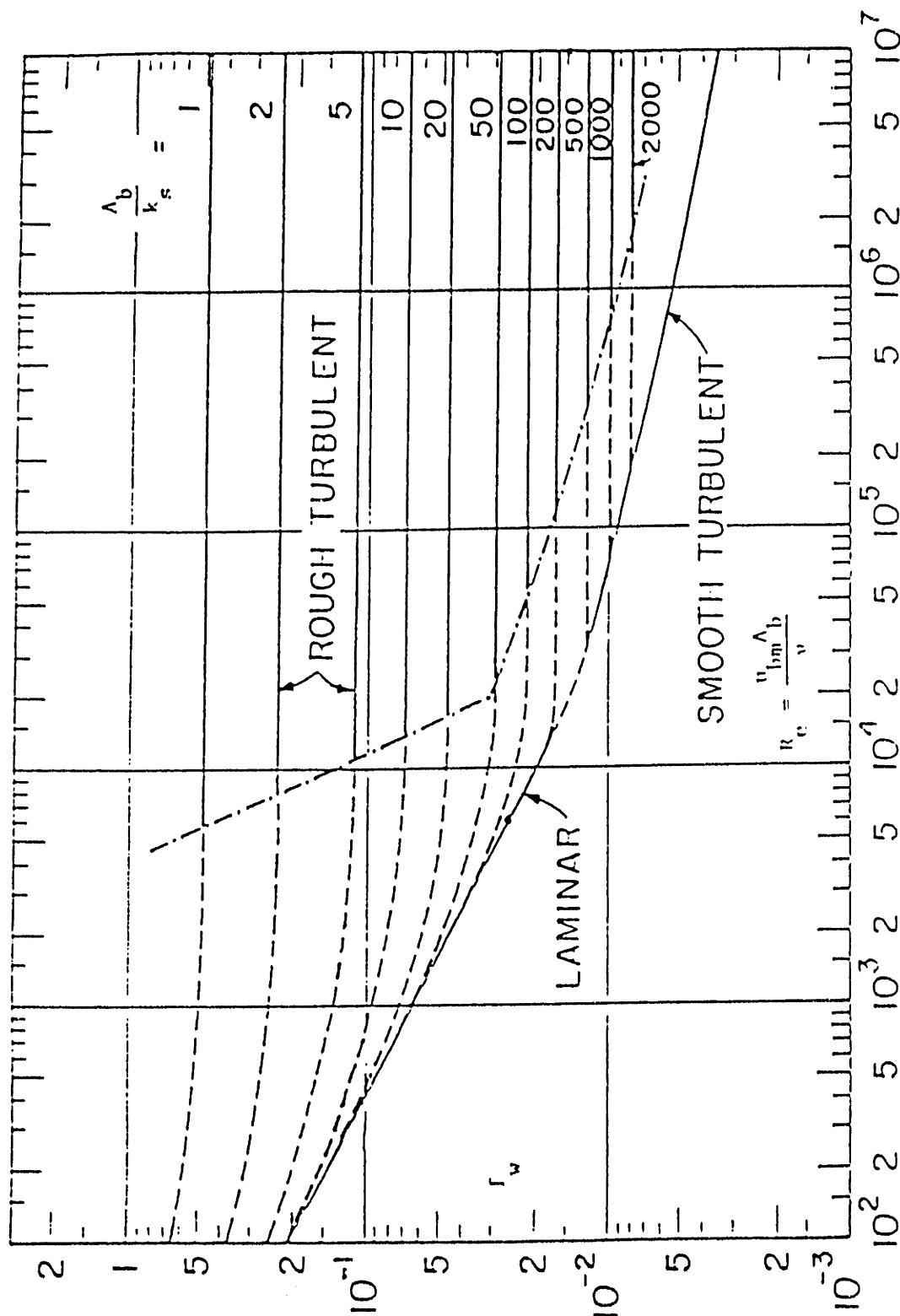
Figure 2.3   Jonsson's (1966) wave friction factor diagram, from Madsen and Grant (1976).
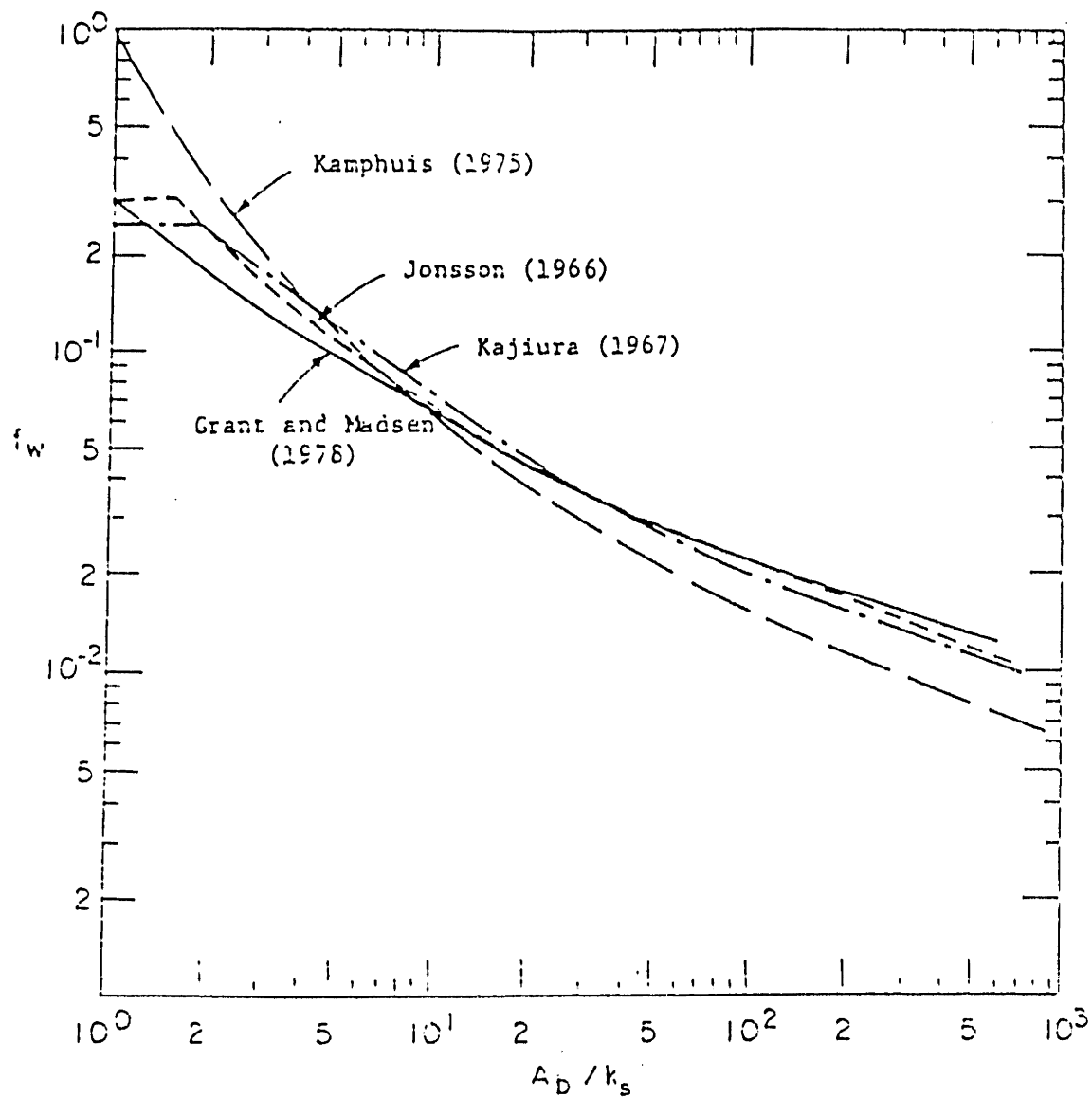
Figure 2.4   Wave friction factor vs. relative roughness in rough turbulent flow.
Comparison between Jonsson (1966), Kajiura (1968), Kamphuis (1975),
and Grant and Madsen (1978), from Grant and Madsen (1978).

$$\frac{1}{4\sqrt{f_w}} + \log_{10}\frac{1}{4\sqrt{f_w}} = \log_{10}\frac{A_b}{k_b} - 0.08 \tag{2.24}$$

and an expression proposed by Grant and Madsen:

$$f_w = \begin{cases} \dfrac{0.08}{\text{ker}^2[2\zeta_0^{1/2}] + \text{kei}^2[2\zeta_0^{1/2}]} & \text{for} \quad \dfrac{k_b}{A_b} < 1 \\[3ex] 0.23 & \text{for} \quad \dfrac{k_b}{A_b} \geq 1 \end{cases} \tag{2.25}$$

where

$$\zeta_0 = \frac{k_b/30}{\kappa U_*/\omega}$$

In this expression, ker and kei are the Kelvin functions of zeroth order, κ is Von Karman's constant, U_* is the maximum bottom shear velocity, and k_b is the Nikuradse equivalent sand roughness. This expression will be applied in a number of applications in later sections of this report.

3 EXPERIMENTAL SETUP

3.1 Description

The experimental work was completed in the Ralph M. Parsons Laboratory for Water Resources and Hydrodynamics at the Massachusetts Institute of Technology in Cambridge, Massachusetts. The project made use of a wave flume at the laboratory that was 28 meters long, 76.2 centimeters wide, and 91 centimeters deep. A programmable piston-type wave generator is located at one end of the flume, and an absorber beach with a slope of one on ten is located at the other end. A 7.5-cm horsehair mat was placed on this absorber beach to help minimize reflections.

For this project, a 10-cm layer of .12-mm uniform silica sand was placed in the bottom of the flume. Therefore, a 10-cm-high wooden ramp was placed near the wavemaker to contain the layer of sand and provide a smooth transition for the generated waves propagating up onto the sand layer. This arrangement provided a test section of approximately 16.5 meters between the ramp and the beach.

The wavemaker was controlled using a Charles River Data Systems computer that operated under the RT-11 operating system. This computer generated a digital signal that was converted to a ± 10 volt analog signal by a Data Translation 2781 D/A Converter. To ensure proper characteristics of the transmitted waves, the voltage signal was conditioned by making use of a wavemaker transfer function, as is further discussed in Section 3.4.

The generated waves were measured using six wave gauges and a controlling unit manufactured by the Danish Hydraulic Institute that made use of a proportionality between wave height and conductivity measured between two thin nichrome wires. The output signal from the controlling device was converted to a digital signal by a

Metrabyte Dash-16 D/A converter installed in an IBM PC XT computer. All additional data processing and analysis was completed by making use of this personal computer.

A schematic identifying the basic components of the experimental setup is shown in Figure 3.1 (from Rosengaus (1987)). Detailed descriptions of the various experimental components may also be found in Rosengaus (1987).

3.2 The Sediment

For his Sc.D. thesis, M. Rosengaus applied the theory summarized in Section 2 to the interaction between long waves and a sediment bed comprised of .20-mm sand. In this report, this theory is further tested by using an even finer silica sand with a mean grain size of approximately .12 mm.

This fine sand was purchased from New England Silica, Inc., from South Windsor, Ct. Specifically, the sand that was used was denoted as F-115 Ottawa sand. Review of the manufacturer's literature indicated that the sand distribution should have a mean grain size of .1 mm. However, to verify the sand characteristics, an in-house sieve analysis was completed.

This sieve analysis was completed in accordance with ASTM standards. In addition, the grain size distribution was analyzed in the manner recommended by the Shore Protection Manual, 1977, in which ϕ units are used to characterize the various grain sizes of the distribution. The ϕ unit is defined as:

$$\phi = -\log_2 d \tag{3.1}$$

where d is the grain diameter expressed in mm.
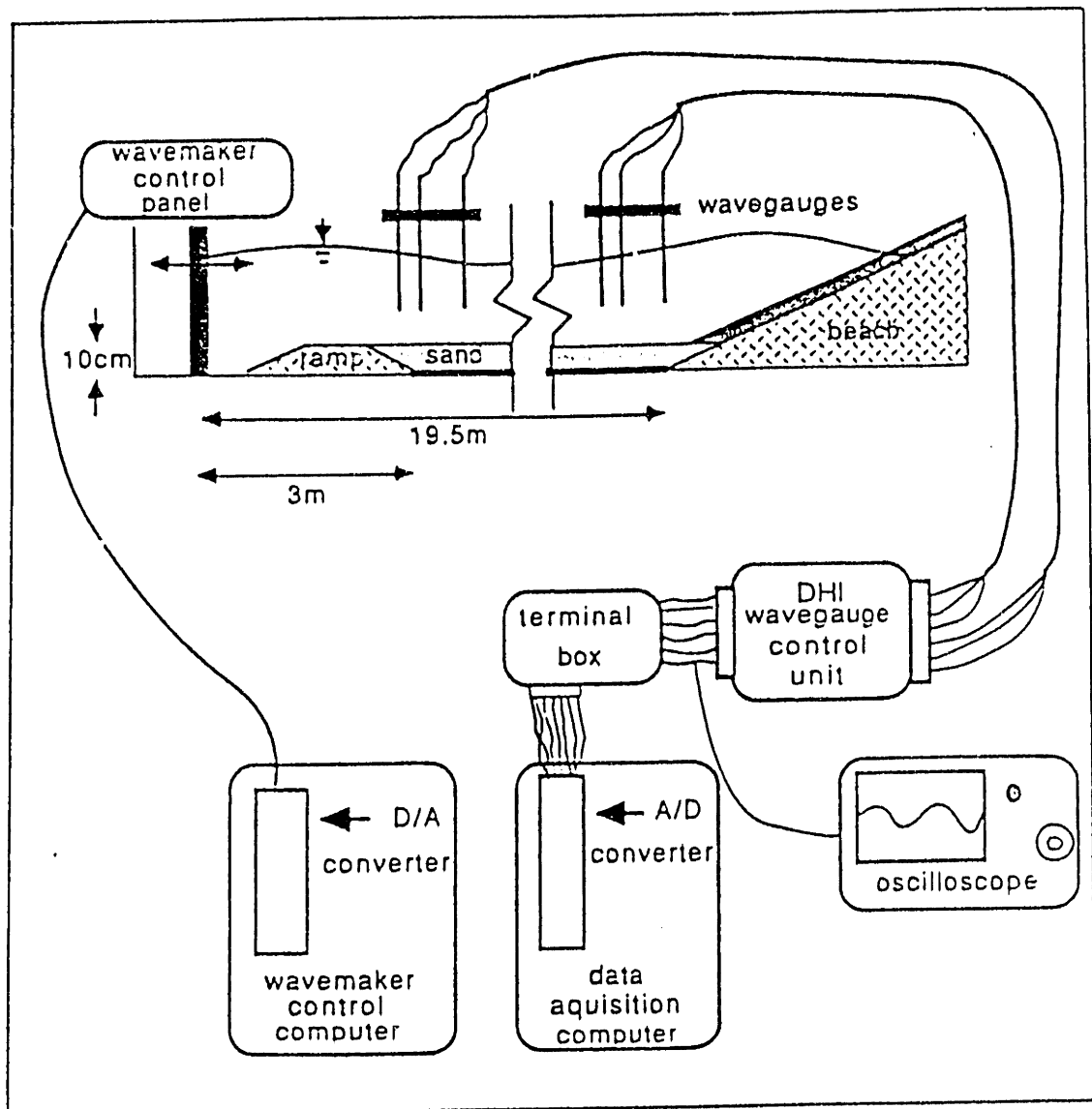
Figure 3.1   Schematic view of experimental installation, from Rosengaus (1987)

Using this characterization, the Shore Protection Manual's method makes use of a number of parameters to describe the grain size distribution. Some of these include M_ϕ, which expresses the mean grain size in ϕ units, $M_{d\phi}$, which expresses the median grain size, σ, which provides an indication of the sorting, and α, which provides an indication of skewness of the distribution.

The procedure for obtaining these parameters makes use of the plot shown in Figure 3.2, which shows the grain size distribution for the silica sand that was obtained. The parameters can then be defined as follows:

mean grain size in ϕ units:

$$M_\phi = \frac{\phi_{16} + \phi_{50} + \phi_{84}}{3} \qquad (3.2)$$

sorting:

$$\sigma = \frac{\phi_{84} - \phi_{16}}{2} \qquad (3.3)$$

mean grain diameter in mm:

$$d_{mean} = 2^{-M_\phi} \qquad (3.4)$$

skewness:

$$\alpha_\phi = \frac{M_\phi - M_{d\phi}}{2} \qquad (3.5)$$

The definitions of ϕ_{16}, ϕ_{50}, ϕ_{84}, and $M_{d\phi}$ are indicated in Figure 3.2. The mean grain size, d, which is the important parameter upon which the sediment parameter(S_*) is based, can be obtained from Equation 3.4 above. Also, Table 3.1 includes a comparison of this information for the in-house analysis and distributer's literature for both the

.
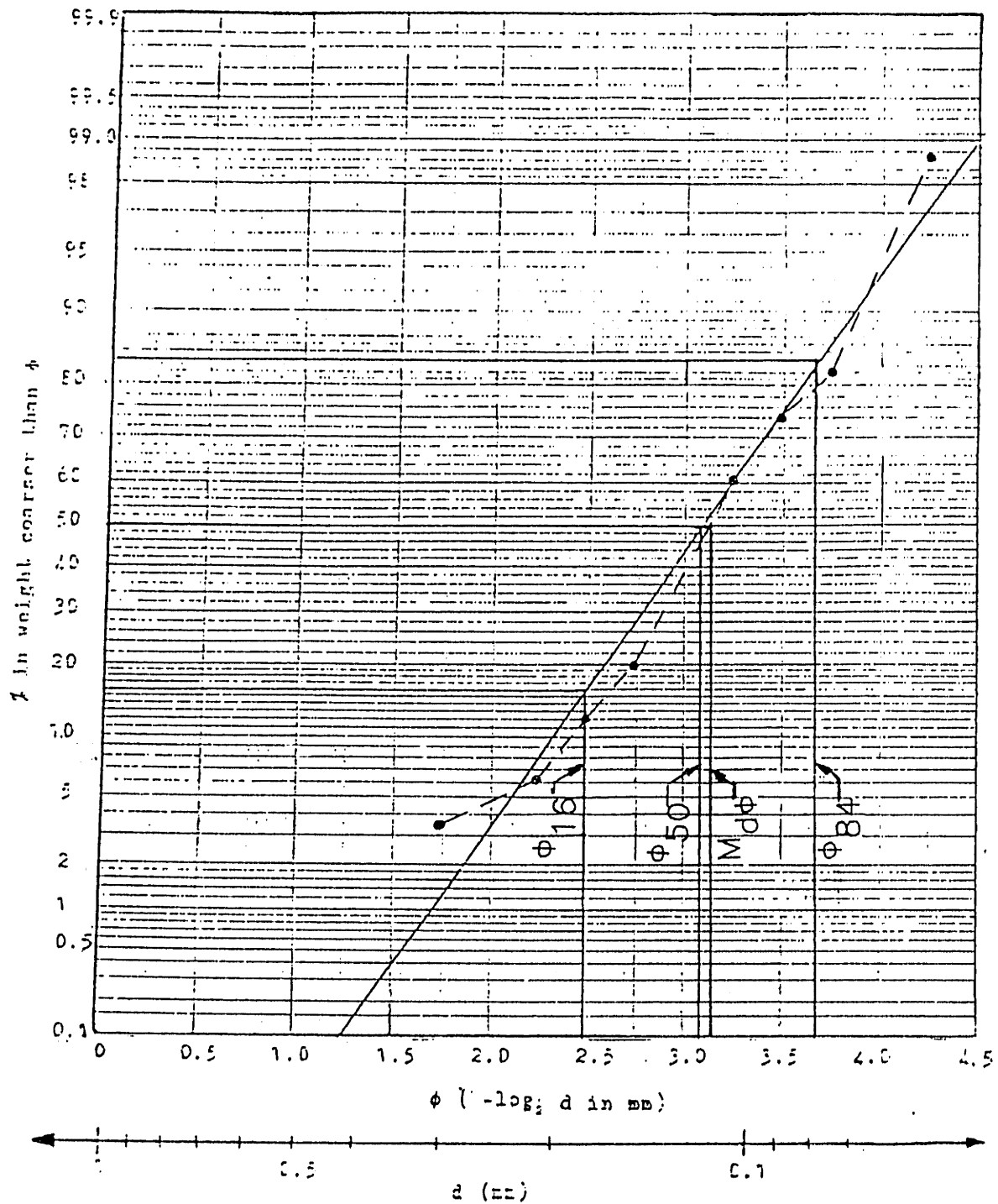
Figure 3.2   Grain size distribution of .12-mm Sand

.12-mm sand, and for the in-house analysis of the .20-mm sand (completed by M. Rosengaus):

Table 3.1

	.12-mm sand		.20-mm sand	
	distributer	in-house	distributor	in-house
$M(\log_2 (mm))$	3.260	3.097	2.473	2.417
$Md(\log_2 (mm))$	3.220	3.120	2.480	2.340
sig	0.510	0.595	0.470	0.315
alpha	0.078	0.039	0.489	0.240
d (mm)	0.104	0.120	0.196	0.196

From the grain size noted above, we can obtain the parameters that are considered to be physically relevant to wave/sediment interaction (discussed in Chapter 2). For the two sands used, these parameters are summarized as follows:

Table 3.2

	d (mm)	
	.12	.20
S_*	1.780	2.845
ψ_c	0.078	0.052
$(\psi'/\psi_c)_b$	2.30	3.41

Ideally, we would like to run experiments that would provide information on wave sediment interaction for a wide range of conditions for both the .12-mm sand and .20-mm sand. For the experiments completed on the .20-mm sand by M. Rosengaus,

the experimental setup basically limited the flow conditions to those within the breakoff range as defined above. However, for the .12-mm sand, the flow conditions can be generated that correspond to a ψ'/ψ_c of about 3.0. Therefore, completing the experiments on the .12-mm sand would be expected to yield information for a wider range of wave/sediment interaction.

3.3 Wave Generation

3.3.1 Monochromatic Waves

In 1951, Biesel and Suquet established the linear theory associated with the use of a piston-type wavemaker to generate monochromatic waves. The relationship between the wavemaker motion and monochromatic wave characteristics was shown to be

$$\xi(t) = -\xi_0 \cos \omega t = -\frac{an_1}{\tanh kh} \cos \omega t \tag{3.2}$$

with n_1 defined as

$$n_1 = \frac{c_g}{c} = \frac{1}{2}\left[1 + \frac{2kh}{\sinh 2kh}\right] \tag{3.3}$$

In 1971, Madsen showed that when the piston-type wavemaker motion is used to generate long waves associated with Stokes Second Order Wave Theory, two second harmonics are produced—a "bound" second harmonic, and a "free" second harmonic. The bound harmonic is described by

$$a_B{}^{(2)} = \frac{ka^2}{4}\frac{(2 + \cosh 2kh)\cosh kh}{\sinh^3 kh} \tag{3.4}$$

and the free harmonic is

$$a_F^{(2)} = \frac{1}{2}a^2\frac{\coth kh}{h}\left[\frac{3}{4\sinh^2 kh} - \frac{n_1}{2}\right]\frac{\tanh k_F h}{n_2} \tag{3.5}$$

where

$$n_2 = \frac{1}{2}\left[1 + \frac{2k_F h}{\sinh k_F h}\right] \tag{3.6}$$

and k_F is the wave number of the second free harmonic that satisfies the following dispersion relationship:

$$(2\omega)^2 = gk_F\tanh k_F h \tag{3.8}$$

In addition, this free second harmonic can be eliminated by adding a second harmonic correction to the wavemaker motion such that:

$$\xi(t) = -\xi_0\left[\cos \omega t + \frac{1}{2}\frac{a}{h}\frac{1}{n_1}\left[\frac{3}{4\sinh^2 kh} - \frac{n_1}{2}\right]\sin 2\omega t\right] \tag{3.7}$$

The details of the effectiveness and accuracy of the removal of the second harmonic is discussed and demonstrated in Rosengaus (1987).

3.3.2 Spectral Waves

For the spectral wave generation, the linear theory noted above may be used to advantage by implementing the theory of linear superposition. To simulate a wave spectrum, a finite number of discrete frequencies are defined and a representative monochromatic wave is chosen for each one. Thus, the surface profile would be represented by:

$$\eta = \sum_{i=1}^{N} a_i\cos(k_i x - \omega_i t - \theta_i) \tag{3.9}$$

where one set of randomly chosen phases can be used to simulate one realization of the spectrum. Generation of the spectrum can be accomplished by superimposing the wavemaker motion for each of the components:

$$\xi(t) = \sum_{i=1}^{N} \xi_i(t) \tag{3.10}$$

Using these principles, simulation of a particular wave spectrum can then be accomplished by defining discrete frequencies and associated component amplitudes for generation. Rosengaus (1987) discussed two possible methods for spectrum simulation: an equally spaced components method, and an equal energy components method. In the former, equally spaced frequencies components are chosen. The amplitudes are then defined to model the spectrum of interest. In this method, one or two components will comprise the majority of the energy in a typical spectrum. In the latter method, the frequency components are chosen such that all components are of equal energy. Therefore, the amplitudes of each of the components would be the same. In this case, more frequency components would be located near the frequency associated with the peak spectral density. These two spectral simulation methods are clarified in Figure 3.3 (taken from Rosengaus (1987)). In addition, a detailed discussion of spectral simulation can be found in Rosengaus (1987).

In this study, two types of spectra were simulated. The first spectrum used was a Pierson-Neumann spectrum. This spectrum is relatively broad banded and is defined by:

(equally spaced components method)

(equal energy components method)
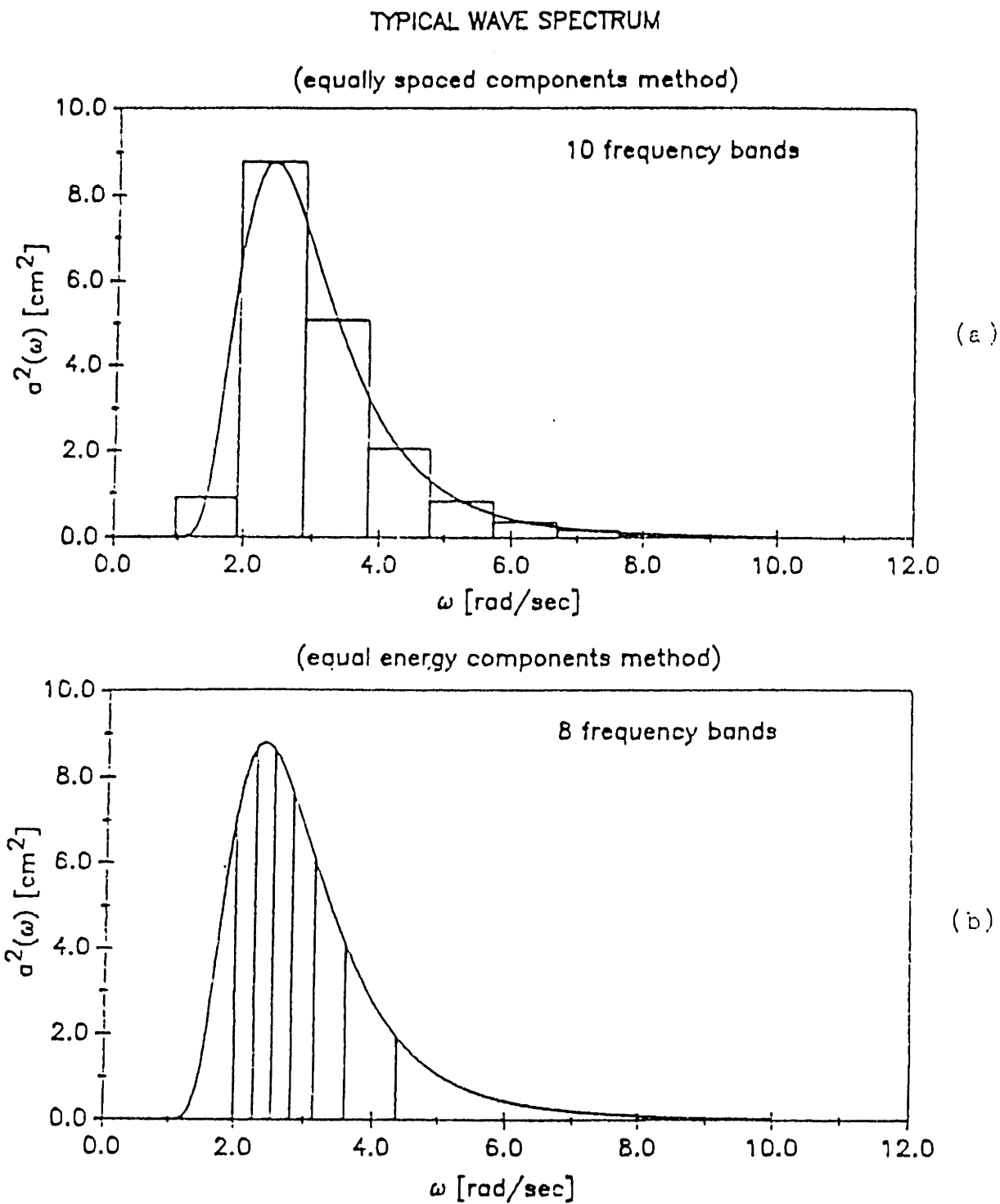
Figure 3.3   Two methods for simulating a wave spectrum, from Rosengaus (1987)

$$S_{\eta\eta}(\omega) = c\pi\omega^{-6}\exp\left\{-\frac{2g^2}{\omega^2 U_{10}^2}\right\} \tag{3.11}$$

where

$$c = \frac{E_T}{3\left[\frac{\pi}{2}\right]^{3/2}\left[\frac{U_{10}}{2g}\right]^5} \tag{3.12}$$

In this equation for the constant, c, E_T represents the total energy associated with the spectrum, and the wind speed, U_{10} is defined by:

$$U_{10} = \sqrt{\frac{2}{3}}\frac{g}{\omega_{max}} \tag{3.13}$$

A typical Pierson-Neumann Spectrum is shown in Figure 3.4.

The second spectrum simulated was a JONSWAP Spectrum. This spectrum, shown in Figure 3.5, is a narrow-banded spectrum that is generally considered to be a more realistic representation of ocean wave spectra. This spectrum is defined by:

$$E_J = E_{PM}\gamma^{\exp\left\{-\frac{[\omega/\omega_{max} - 1]^2}{2\sigma^2}\right\}} \tag{3.14}$$

where E_{PM} is:

$$E_{PM} = \frac{2\pi\alpha g^2}{\omega^5}\exp\left\{-\frac{5}{4}\left[\frac{\omega_{max}}{\omega}\right]^4\right\} \tag{3.15}$$

This spectrum can be applied in shallow water by using:

$$S_{\eta\eta}(\omega) = \Phi(\omega)E_J \tag{3.16}$$
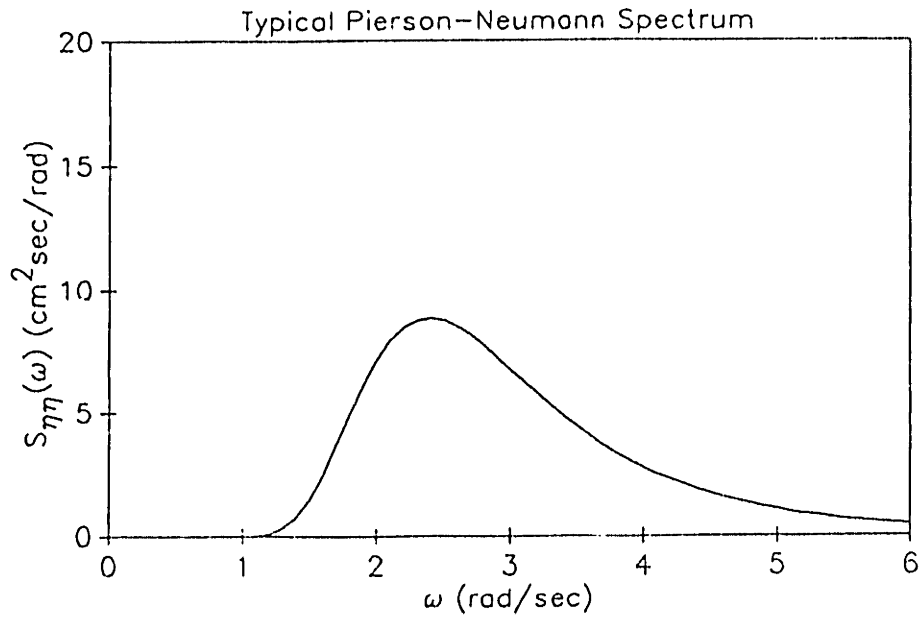
Figure 3.4   Typical Pierson–Neumann spectrum, with an ω_{max} of 2.39 and spectral energy equal to that of a 6-cm monochromatic wave
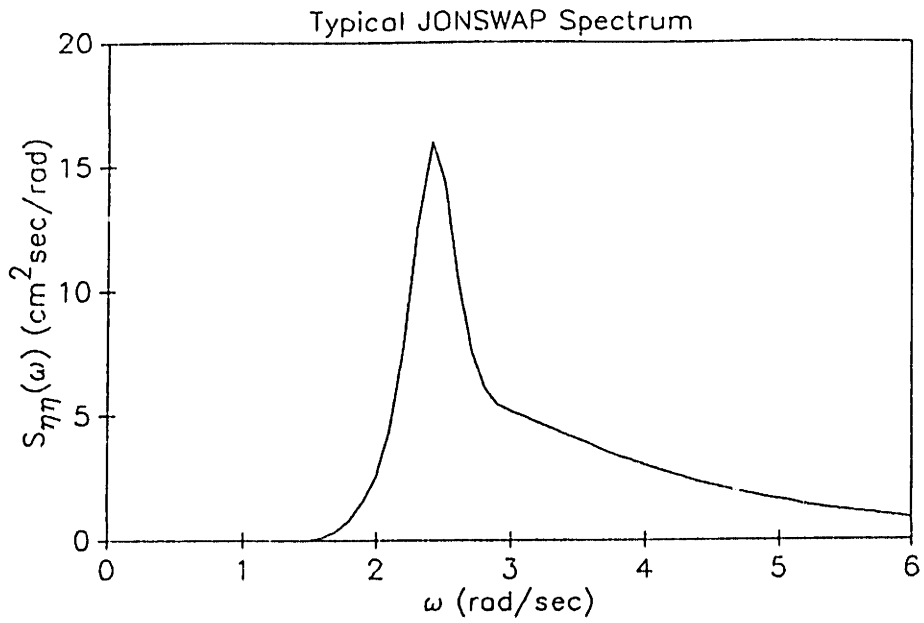
Figure 3.5   Typical JONSWAP spectrum, with an ω_{max} of 2.39 and spectral energy equal to that of a 6-cm monochromatic wave

where $\Phi(\omega)$ is obtained from:

$$\Phi(\omega) = \chi^{-2}[1 + \omega_h{}^2(\chi^2 - 1)]^{-1} \tag{3.17}$$

In this equation,

$$\omega_h = \omega\left[\frac{h}{g}\right]^{1/2} \tag{3.18}$$

and χ is obtained from:

$$\chi\tanh(\omega_h{}^2\chi) = 1 \tag{3.19}$$

The parameters that may be varied in these equations included a peak enhancement factor, γ, a spectral width parameter, σ, and a Phillips Constant, α. First, the peak enhancement factor was taken to be 3.3. Often two spectral width parameters are used—one for the spectral band width associated with frequencies less than the maximum frequency (call it σ_A) and another for those greater than the maximum frequency (call this one σ_B). Commonly σ_B is slightly larger than σ_A. Since they are generally similar in magnitude, a single spectral width parameter of 0.08 was used. The final parameter, α, was varied to set the total energy associated with the spectrum. A typical value was 0.0015 which yielded a design spectrum with the total energy equal to that of a 6-cm wave with peak frequency of 2.39 rad/s.

3.4 Wavemaker Calibration

In order to operate the wavemaker in the manner prescribed by the equations above, the wavemaker system must be calibrated. The calibration is necessary to characterize

the way in which the system will translate an input voltage signal into an actual wavemaker displacement. This characterization is commonly defined in terms of a transfer function with both an amplitude and phase. The amplitude of the transfer function defines the magnification or reduction of the actual output wavemaker displacement relative to the desired or input motion, and the phase of the transfer function represents the lag of the output behind the input. Therefore, we can define the input motion by

$$\xi_{in}(t) = \text{Real}\{|\xi_{in}|e^{i(\omega t + \beta_{in})}\} \tag{3.20}$$

and the desired output motion by

$$\xi_{out}(t) = \text{Real}\{|\xi_{out}|e^{i(\omega t + \beta_{out})}\} \tag{3.21}$$

In this case, the transfer function can be defined as

$$H = \frac{\xi_{out}}{\xi_{in}} = |H|e^{i\gamma} \tag{3.22}$$

where the amplitude of the function is

$$|H| = \frac{|\xi_{out}|}{|\xi_{in}|} \tag{3.23}$$

and the phase is

$$\gamma = \beta_{out} - \beta_{in} \tag{3.24}$$

Then, to get the proper wavemaker displacement we must define a modified input displacement:

$$\xi_{in}(t) = \frac{|\xi_{out}|}{|H|} e^{i(\omega t + (\beta_{out} - \gamma))} \qquad (3.25)$$

When this modified displacement is used as input, the desired displacement described by Equation 3.21 will be obtained.

Calibration of the system involves determination of the amplitude and phase of the transfer function for a range of wavemaker operating conditions (included signal magnitude, frequency, and depth of water in which the wavemaker operates). This calibration was initially completed by M. Rosengaus. The details of the analysis may be found in his doctoral thesis. In March of 1988, the pressure and voltage gain settings for the wavemaker were reset by Jack Crocker, the Laboratory Technician. The pressure setting was increased from 1000 psi to 1200 psi and the voltage gain was also increased. These changes were completed to increase the wavemaker output to allow the generation of larger monochromatic waves and higher energy wave spectra. Since the characteristics of the wavemaker system had changed, a new calibration was necessary.

To simplify this calibration, an existing wavemaker generation program, which included the transfer function developed by Mike Rosengaus, was used as the input to the wavemaker system. The previously developed transfer function is shown in Figures 3.6A and 3.6B (from Rosengaus (1987)).

For this wavemaker system, both the amplitude and phase were found to be strong functions of frequency and relatively weak functions of the magnitude of the signal. Therefore, since previous calibrations had shown the transfer function to be relatively

WAVEMAKER TRANSFER FUNCTION
(Interpolation polynomial)

(a)

WAVEMAKER TRANSFER FUNCTION
(Interpolation polynomial)

(b)
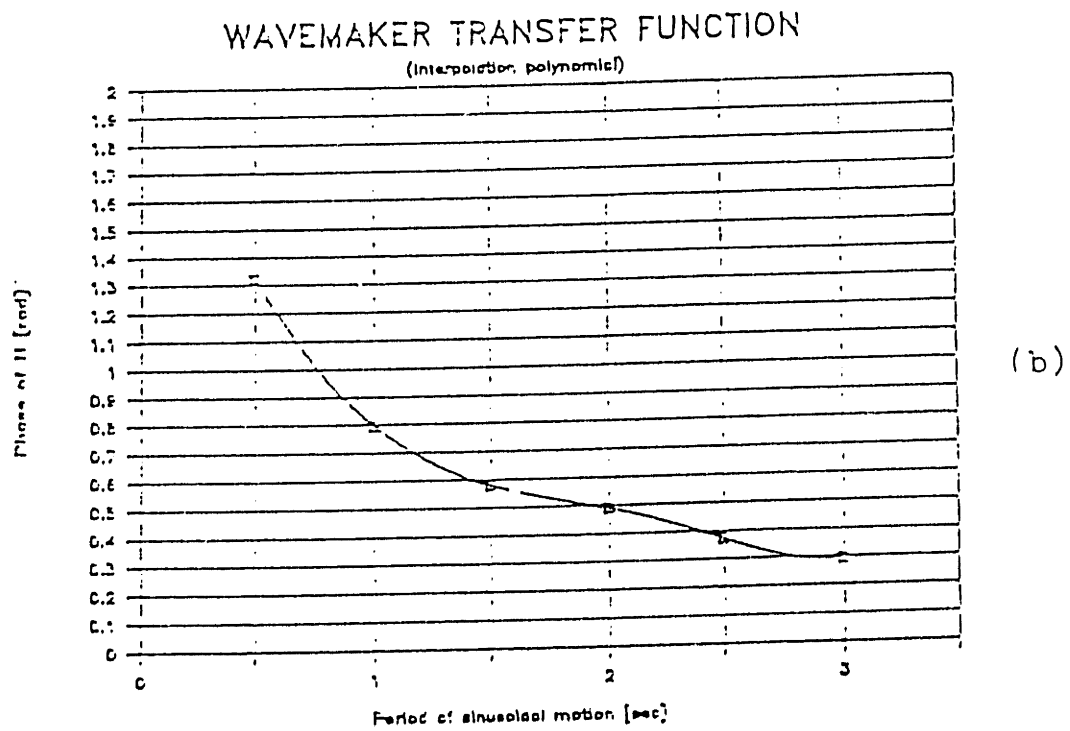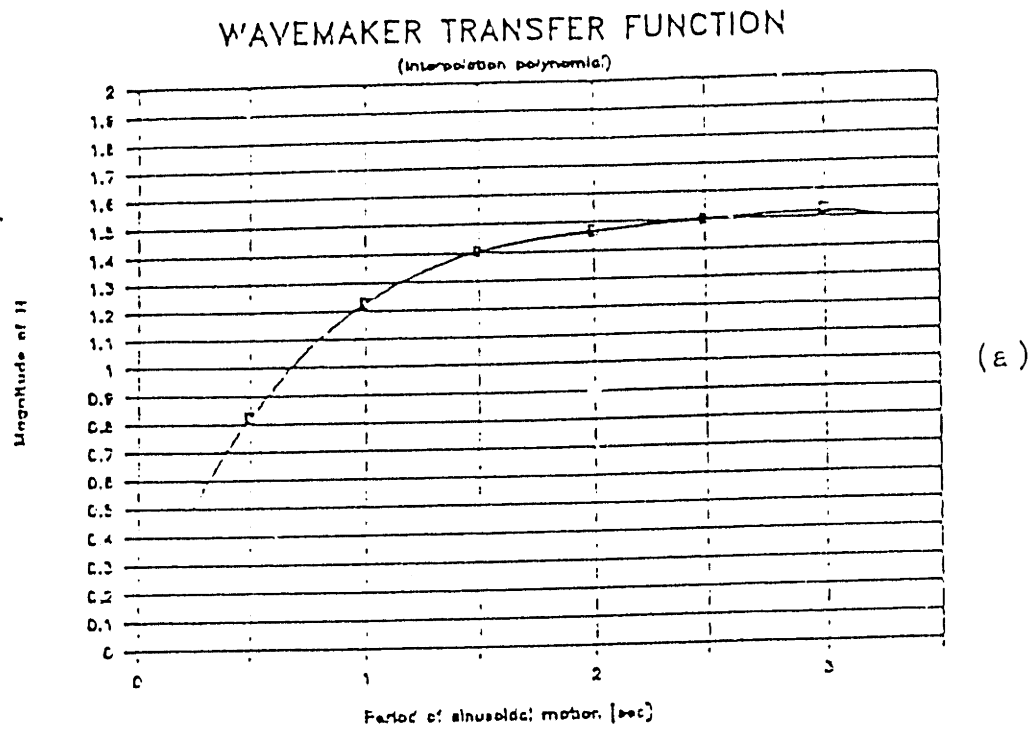
Figure 3.6   Origional wavemaker transfer function, from Rosengaus (1987)

insensitive to the depth of water in which the wavemaker operates and most experiments would use a 60-cm depth, the 60-cm depth was used for wavemaker calibration.

The output amplitude vs input amplitude, $|H|$, was then determined over a range of frequencies and signal magnitudes. This information is summarized in Figure 3.7A. As can be seen in this figure, the amplitude is a relatively weak function of the signal magnitude but is a relatively strong function of frequency (as expected). In general, the lower frequency (higher period) oscillations and lower input signals result in more magnification of the output signal.

In a similar manner, the phase angle between the output signal and input signal was determined over the same range of frequencies and signal magnitudes. This information is summarized in Figure 3.7B. In this case, the higher frequencies (lower periods) resulted in a greater phase lag between the input and output signals. Also, the phase angles associated with the different input signal magnitudes displayed some scatter when compared at discrete frequencies. This simply shows that the effect of the input frequency magnitude was relatively insignificant and the different measurements could not be differentiated when read off of the oscilloscope.

From these two plots, the transfer function was developed by choosing representative data points that would produce accurate wavemaker motion over a wide range of experimental conditions. Since it is desirable to run spectral waves that include a number of relatively small components oscillating at discrete frequencies, the amplitude ratios associated with $(H)_{in} = .25$ (as noted on Figure 3.7) were used to define the transfer function. Since the phase angles showed the scatter noted above, the mean values for each of the frequencies were used in developing the transfer function.

Wavemaker Calibration Data
(for 60 cm depth)
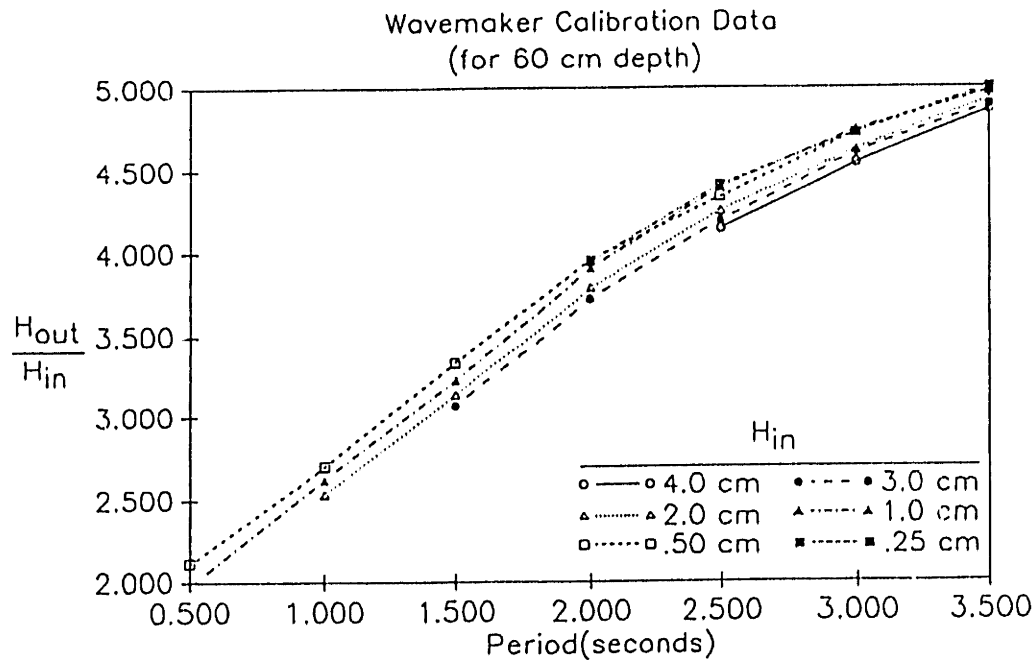
Figure 3.7A   Wavemaker calibration data (1988) – Amplitude

Wavemaker Calibration Data
(for 60 cm depth)
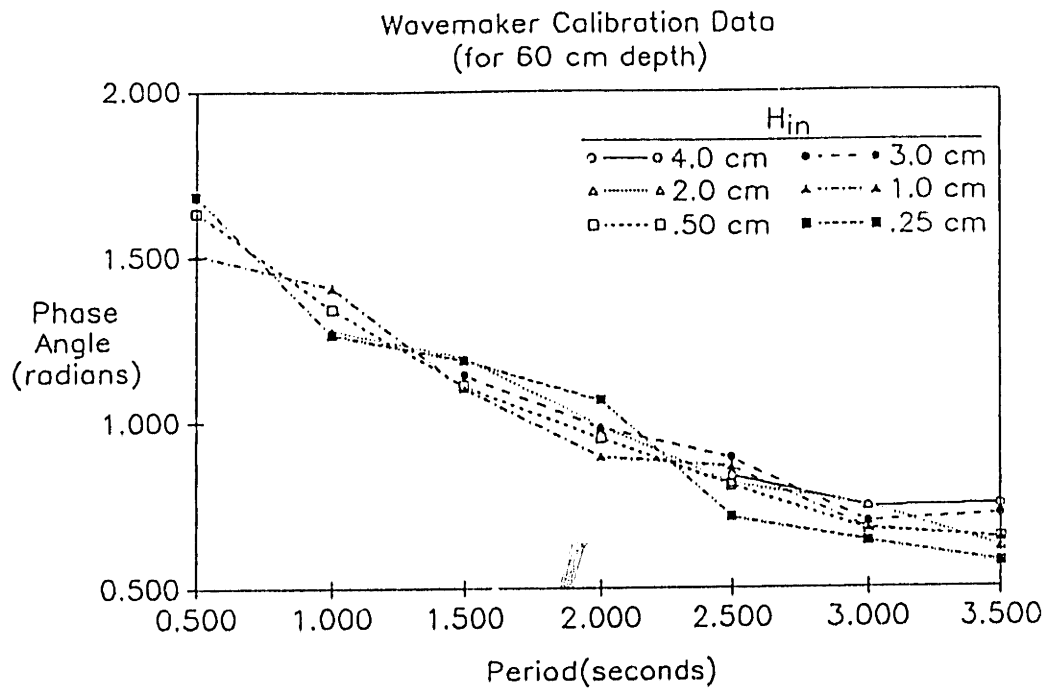
Figure 3.7B   Wavemaker calibration data (1988) – Phase

This information was then incorporated into the wave generation programs by making use of Newton's Divided Difference Interpolation Polynomials to define the relationships over a range of frequencies. This new transfer function was actually a correction to the previous transfer function and was simply added into the programs to modify the program's output signal (the wavemaker system's input signal) so that the proper wavemaker motion is realized. The final transfer function relationships for the amplitude and phase are plotted in Figures 3.8A and 3.8B. Comparison of the new transfer function to that described in Rosengaus (1987) shows a significant increase in the amplitude of the transfer function. Since the pressure was only changed by 200 psi, this increase can be primarily explained by the changes in the gain control.

3.5 Wave Measurement and Resolution

3.5.1 Review of Theory

Analysis of the interaction between waves passing over any sediment bed and the resulting bedforms naturally requires some measurements of the wave characteristics at different locations along the bed. Two methods for measuring the evolution of the wave amplitude over the length of the channel are detailed in Rosengaus (1987).

The first of these methods, referred to as the Reference Measuring Method (RMM) or Slow Measuring Method, used the wave gauges described in Section 3.1 to obtain wave records of the surface displacement variation at closely spaced locations along the wave flume. Provided that these records are taken after the wave motion within the flume is at a steady state, they need not be simultaneous. Next, a Fourier Analysis is completed for each record to define the energy associated with the first and second harmonic wave components. Assuming a monochromatic experiment is being completed, we would expect that, at the first harmonic, we have an incident wave
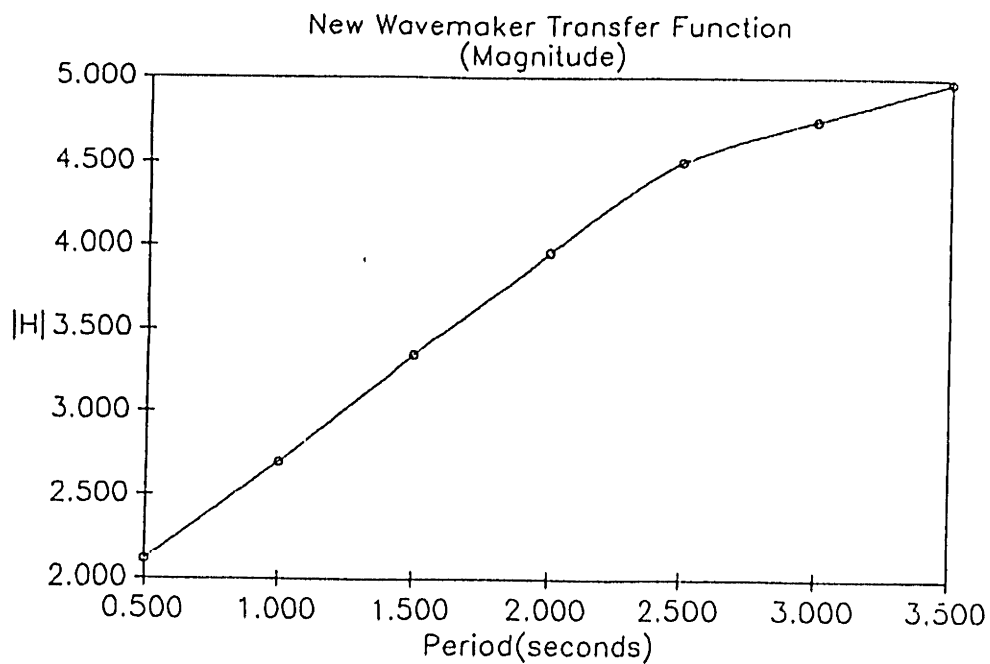
Figure 3.8A   Updated wavemaker transfer function (1988) – Amplitude
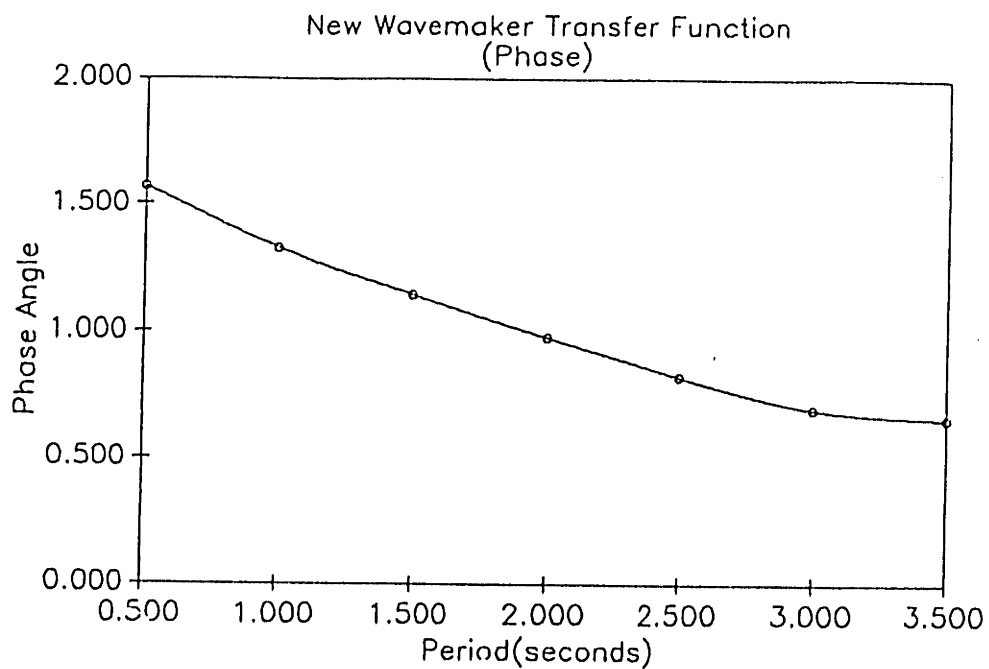
Figure 3.8B   Updated wavemaker transfer function (1988) – Phase

$$\eta_I = a_I \cos(kx - \omega t - \theta_I) \tag{3.26}$$

and a reflected wave

$$\eta_R = a_R \cos(kx + \omega t + \theta_R) \tag{3.27}$$

At the second harmonic, we expect a bound second harmonic wave

$$\eta_B^{(2)} = a_B^{(2)} \cos(2kx - 2\omega t - \theta_B^{(2)}) \tag{3.28}$$

and a free second harmonic wave

$$\eta_F^{(2)} = a_F^{(2)} \cos(k_F - 2\omega t - \theta_F^{(2)}) \tag{3.29}$$

which satisfies a dispersion relationship of

$$(2\omega)_F = gk_F \tanh k_F h \tag{3.30}$$

As discussed in Rosengaus's thesis, these various components may be separated by performing least-squares fits to the spatial variations of the amplitudes of the different frequencies.

While this method produces accurate results, it requires a tremendous amount of data and also a good deal of time to complete. Therefore, experimental requirements were simplified by using the Fast Measuring Method (FMM). In this procedure, the surface variation is measured simultaneously at a few closely spaced locations along the flume. Provided that the gauge spacing is much smaller than the length scales

associated with notable wave attenuation, the wave records may be used to separate the various components of interest. This is accomplished by using Fourier Analysis on the record of each gauge to define the amplitudes and phases associated with each frequency component and then using the concepts of Cramer's Rule to solve the resulting sets of linear equations. Again, the reader should consult Rosengaus (1987) for the details of the analysis.

3.5.2 Summary of Wave Measurement Procedures

For most experiments completed in this study, the Fast Measuring Method (FMM) was used in the context of a three-gauge setup. Basically, one station was located near the upstream (or "up-wave") end of the sand bed and another was located downstream ("down-wave") end of the sand bed.

In summary, implementation of the FMM made use of five computer programs:

1. A sampling program, which used the DASH-16 A/D converter to convert the -10 to +10 V signals to integral values between 0 and 4096.

2. A user-interactive gauge calibration program, for which the user would set the gauges at various elevations so that the program could sample the associated voltages and develop a surface displacement/voltage relationship for the gauge. The program would fit a fourth order polynomial to the curve and form files containing the regression coefficients for each of the gauges.

3. A processing program, which used files containing regression coefficients to convert the integers output from the sampling program into surface displacements.

4. A Fast Fourier Transform program, to convert the surface displacement records in the time domain into amplitude and phase records in the frequency domain.

5. A FMM program, to convert the amplitudes and phases associated with various frequencies into the appropriate components.

For the monochromatic wave experiments, the FMM program adequately identifies all wave components at each station. Therefore, attenuation can be studied by simply comparing the components of interest at the up-wave and down-wave stations. However, for the spectral wave experiments, non-linear interactions or energy transfers that occur between the various spectral components are unavoidable. Therefore, although the amplitudes of the spectral components could be measured at the two stations, there is still no way to determine the relative magnitudes of energy dissipation due to bottom friction and non-linear energy transfers as the wave component propagates through the wave flume.

To overcome this problem, additional procedures were necessary. Therefore, a procedure was developed to help evaluate the non-linear energy transfers. For all spectral experiments, a number of experiments were run over a flat sediment bed. For these flat bed runs, non-linear energy transfers between various components generally dominate the energy dissipation due to bottom friction. In addition, a laminar boundary layer exists for the flat bed conditions and the energy loss in the bottom boundary layer can be estimated by well-documented laminar boundary layer theory. Therefore, the energy dissipation due to bottom friction can be subtracted out and the energy changes due to non-linear energy transfers can be determined for each of the spectral components. If these are then recorded as fractional energy changes (relative to the energy at the up-wave station), they can be applied to the fully developed bed experimental runs. Thus, for the spectral fully developed bed runs, the fractional amplitude changes due to non-linear energy transfers are subtacted out, leaving only the effects of bottom friction. Additional information regarding the use of this

procedure can be found in Section 3.6.3.2, in which the accuracy of this procedure is discussed.

For the experiments completed by M. Rosengaus using the .20-mm sand, the flat bed was attained by flattening the bed using the "bottom scraper." For these experiments, it was found that the wave conditions in the flume could attain a steady state before the wave agitation would result in bedform development. However, for the .12-mm sand experiments, bedforms would develop before a steady state wave climate was attained. Therefore, twenty 5-foot by 2.5-foot flat steel plates were purchased. These plates were placed on top of the sand for the flat bed runs, assuring that no bedforms would develop and that the boundary layer remained laminar for these runs.

3.6 Accuracy of the Wave Measurements

In M. Rosengaus's doctoral thesis, a detailed analysis of the accuracy of the fast measuring system was included. This analysis included an error propagation analysis of the FMM and a comparison of the accuracy of the FMM relative to the RMM. In addition, the thesis includes a discussion of "blind zones" associated with the FMM, in which he defined gauge spacings that should be avoided because of a significant sensitivity to errors in phase differences.

Despite the intensive analysis of error and accuracy completed by M. Rosengaus, a few nagging questions remained. First, a sampling problem, which he referred to as the dropout problem, still persisted. In this case, the sampling program would skip a time step in one of the seven channels being sampled, placing the sample for the next time step in its place, and adjusting the remainder of the record accordingly. This phenomenon, which showed no easily recognizable pattern, was found to have an impact on experimental results when it occurred. In the second problem, the voltages shown

by the wave gauges during calibration were occasionally observed to "drift" after calibration. This drift could in effect render the regression coefficients invalid and possibly affect experimental results. Finally, the question of how accurately a monochromatic wave, or each component of a wave spectrum, could be measured required more attention. The review of these concerns is discussed in the following subsections.

3.6.1 Solution to the Samp'ing Problem

The sampling problem was noticed by Mike Rosengaus when his wave spectrum experiments yielded friction factors that did not appear to be reasonable. Also, energy conservation principles were not satisfied in a number of cases.

An explanation was found by reviewing surface profile records. Many records showed that, in an apparently random manner, for one of the seven channels being used for sampling, a sample for one time step was being skipped, or "dropped out." The sample associated with the next time step was inserted in its place. The remainder of the profile in that channel was still sampled throughout the sampling interval but was shifted back by the one time step that was dropped out. This "drop out" problem, which is clarified by Figure 3.9 (from Rosengaus (1987)), was quite difficult to characterize. However, an organized analysis revealed a pattern. The first dropout always occurred in the first channel, Channel 0; the second one always occurred in the second channel, Channel 1; the third in Channel 2; and so on. In addition, the time intervals between these dropouts often (although not always) occurred in systematic time intervals. This pattern indicated that the problem may not be a hardware problem, but a software problem. Somehow, it appeared that, during the transfer of the data from the Dash-16 Data Acquisition Board to the IBM PC, the computer's interrupts were not properly accommodated. Since this software was provided in a
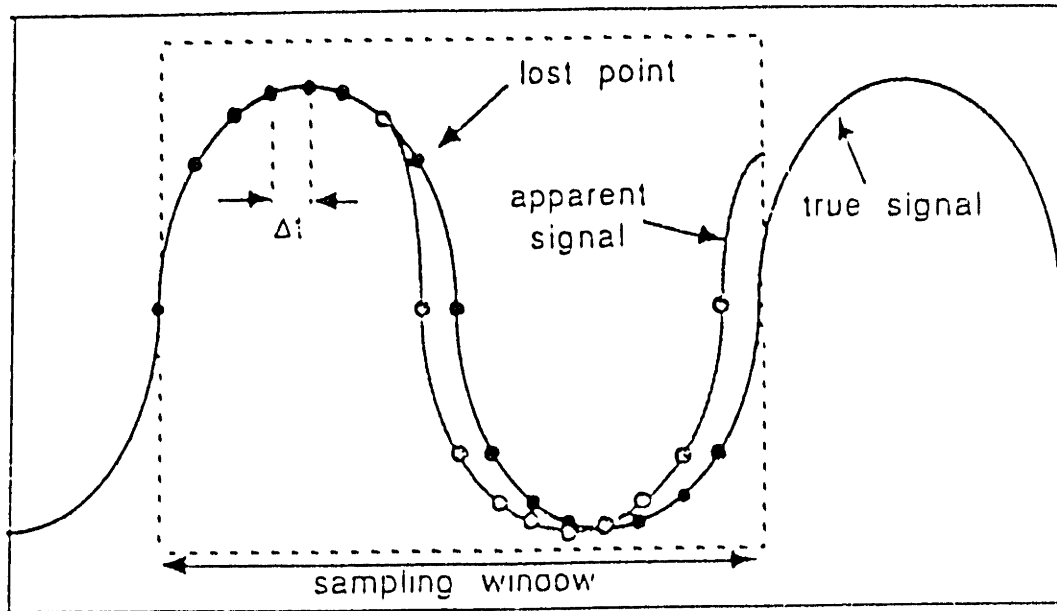
Figure 3.9   Schematic view of the sampling malfunction, from Rosengaus (1987)

packaged form rather than code, the problem was finally solved by purchasing another software package that was available from Metrabyte Corporation.

3.6.2 The Drift Problem

The second problem that was of concern was that of wave gauge "drifting." It was found that, after calibration, the voltages generated by the wave gauges for any given surface elevations would occasionally drift from the voltages obtained during calibration. Control of this drift problem was accomplished in a number of ways.

First, the warm-up time for the wave gauge unit increased from the 10 to 15 minutes as recommended by the manufacturer's literature to approximately 45 to 60 minutes before operation. This requirement was determined during the first analysis of this problem after it was first observed. In this analysis, careful observations were made during a number of successive calibrations after the wave gauge apparatus was initially turned on. On different days, different procedures were attempted, such as running waves over the gauges before calibration, leaving the water at its mean level thought the testing period, and mixing the water to ensure removal of temperature gradients. Of these parameters, the warm-up time proved to be the most critical.

Secondly, the accuracy of the calibration was verified by checking the voltages before and after experimental runs. After many experimental runs and accuracy tests, it was found that, in general, wave gauge drift tended to be characterized by an increase in the voltage. The highest calibration level (associated with the highest water surface level and maximum voltage) resulted in the highest upward drift. The lowest calibration level (associated with the lowest water surface level and minimum voltage) normally resulted in negligible drift. In addition, the voltages associated with the still water level (normally set to zero voltage) were found to be good indicators of the

magnitude of the drift. Keeping these observations in mind, these "zeros" can then be used as a criterion to determine the acceptability of measuring runs. Therefore, these zeros were checked before and after completing experimental runs. If the drift of these zeros for all gauges was well within the accuracy of the measuring system, the experimental run was considered to be acceptable. If the drift was too high, the experimental run was considered to be unacceptable, and the data were not included in friction factor computations.

Finally, control of the drift problem was ensured by implementing a number of other precautions. First, after filling the wave flume with water, it was commonly left for about three days so that it would reach room temperature. Also, the water was commonly mixed to ensure that all temperature gradients were eliminated. In addition, during experiments using the .12-mm sand, some reaction appeared to be occurring between the water and the nichrome wires associated with the wave gauges. This produced a thin film of slime on the wires that resulted in nonlinearities in the calibration. It was found that, as long as the gauges were wiped off after every run, the film had no effect on wave-gauge operation. Therefore, for all remaining experiments, the gauges were wiped off after every run.

3.6.3 General Accuracy Analysis

The final concern related to the accuracy of the measuring system was how accuracy limitations or errors were propagated though the equations for computation of a friction factor. In other words, how accurate are our friction factor estimates? To determine this, two cases were considered: Accuracy of monochromatic friction factors and accuracy of spectral friction factors.

3.6.3.1 Monochromatic Waves

First, the accuracy of the monochromatic wave experiments was determined by making use of the results from Experiment B. Wave intensities tested in Experiment B included amplitudes ranging from about 3 cm to 7 cm. In addition, review of wave measurements showed the standard deviation of the incident amplitude to be roughly .015 cm, which is less than 0.5 percent of the incident amplitude. In addition, measurements of the change in incident wave amplitude due to wave attenuation had a standard deviation of approximately .02 cm. Since the change in amplitude over the sediment bed ranged between .2 and .3 cm, this standard deviation implies an accuracy of 5 to 10 percent relative to the change in amplitude.

To determine the effects of these accuracy limitations on friction factor estimates the above information was propagated through the friction factor equations by using principles describing error propagation. For this case, given:

$$f_w = f_w(c_g,\ a,\ U_b,\ m_b) \tag{3.31}$$

we can express the error in f_w as

$$\Delta f_w = \left[\left[\frac{\partial f_w}{\partial c_g} \Delta c_g \right]^2 + \left[\frac{\partial f_w}{\partial a} \Delta a \right]^2 + \left[\frac{\partial f_w}{\partial U_b} \Delta U_b \right]^2 + \left[\frac{\partial f_w}{\partial m_b} \Delta m_b \right]^2 \right]^{\frac{1}{2}} \tag{3.32}$$

In these two equations, f_w is the wave friction factor, c_g represents the group velocity, U_b is the bottom horizontal orbital velocity, m_b represents the measured attenuation slope (change in amplitude per length of flume), and Δ denotes the standard deviation of the associated parameter.

When the above accuracy information was propagated through the friction factor equation, it was found that the friction factor estimates should be accurate within a standard deviation of approximately .012. In this case, we might expect that, if we run eight experiments, the average friction factor obtained might be accurate within a standard deviation of about .004. The experimental results agreed with the accuracy estimates quite well.

3.6.3.2 Spectral Waves

The accuracy of the measurements in the spectral wave experiments, in which a representative friction factor depends on the amplitudes of a number of components, was found to be more critical than for the monochromatic experiments. This is due to a number of reasons.

First, because the spectrum includes a number of components (five components for these experiments), each component must be smaller than the single component of the monochromatic wave experiments. This is due to the size limitations of the wave flume. Because each component's amplitude is smaller, the corresponding change in amplitude over the sediment bed will be smaller and the limitations of the measuring system will be of greater concern.

Also, the attenuation is defined in terms of a friction slope, m_b, which represents attenuation per unit length of flume. This slope is obtained by using the equation

$$m_b = m_t + m_{sw} + m_{nl} \tag{3.33}$$

in which m_t is the total change in amplitude per unit length, m_{sw} represents the attenuation due to sidewall friction, and m_{nl} is the change in amplitude per unit length

resulting from nonlinear transfers. Normally, the sidewall friction would be much less than the bottom friction for wave motion over bedforms. However, nonlinear effects are often found to be comparable to the effects of bottom friction. The nonlinear energy slope is determined by using runs over a flat bed (as explained in Section 3.5.2), for which the friction slope is minimal. Since our accuracy for these experiments is limited in the same way as for the fully developed bed runs, the estimate for the friction slope will have that much more error.

To determine the accuracy of spectral friction factor estimates, it was first necessary to determine the accuracy of amplitude measurements of the wave components and the associated attenuation. To accomplish this, data from Experiments S4 and S5 were used. Both of these spectral experiments included five wave components and simulated a Pierson-Neumann Spectrum. S4 represented an experiment with relatively high wave conditions, and S5 had relatively low wave conditions.

To start, we can consider the amplitude statistics for Experiment S4, which are shown in Tables 3.3A and 3.3B. In these tables, the measurements for all five wave components are summarized. These components, Components 1 through 5, have respective radian frequencies of 1.964, 2.393, 2.822, 3.375, and 4.541 rad/sec. As can be seen in the tables, the experiment was repeated ten times over a flat bed. This flat bed information is summarized in Table 3.3A. In addition, eight runs were completed over a fully developed bed, which implies that the bed is fully rippled and is statistically in a steady state. The fully developed bed information is summarized in Table 3.3B. For each of the runs completed, amplitudes of each component were measured at a location upwave (Station 1) and downwave of the sand bed (Station 2). The tables also include the difference between the Station 1 and 2 amplitudes, which is a critical variable necessary in determination of the friction factor. For this difference between Stations 1 and 2, a positive value indicates an increase in a component's amplitude as it

Table 3.3
Amplitude Measurements for a High Intensity Pierson–Neumann Spectrum

AMPLITUDE MEASUREMENTS FOR FLAT BED
(IN CM)

RUN ID	COMPONENT 1			COMPONENT 2			COMPONENT 3			COMPONENT 4			COMPONENT 5		
	STA 1	STA 2	DIFF	STA 1	STA 2	DIFF	STA 1	STA 2	DIFF	STA 1	STA 2	DIFF	STA 1	STA 2	DIFF
S401	2.766	2.763	-0.003	2.367	2.159	-0.208	2.180	2.311	0.131	1.949	1.440	-0.509	2.172	1.958	-0.214
S402	2.820	2.680	-0.140	2.210	2.380	0.170	2.222	2.215	-0.007	1.967	1.461	-0.506	2.148	2.014	-0.134
S403	2.882	2.781	-0.101	2.200	2.232	0.032	2.317	2.179	-0.138	1.962	1.485	-0.477	1.929	1.746	-0.183
S404	2.817	2.713	-0.104	2.223	2.252	0.029	2.242	2.238	-0.004	2.015	1.469	-0.546	2.140	2.067	-0.073
S405	2.852	2.878	0.026	2.249	2.277	0.028	2.273	2.193	-0.080	1.957	1.439	-0.518	2.036	1.714	-0.322
S406	2.833	2.782	-0.051	2.375	2.173	-0.202	2.127	2.180	0.053	2.012	1.472	-0.540	2.148	1.773	-0.375
S409	2.775	2.742	-0.033	2.185	2.233	0.048	2.146	2.133	-0.013	1.937	1.580	-0.357	2.000	1.790	-0.210
S410	2.751	2.805	0.054	2.258	2.174	-0.084	2.175	2.131	-0.044	1.910	1.453	-0.457	2.044	1.743	-0.301
S411	2.826	2.727	-0.099	2.288	2.182	-0.106	2.088	2.282	0.194	1.957	1.446	-0.511	1.901	1.923	0.022
S412	2.831	2.746	-0.085	2.168	2.234	0.066	2.105	2.162	0.057	2.004	1.622	-0.382	2.146	1.902	-0.244
AVG	2.815	2.762	-0.054	2.252	2.230	-0.023	2.188	2.202	0.015	1.967	1.487	-0.480	2.066	1.863	-0.203
STDEV	0.038	0.052	0.060	0.068	0.062	0.116	0.071	0.057	0.093	0.032	0.060	0.061	0.094	0.119	0.113

AMPLITUDE MEASUREMENTS FOR FULLY DEVELOPED BED
(IN CM)

RUN ID	COMPONENT 1			COMPONENT 2			COMPONENT 3			COMPONENT 4			COMPONENT 5		
	STA 1	STA 2	DIFF	STA 1	STA 2	DIFF	STA 1	STA 2	DIFF	STA 1	STA 2	DIFF	STA 1	STA 2	DIFF
S413	2.866	2.536	-0.330	2.243	2.150	-0.093	2.050	2.045	-0.005	1.933	1.437	-0.496	1.833	1.836	0.003
S414	2.769	2.695	-0.074	2.278	1.997	-0.281	1.999	2.086	0.087	1.933	1.414	-0.519	1.952	1.876	-0.076
S415	2.675	2.560	-0.115	2.266	2.101	-0.165	2.115	2.125	0.010	1.914	1.294	-0.620	1.856	1.678	-0.178
S416	2.723	2.557	-0.166	2.129	2.117	-0.012	2.129	1.992	-0.137	1.940	1.450	-0.490	1.977	1.705	-0.272
S417	2.817	2.605	-0.212	2.143	2.072	-0.071	2.154	2.015	-0.139	1.933	1.402	-0.531	1.849	1.675	-0.174
S418	2.816	2.602	-0.214	2.216	2.030	-0.186	2.036	2.112	0.076	1.929	1.397	-0.532	1.930	1.958	0.028
S419	2.789	2.533	-0.256	2.185	2.201	0.016	2.096	2.050	-0.046	1.910	1.421	-0.489	1.943	1.896	-0.047
S420	2.816	2.634	-0.182	2.198	2.022	-0.176	2.033	2.112	0.079	1.936	1.406	-0.530	1.973	1.955	-0.018
AVG	2.784	2.590	-0.194	2.207	2.086	-0.121	2.077	2.057	-0.009	1.929	1.403	-0.526	1.914	1.822	-0.092
STDEV	0.057	0.052	0.075	0.051	0.065	0.093	0.051	0.046	0.086	0.010	0.044	0.040	0.055	0.112	0.099

Table 3.4
Amplitude Measurements for a Low Intensity Pierson-Neumann Spectrum

AMPLITUDE MEASUREMENTS FOR FLAT BED
(IN CM)

RUN ID	COMPONENT 1			COMPONENT 2			COMPONENT 3			COMPONENT 4			COMPONENT 5		
	STA 1	STA 2	DIFF	STA 1	STA 2	DIFF	STA 1	STA 2	DIFF	STA 1	STA 2	DIFF	STA 1	STA 2	DIFF
S501	2.003	1.994	-0.009	1.741	1.673	-0.068	1.594	1.531	-0.063	1.517	1.313	-0.204	1.489	1.544	0.055
S502	1.952	1.950	-0.002	1.783	1.633	-0.150	1.526	1.646	0.120	1.524	1.308	-0.216	1.552	1.579	0.027
S503	1.982	1.965	-0.017	1.749	1.697	-0.052	1.476	1.591	0.115	1.571	1.304	-0.267	1.450	1.461	0.011
S504	1.960	1.957	-0.003	1.813	1.632	-0.181	1.535	1.537	0.002	1.545	1.353	-0.192	1.455	1.505	0.050
S505	1.994	1.954	-0.040	1.728	1.758	0.030	1.496	1.560	0.064	1.595	1.299	-0.296	1.576	1.411	-0.165
S506	1.987	2.027	0.040	1.735	1.664	-0.071	1.516	1.549	0.033	1.578	1.356	-0.222	1.589	1.477	-0.112
S507	1.965	1.957	-0.008	1.767	1.675	-0.092	1.534	1.618	0.084	1.546	1.307	-0.239	1.601	1.484	-0.117
S508	2.012	2.009	-0.003	1.694	1.763	0.069	1.577	1.577	0.000	1.580	1.277	-0.303	1.588	1.525	-0.063
S509	1.961	1.898	-0.063	1.659	1.792	0.133	1.617	1.582	-0.035	1.539	1.313	-0.226	1.511	1.531	0.020
S510	1.952	1.939	-0.013	1.845	1.638	-0.207	1.471	1.677	0.206	1.522	1.332	-0.190	1.612	1.448	-0.164
S511	1.987	1.925	-0.062	1.767	1.682	-0.085	1.490	1.685	0.195	1.508	1.332	-0.176	1.615	1.448	-0.167
S512	1.978	1.961	-0.017	1.758	1.681	-0.077	1.477	1.575	0.098	1.569	1.297	-0.272	1.592	1.429	-0.163
AVG	1.978	1.961	-0.016	1.753	1.691	-0.063	1.526	1.594	0.068	1.550	1.316	-0.234	1.553	1.487	-0.066
STDEV	0.019	0.034	0.027	0.047	0.051	0.095	0.046	0.050	0.081	0.027	0.022	0.040	0.058	0.049	0.088

AMPLITUDE MEASUREMENTS FOR FULLY DEVELOPED BED
(IN CM)

RUN ID	COMPONENT 1			COMPONENT 2			COMPONENT 3			COMPONENT 4			COMPONENT 5		
	STA 1	STA 2	DIFF	STA 1	STA 2	DIFF	STA 1	STA 2	DIFF	STA 1	STA 2	DIFF	STA 1	STA 2	DIFF
S513	1.945	1.813	-0.132	1.760	1.513	-0.247	1.482	1.550	0.068	1.535	1.258	-0.277	1.520	1.475	-0.045
S514	2.044	1.854	-0.190	1.702	1.559	-0.143	1.444	1.513	0.069	1.560	1.268	-0.292	1.585	1.392	-0.193
S515	2.026	1.783	-0.243	1.659	1.620	-0.039	1.531	1.442	-0.089	1.543	1.303	-0.240	1.497	1.373	-0.124
S516	2.077	1.853	-0.224	1.753	1.536	-0.217	1.473	1.596	0.123	1.562	1.230	-0.332	1.430	1.345	-0.085
S517	1.917	1.806	-0.111	1.815	1.547	-0.268	1.491	1.540	0.049	1.581	1.269	-0.312	1.521	1.468	-0.053
S518	2.045	1.847	-0.198	1.723	1.532	-0.191	1.451	1.527	0.076	1.588	1.268	-0.320	1.486	1.487	-0.001
S519	1.935	1.828	-0.107	1.742	1.569	-0.173	1.518	1.532	0.014	1.555	1.257	-0.298	1.585	1.411	-0.174
S520	1.979	1.784	-0.195	1.652	1.636	-0.016	1.560	1.442	-0.118	1.559	1.315	-0.244	1.532	1.386	-0.146
AVG	1.996	1.821	-0.175	1.726	1.564	-0.162	1.494	1.518	0.024	1.560	1.271	-0.289	1.520	1.417	-0.103
STDEV	0.056	0.027	0.048	0.051	0.040	0.086	0.037	0.049	0.079	0.016	0.025	0.032	0.048	0.050	0.063

propagates down the flume, and a negative value indicates a decrease in amplitude. In addition, averages and standard deviations are included in the tables. All of this information is also summarized for Experiment S5 in Tables 3.4A and 3.4B.

In general, measurements of each wave component for the higher energy spectrum(S4) indicate amplitudes in the range of 2.0 to 2.8 cm with a standard deviation of approximately .06 cm. For the lower energy spectrum(S5), the amplitudes range between about 1.5 and 2.0 cm and the standard deviation is approximately .04 cm. Therefore, the error in amplitude measurements may be expected to be less than about 3 percent for any run.

The difference between the amplitudes for Stations 1 and 2, which is a critical parameter for computing the friction factor, typically ranges between .05 to .10 cm for the high energy spectrum, and between .03 and .08 cm for the low energy spectrum. The standard deviations in these measurements is approximately .085 cm and .065 cm for the high and low energy spectra, respectively. Here, the standard deviations of the differences are of the same order as the magnitudes of the differences. There is obviously a reason for concern when one realizes that this difference in measured amplitudes provides the basis for the friction factor estimates.

Therefore, it is important to determine how much these inaccuracies will affect the friction factor results. This can be determined by propagating the above accuracy information through the friction factor equations using equations describing error propagation, as was done for the monochromatic experiments in Section 3.6.3.1. In this case, we expect:

$$f_w = f_w(c_{g,i},\ a_i,\ U_{brms},\ U_{b,i},\ m_{b,i}) \tag{3.33}$$

Thus, we can express the error in f_w as

$$\Delta f_w = \left[\left[\frac{\partial f_w}{\partial c_g}\Delta c_g\right]^2 + \left[\frac{\partial f_w}{\partial a}\Delta a_i\right]^2 + \left[\frac{\partial f_w}{\partial U_{b,rms}}\Delta U_{b,rms}\right]^2 + \left[\frac{\partial f_w}{\partial U_{b,i}}\Delta U_{b,i}\right]^2\right.$$
$$\left. + \left[\frac{\partial f_w}{\partial m_{b,i}}\Delta m_{b,i}\right]^2\right]^{\frac{1}{2}} \tag{3.34}$$

The overall accuracy of the friction factor estimates for wave spectrum experiments was estimated in this way. In the analysis, the higher energy accuracy information was used as a critical case since the standard deviations were higher. For this case, it was found that, for each component of a particular run, the friction factor estimate has a high standard deviation of approximately .12, which is of the same order as the friction factor itself. Experimental results for the friction factors of various components showed with this accuracy estimate to be reasonable.

If one considers the representative friction factor for the experiment, the standard deviation is .04. This estimate is still relatively high as compared to the friction factor estimates themselves, which range approximately .08 to .20. However, if we repeat an experiment eight times we might expect our average value to be accurate within a standard deviation of .014, which would imply that the resulting representative friction factor is accurate to within about 10 to 15 percent.

In general, all spectral results reflected these accuracy estimates. However, some changes in accuracy characteristics were observed for the JONSWAP spectral runs. This was because of the narrow banded nature of the JONSWAP spectrum, which is described in detail in Section 3.3.2. For these narrow banded experiments, Experiments F, G, H, and I, the three highest components had frequencies of 2.761, 3.375, and 4.295 rad/sec. The two lowest frequency components had radian frequencies of 2.271 and

2.454 rad/sec, respectively. Therefore, since the difference between these two frequencies is very small, a problem in resolution of the two components results.

This problem results due to the limitations of the Fast Fourier Transform (FFT) program, which, for the experiments completed, resolves the surface profile into 256 discrete components by transforming the surface profile records of 512 data points. For example, for the five-component JONSWAP spectra simulated, the five frequencies noted above would correspond to five distinct Fourier components (which are often referred to as "spikes"). These spikes are often identified by numbers that, for this case, would range between 0 and 255. The frequencies noted above would correspond to spike numbers 37, 40, 45, 55, and 70, with 37 being the lowest frequency, and 70 being the highest.

When simulating a spectrum, we define the frequencies of the various components such that they each exactly match one of the discrete Fourier components defined above. However, due to limitations of the discrete Fourier Analysis procedure and the experimental setup, this match will never be perfect. Thus, upon Fourier transformation, the energy associated with a component of interest will show up in (or "leak" into) adjacent components. Therefore, when two components are oscillating at similar frequencies, there will be some leakage of energy from one component to the other, which will likely vary somewhat for each experimental run completed. Because of this phenomenon, if we are trying to separate out the energy associated with each of the two components, we might expect a variability in our measurements. This variability would be reflected in a high standard deviation in the component amplitude measurements.

After tabulation of results from some of the experiments completed, this turned out to be the case, as can be seen in the amplitude statistics for Experiment G1, shown in

Tables 3.5A and 3.5B. In these tables, the standard deviation of measurements of amplitude for two lowest components ranged between .06 and .10 cm. The standard deviations for the associated changes in amplitude between Stations 1 and 2 ranged from .10 to .14 cm. However, the remaining components, Components 3, 4, and 5 (as noted in Tables 3.5A and 3.5B), had standard deviations that are roughly comparable to Pierson-Neumann experiments of the approximately the same intensity (Experiment S5, for example).

These high standard deviations would likely have significant effects on the friction factors that we find for attenuation associated with each of these two components. However, they should have a small impact on the friction factor associated with the total spectral attenuation. This could be shown by lumping these two components together as one component, and measuring a representative energy or amplitude of the resulting component. If this were done, we would expect that the friction factor (and associated standard deviation) for the single coupled component would be quite reasonable as compared to the separate friction factors for the two components. For example, when the two components are combined for Experiment G1, the standard deviations of the resultant amplitude equations are reduced significantly. Also, for the flat bed runs, the standard deviations associated with the estimates of change in amplitude are reduced from .088 cm (Component 1) and .175 cm (Component 2) to .078 cm for the coupled component. The fully developed bed runs show a similar trend, with the .1-cm standard deviations for amplitude change for each of the components being reduced to .074 cm for the coupled component.

As was suggested above, the JONSWAP spectral experiments proved that the higher variability in the two components had negligible impact on the total spectral friction factor. In other words, the standard deviations in the representative spectral friction factor for the JONSWAP experiments were comparable to those of the less sharply

Table 3.5
Amplitude Measurements for a JONSWAP spectrum

AMPLITUDE MEASUREMENTS FOR FLAT BED
(IN CM)

RUN ID	COMPONENT 1 STA 1	STA 2	DIFF	COMPONENT 2 STA 1	STA 2	DIFF	COMPONENT 3 STA 1	STA 2	DIFF	COMPONENT 4 STA 1	STA 2	DIFF	COMPONENT 5 STA 1	STA 2	DIFF
G113	1.780	1.846	0.066	1.846	1.741	-0.105	1.681	1.729	0.048	1.698	1.350	-0.348	1.552	1.595	0.043
G114	1.729	1.876	0.147	1.849	1.844	-0.005	1.740	1.596	-0.144	1.664	1.450	-0.214	1.577	1.600	0.023
G115	1.684	1.924	0.240	1.968	1.753	-0.215	1.660	1.570	-0.090	1.699	1.463	-0.236	1.574	1.618	0.044
G116	1.691	1.846	0.155	2.001	1.848	-0.153	1.662	1.622	-0.040	1.714	1.345	-0.369	1.544	1.609	0.065
G117	1.795	1.962	0.167	1.774	1.716	-0.058	1.730	1.594	-0.136	1.645	1.403	-0.242	1.573	1.590	0.017
G118	1.659	1.793	0.134	2.011	1.924	-0.087	1.702	1.665	-0.037	1.652	1.370	-0.282	1.591	1.596	0.005
G119	1.736	1.775	0.039	1.871	1.991	0.120	1.705	1.658	-0.047	1.705	1.364	-0.341	1.560	1.617	0.057
G120	1.809	1.742	-0.067	1.707	2.082	0.375	1.795	1.648	-0.147	1.681	1.341	-0.340	1.556	1.604	0.048
AVG	1.735	1.846	0.110	1.878	1.862	-0.016	1.709	1.635	-0.074	1.682	1.386	-0.297	1.566	1.604	0.038
STD	0.052	0.070	0.088	0.102	0.121	0.175	0.042	0.047	0.064	0.024	0.045	0.056	0.014	0.010	0.019

AMPLITUDE MEASUREMENTS FOR FULLY DEVELOPED BED
(IN CM)

RUN ID	COMPONENT 1 STA 1	STA 2	DIFF	COMPONENT 2 STA 1	STA 2	DIFF	COMPONENT 3 STA 1	STA 2	DIFF	COMPONENT 4 STA 1	STA 2	DIFF	COMPONENT 5 STA 1	STA 2	DIFF
G101	1.719	1.781	0.062	1.886	1.773	-0.113	1.716	1.530	-0.186	1.673	1.415	-0.258	1.571	1.572	0.001
G102	1.734	1.762	0.028	1.914	1.897	-0.017	1.763	1.519	-0.244	1.671	1.310	-0.361	1.553	1.575	0.022
G103	1.772	1.682	-0.090	1.874	1.979	0.105	1.653	1.587	-0.066	1.683	1.297	-0.386	1.584	1.566	-0.018
G104	1.727	1.650	-0.077	1.901	1.822	-0.079	1.612	1.546	-0.066	1.655	1.314	-0.341	1.566	1.571	0.005
G105	1.870	1.769	-0.101	1.698	1.736	0.038	1.653	1.608	-0.045	1.687	1.423	-0.264	1.563	1.553	-0.015
G106	1.729	1.870	0.141	1.820	1.734	-0.086	1.823	1.494	-0.329	1.684	1.344	-0.340	1.551	1.568	0.017
G107	1.670	1.825	0.155	1.985	1.828	-0.157	1.687	1.503	-0.184	1.675	1.307	-0.368	1.585	1.574	-0.011
G108	1.754	1.744	-0.010	1.926	1.859	-0.067	1.649	1.553	-0.096	1.704	1.338	-0.366	1.555	1.552	-0.003
G109	1.854	1.856	0.002	1.694	1.646	-0.048	1.672	1.579	-0.093	1.716	1.317	-0.399	1.562	1.567	0.005
G110	1.671	1.842	0.171	1.981	1.697	-0.284	1.674	1.517	-0.157	1.677	1.415	-0.262	1.582	1.583	0.001
G111	1.859	1.778	-0.081	1.819	1.596	-0.223	1.633	1.755	0.122	1.635	1.378	-0.257	1.588	1.561	-0.027
G112	1.942	1.764	-0.178	1.740	1.661	-0.079	1.636	1.766	0.130	1.644	1.414	-0.230	1.605	1.563	-0.042
AVG	1.775	1.777	0.002	1.853	1.769	-0.084	1.681	1.580	-0.101	1.675	1.356	-0.319	1.573	1.567	-0.005
STD	0.083	0.063	0.108	0.096	0.108	0.101	0.058	0.087	0.129	0.022	0.047	0.058	0.016	0.009	0.017

peaked Pierson-Neumann Spectrum. Since the variability in friction factors for the two low-frequency components did not affect the representative spectral friction factor, it was not deemed necessary to use a single coupled component for the two lowest frequency components.

3.7 Bedform Analysis

To relate wave attenuation to bedform characteristics, an extensive bedform analysis is obviously essential. Procedures for quantifying the response of the sediment bed to wave agitation were presented in Rosengaus (1987). These procedures include methods for characterizing the transcient case, which we commonly refer to as "the developing bed," and the case that is statistically independent of time, which is usually identified as "the fully developed bed." The developing bed may include a sand bed that is developing from an initially flat bed, as was the case for all experiments completed in this study. Alternatively, it may include a redeveloping sand bed that was initially in a fully developed state resulting from another wave climate, which was studied in detail in Rosengaus (1987).

For this study, Chris Rehman, a UROP (Undergraduate Research Opportunities Program) student, completed the majority of the bedform analysis. His work basically made use of the methods and procedures that are detailed in Rosengaus (1987). Therefore, a brief summary of the basic requirements for both the developing bed and fully developed bed is in order.

3.7.1 The Developing Bed

M. Rosengaus observed that when the sediment bed in the wave flume was developing from an initially flat state, ripples initially formed at discontinuities, or,

more specifically, at the junctions between the glass side panels of the flume. At these locations, the ripples would grow as patches, in a random and chaotic manner, and eventually cover the sediment bed. Therefore, to help simplify the procedure, "originator ripples" were set at the junctions by tracing a line across the flume using a wooden stick. This procedure forced the ripple patch to extend across the width of the flume. Thus, the ripple patch would grow in an organized manner.

In addition, the appearance of the growing patch followed a trend. It was observed that ripples that were located a certain number of crests behind the expanding patch front attained a geometry that was very similar to their fully developed state. The region between the patch front (at the flat bed) and these fully developed ripples appeared to form a type of envelope. In any event, with this organized patch growth, some parameters could be defined to characterize the development of the sediment bed.

The first of these parameters is the ripple patch expansion speed, C_b, which is the sum of the patch propagation speed observed in the wave direction or $+X$ direction, C_{b+}, and that opposite of the wave direction or $-X$ direction, C_{b-}. Therefore,

$$C_b = C_{b+} + C_{b-} \tag{3.33}$$

These patch propagation speeds are measured by noting the location of the patch fronts at various times during the experimental run.

The next parameter of interest is the time it takes a bedform crest to develop from its first appearance to a fully developed state, t_f. To develop an estimate for this parameter, the observation noted above, in which fully developed ripples and associated envelopes appeared, was used to advantage. The generalized parameter, t_f, is actually the average of t_{f+} and t_{f-}. t_{f+} is determined by using information observed for the patch

propagating in the +X direction, and t_{f-} is determined using information observed for the patch propagating in the -X direction.

To determine t_{f+} and t_{f-}, a procedure was developed that would help to minimize the subjectiveness of the observations. First, the number of bedforms experiencing growth within the developing envelope (described above), which we can call N_{FB}, is estimated. Then, if we consider the +X direction as an example, the time for the bedform to develop from its first appearance to its fully developed state is equal to the time it takes for N_{FB} new crests to appear. To estimate t_f, another parameter, the time for a development of each new bedform, t_{new}, must first be obtained by determining the time elapsed since the beginning of the run and dividing that by the total number of ripples in the patch of interest. If we consider the +X direction as an exapmle, then the time for the bedform to develop from its first appearance to its fully developed state may be estimated by:

$$T_{f+} = N_{FB+} T_{new} \tag{3.34}$$

Obviously, the accuracy of this method is limited since it is dependent on the subjective judgement of the observer to determine whether ripples are fully developed and to locate the front of the ripple patch. However, this procedure does serve as a quantitative indicator of the response of the sediment bed to wave agitation. Again, the details of this procedure are thoroughly discussed and clarified in Rosengaus (1987).

3.7.2 The Fully Developed Bed

As noted above, the fully developed bed is defined to be in a state in which any bedform parameters are statistically independent of time. The parameters that are commonly accepted to be relevant to the fully developed bed include the

nondimensional bedform height, η/A_b, length, λ/A_b, steepness, η/λ, and the asymmetry, α. The analysis of these parameters, which are further described in Chapter 5, was completed by taking pictures of the bedform profiles at a number of locations along the test section of the wave flume. These pictures were then analyzed to obtain statistics associated with the bedform parameters of interest. This analysis required the use of a variety of equipment and computer programs. The procedures and materials associated with this analysis are described in detail in Rosengaus (1987). However, they can be briefly summarized.

The experimental equipment for the bedform analysis includes an Olympus OM10 35-mm camera and a variety of photographic lamps. As noted above, a number of photographs were taken of the bedform profile at various locations along the length of the test section of the flume. To analyze these photographs (which were in the form of slides), a slide projector was used to project the bedform profile onto a CALCOMP 9000 digitizing tablet. Then, an IBM XT computer was used to run a number of programs to process the digitized profile.

The first processing program used converts the output from the digitizer information into a record of equally spaced points representing the bedform profile. Next, a program digitally filters the profile record to eliminate long variations not associated with the individual bedforms. Once this is completed, another program counts the individual bedforms, measures their heights and lengths, and computes relevant statistics. In addition, another program is used to estimate the statistics on the asymmetry of the bedforms. Finally, a program is used to plot the profiles. Basically, this software provided all necessary information from which the characteristics of the bedforms could be quantified in a statistically objective manner.

4 EXPERIMENT DESIGN

4.1 Experimental Procedure

4.1.1 Monochromatic Waves

The experimental procedure necessary for setting up monochromatic wave experiments in the wave flume is described in detail by Rosengaus (1987). However, the procedure may be briefly summarized as a few steps.

First, the desired wave characteristics (amplitude, frequency, and wavelength) are determined for the region of the flume that includes the sand layer. Next, these wave characteristics are traced back down the ramp to define the characteristics of waves that must be generated by the wavemaker. This computation is completed by using a conservation of energy flux argument for a wave passing over an abrupt change in depth (as per Ippen (1966)).

Once this is completed, a correction factor is computed to ensure that the second harmonic free wave is properly eliminated in the test section. This free harmonic, which shows up when using a piston-type wavemaker to generate Stokes Waves, is discussed in Chapter 3. In this case, the transition over the ramp requires us to modify the wavemaker motion to ensure the the free harmonic is sufficiently eliminated in the test section (over the sand bed). As discussed in Rosengaus (1987), the component of wavemaker motion that is normally used to eliminate the free harmonic can be thought of as a "counter-second harmonic free wave." One might expect that this "counter-wave" would normally be computed based on the deeper depth at the wavemaker (usually 70 cm). However, the necessary "counter-wave" would have to be larger if the depth at the wavemaker were the same as that over the sand bed (usually 60 cm). Therefore, since the free harmonic must be eliminated in the test section, we might

expect that the magnitude of this counter-second harmonic free wave must be larger than that normally computed for the deeper depth at the wavemaker. Accordingly, a correction factor is defined that may be used to adjust the amplitude of the component of wavemaker motion that eliminates the second harmonic free wave.

As is thoroughly explained in his thesis, M. Rosengaus obtained this correction factor by determining what the amplitude of the free second harmonic would be if the depth at the wavemaker were the same as that over the sand bed. Then, he adjusted this amplitude as necessary to accommodate the deeper depth at the wavemaker by making use of the conservation of energy flux computation. The correction factor would then be this amplitude divided by the theoretical free harmonic amplitude. As detailed in Rosengaus (1987), this procedure was tested experimentally. Although it was shown that removal of the free harmonic could be improved by experimental "fine tuning," the procedure noted above was shown to be sufficiently accurate to remove the free harmonic for the experiments completed. After the wavemaker recalibration, this procedure for calculating this correction factor was tested. Experimentally, it was shown that the removal of the second harmonic was improved if this computed correction factor was reduced by about 15 percent. Therefore, for the monochromatic wave experiments using the .12-mm sand, this reduced correction factor was used.

4.1.2 Spectral Waves

In addition to a number of spectral experiments using the 0.12-mm sand, a number of spectral experiments were also completed using the 0.20-mm sand. All of these experiments were simply a continuation of the spectral experiments completed by M. Rosengaus. Therefore, as for the monochromatic wave experiments, a detailed description of the design procedure for these experiments can be found in Rosengaus (1987). Again, however, the design procedure can be summarized in a few steps.

For the experiments of interest, the spectral intensity or spectral energy may be expressed in terms of a representative monochromatic wave, as follows:

$$E = \int_0^\infty S_{\eta\eta}(\omega)d\omega = \frac{1}{2}a_{rep}^2 \qquad (4.1)$$

Once the spectral energy has been defined (or an amplitude and radian frequency for a representative monochromatic wave has been chosen), the shape of the spectrum to be simulated must be determined. For the earlier experiments completed (preliminary experiments and Experiments C, D, and E), a Pierson-Neumann spectrum was simulated. This spectrum is a relatively broad-banded spectrum in which the energy is distributed over a wide range of frequencies.

The remainder of the experiments simulated a JONSWAP spectrum, which is a relatively narrow-banded spectrum. The JONSWAP spectrum is commonly accepted as the more realistic of the two spectra. The parameters and relationships describing both of these spectra are summarized in Section 3.3.2. In addition, they are plotted in Figures 3.4 and 3.5.

For spectrum simulation, the theoretical continuous wave spectrum is partitioned into five components of equal energy using a numerical integration program. Since we have defined the total desired energy for the spectrum, we can simply divide this equally among the five components and thereby obtain design amplitudes for each of the spectral components. Then, the frequency for each component can be taken as the centroid of the region under the spectral curve that it will represent.

This choice of a five-component spectrum was advantageous because it provided a wide range of frequencies to represent the frequency distribution that might be found in

a real spectrum. It also reduced the problems posed by some of the earlier eight-component spectral representations.

The first advantage of reducing the number of components to five involved the size limitations of the wave flume and accuracy of the measuring system. Basically, the depth of the flume limits the total allowable surface height. The concepts of superposition would indicate that, considering this size restriction, if we have fewer components in the spectrum the amplitude of each component can be larger. The accuracy of the amplitude measurements is limited by the measuring system, as is discussed in Section 3.6.3. In effect, with larger amplitudes for each of the components, the relative error will be smaller. Therefore, we will get a more accurate determination of the attenuation and friction factor.

It is also advantageous because, with fewer components, fewer higher harmonics and nonlinear interactions result. For example, if two components included in a spectrum are ω_1, and ω_2, we expect second harmonic components oscillating at frequencies of $(2\omega_1)$, and $(2\omega_2)$ and third harmonic components oscillating at $(3\omega_1)$ and $(3\omega_2)$. In addition, the two frequency components will interact nonlinearly to produce components oscillating at $|\omega_1+\omega_2|$ and $|\omega_1-\omega_2|$. We must make sure that these additional components do not oscillate at frequencies that coincide with those of other components in our spectrum and affect our amplitude and attenuation estimates.

Once the frequencies of each of the components have been chosen, they must be adjusted to complement the wave gauge sampling parameters. This requirement arises because we are using a number of discrete sample points over a finite sampling period or "window" to resolve the components of the water surface profile. Due to the characteristics of discrete Fourier transforms over finite sampling periods, the ratio of the sampling period to any component's period must be an integer for accurate

resolution. This slight adjustment assures that the energy leakage around the frequency spike of interest will be minimized.

After the frequencies have been finalized, ensuring that the energy leakage is minimized and nonlinear components have negligible impact, the final characteristics of the wave spectrum that will be generated over the sand bed may be defined. These characteristics may then be used to obtain the amplitudes of components in the deeper water at the wavemaker. This is completed by applying the energy flux conservation equations, also mentioned in Section 4.1.1, to each of the components of the spectrum. Then, the spectrum may be generated by making use of a random number generator for each of the phases of the oscillatory components to be generated.

4.2 Description of Experiments

4.2.1 Monochromatic Waves

All monochromatic wave experiments associated with this thesis were completed using 0.12-mm silica sand in the flume. These experiments, being an extension of the experiments completed by M. Rosengaus using the 0.2-mm sand, were performed in a similar manner. As for the previous set of monochromatic wave experiments, "typical wave conditions" were considered to be those characterized by

$h = 60.0$ cm

$a = 6.0$ cm

$L = 600$ cm

$h/L = 1/10$

$\omega = 2.39185$ rad/sec

$T = 2.627$ sec

The monochromatic wave experiments completed were:

Experiment A. This experiment, designed with typical wave conditions except for the wave amplitude, was intended to better define the initiation-of-motion condition for waves propagating over an initially flat bed. Therefore, no "originator" ripples were formed at the beginning of the experiment. The amplitudes used were 2.0, 2.5, 3.0, 3.5, and 4.0 cm. Runs with progressively higher wave amplitudes were completed, and the progression from onset of movement to ripple development and ripple patch progression was observed.

Experiment B. Again, the typical wave conditions were used with the exception of the amplitude, which again was progressively increased. Here, however, the amplitudes used were 4.0, 5.0, 5.5, 6.0, 7.0, and 8.0 cm. For this experiment, the characteristics of the developing bed were analyzed. In addition, the procedure was to determine attenuation over a developed bed, and also to record the bedform characteristics. Therefore, the bed was allowed to reach a fully developed or steady state for each amplitude used. In this way, quantitative relationships between bedforms and the associated wave attenuation could be developed.

A summary of the monochromatic wave experiments is shown in Table 4.1.

4.2.2 Spectral Waves

The spectral experiments in this study included five experiments for which the 0.2-mm sand was used, and eight experiments for which the 0.12-mm sand was used. The spectral experiments were completed with the purpose of characterizing any general relationships associated with the wave/sand interaction for an arbitrarily chosen spectrum. Also, the experiments were intended to test the assumption of using a

Table 4.1
Description of the Monochromatic Wave Experiments

Monochromatic Wave Experiments

Expt ID	Run #	depth (cm)	frequency (rad/sec)	wavenumber (1/cm)	h/L	amplitude (cm)	wavelength (cm)	period (sec)	Ursell #	# of attenuation measurements	Bedform Analysis
A	1	60	2.39185	0.0104719	0.1	2.00	600	2.627	6.67	7	no
	2					2.50			8.33	6	no
	3					3.00			10.00	4	no
	4					3.50			11.67	12	no
	5					4.00			13.33	12	no
B	1	60	2.39185	0.0104719	0.1	4.00	600	2.627	13.33	12	yes
	2					5.00			16.67	8	yes
	3					6.00			20.00	6	yes
	4					7.00			23.33	11	yes
	5					8.00			26.67	8	yes
	6					5.50				8	yes

representative monochromatic wave to characterize the attenuation associated with a wave spectrum.

The spectral experiments completed can be considered in two groups:

4.2.2.1 Spectral Experiments Using the 0.20-mm Sand

Experiment S1. The primary purpose of this experiment was to verify the reproduction of spectral experiments completed previously by M. Rosengaus. For this experiment, a five-component design spectrum was used for which the associated spectral energy was set equivalent to one-half of the energy associated with the typical monochromatic wave (defined in Section 4.2.1). As for Experiments S2 through S5, a Pierson-Neumann spectrum was simulated.

Experiment S2. This experiment was also used as additional verification of the spectral experiments and also included analysis of the developing bed. The experiment included another representation of the same spectrum. Here, the spectrum was generated using a different random seed for the random number generator routine in the wave generation program. Therefore, the relative phases for each of the components were different from those of the components generated in Experiment S1. Again, however, the spectral energy was taken as one-half of that associated with the typical monochromatic wave.

Experiment S3. This experiment was completed after changes were made to the wavemaker to increase its output so that higher waves could be generated. Because of these changes, the wavemaker was recalibrated. After this recalibration (which is discussed in Section 3.4), this experiment was completed to verify proper wavemaker operation and to test the accuracy of the measuring system. The energy was equal to

that of the typical monochromatic wave. The developing bed was also analyzed in this experiment.

Experiment S4. This experiment, also completed after wavemaker recalibration, was completed to study the wave/sand interaction for higher spectral energies. Therefore, the spectral energy was taken to be equal to that of the typical monochromatic wave. No developing bed information was obtained for this experiment.

Experiment S5. Here, wave/sand interaction for lower spectral intensities (including that associated with the developing bed) was studied. This experiment provided a comparison to Experiment S4, which yielded information regarding high spectral intensities. For Experiment S5, the spectral energy was taken to be equal to one-half that of the typical monochromatic wave. In addition, Experiments S4 and S5 both were used to study the accuracy limitations of the experimental setup, and were used as examples in Section 3.6.3.2. The Pierson–Neumann spectral experiments are summarized in Table 4.2A.

4.2.2.2 Spectral Experiments Using the 0.12-mm Sand

Experiment C. For this experiment, two realizations of the spectrum were generated, which means that experiments were completed for two different random seeds to define the phase relationships. The design spectral energy was taken to be equal to three-fourths of the energy associated with the typical monochromatic wave. Developing bed information was obtained for this experiment. The developing bed was also analyzed for Experiment E. However, for Experiments D and F through J, no developing bed information was obtained.

Table 4.2A

Description of the Spectral Experiments Using .20 mm Sand

Spectral Wave Experiments using .20 mm sand

Expt ID	Spectrum Simulated	Component #	depth (cm)	frequency (rad/sec)	wavenumber (1/cm)	h/L	amplitude (cm)	wavelength (cm)	period (sec)	Ursell #	# of attenuation measurements		Bedform Analysis
											flat bed	FDB	
S1	Pierson Neumann	1	50.0	2.011	0.0094021	0.07	1.900	668	3.12	13.58	2	3	no
		2		2.450	0.0116613	0.09	1.900	539	2.56	8.83			
		3		2.890	0.0140516	0.11	1.900	447	2.17	6.08			
		4		3.456	0.0173734	0.14	1.900	362	1.82	3.98			
		5		4.650	0.0256927	0.20	1.900	245	1.35	1.82			
S2	Pierson Neumann	1	50.0	2.011	0.0094021	0.07	1.900	668	3.12	13.58	4	4	yes
		2		2.450	0.0116613	0.09	1.900	539	2.56	8.83			
		3		2.890	0.0140516	0.11	1.900	447	2.17	6.08			
		4		3.456	0.0173734	0.14	1.900	362	1.82	3.98			
		5		4.650	0.0256927	0.20	1.900	245	1.35	1.82			
S3	Pierson Neumann	1	50.0	2.011	0.0094021	0.07	2.680	668	3.12	19.15	7	5	yes
		2		2.450	0.0116613	0.09	2.680	539	2.56	12.45			
		3		2.890	0.0140516	0.11	2.680	447	2.17	8.57			
		4		3.456	0.0173734	0.14	2.680	362	1.82	5.61			
		5		4.650	0.0256927	0.20	2.680	245	1.35	2.56			
S4	Pierson Neumann	1	50.0	1.902	0.0088616	0.07	2.680	709	3.30	21.56	10	8	no
		2		2.393	0.0113595	0.09	2.680	553	2.63	13.12			
		3		2.823	0.0136737	0.11	2.680	460	2.23	9.05			
		4		3.375	0.0168777	0.13	2.680	372	1.86	5.94			
		5		4.602	0.0253179	0.20	2.680	248	1.37	2.64			
S5	Pierson Neumann	1	50.0	1.902	0.0088616	0.07	1.900	709	3.30	15.28	12	8	yes
		2		2.393	0.0113595	0.09	1.900	553	2.63	9.50			
		3		2.823	0.0136737	0.11	1.900	460	2.23	6.42			
		4		3.375	0.0168777	0.13	1.900	372	1.86	4.21			
		5		4.602	0.0253179	0.20	1.900	248	1.37	1.87			

Table 4.2B
Description of the Pierson–Neumann Spectral Experiments Using .12 mm Sand

Pierson-Neumann Spectral Wave Experiments using .12 mm sand

Expt ID	Spectrum Simulated	Component #	depth (cm)	frequency (rad/sec)	wavenumber (1/cm)	h/L	amplitude (cm)	wavelength (cm)	period (sec)	Ursell #	# of attenuation measurements flat bed	FDB	Bedform Analysis
C1	Pierson Neumann	1	60.0	1.963	0.0084253	0.08	2.324	746	3.20	11.97	12	8	yes
		2		2.393	0.0104776	0.10	2.324	600	2.63	7.74			
		3		2.823	0.0126672	0.12	2.324	496	2.23	5.29			
		4		3.375	0.0157446	0.15	2.324	399	1.86	3.43			
		5		4.541	0.0236349	0.23	2.324	266	1.38	1.52			
C2	Pierson Neumann	1	60.0	1.963	0.0084253	0.08	2.324	746	3.20	11.97	8	4	yes
		2		2.393	0.0104776	0.10	2.324	600	2.63	7.74			
		3		2.823	0.0126672	0.12	2.324	496	2.23	5.29			
		4		3.375	0.0157446	0.15	2.324	399	1.86	3.43			
		5		4.541	0.0236349	0.23	2.324	266	1.38	1.52			
D1	Pierson Neumann	1	50.0	1.963	0.0091667	0.07	2.680	685	3.20	20.15	8	12	yes
		2		2.393	0.0113595	0.09	2.680	553	2.63	13.12			
		3		2.823	0.0136737	0.11	2.680	460	2.23	9.05			
		4		3.375	0.0168777	0.13	2.680	372	1.86	5.94			
		5		4.541	0.0248407	0.20	2.680	253	1.38	2.74			
D2	Pierson Neumann	1	50.0	1.963	0.0091667	0.07	2.680	685	3.20	20.15	4	8	yes
		2		2.393	0.0113595	0.09	2.680	553	2.63	13.12			
		3		2.823	0.0136737	0.11	2.680	460	2.23	9.05			
		4		3.375	0.0168777	0.13	2.680	372	1.86	5.94			
		5		4.541	0.0248407	0.20	2.680	253	1.38	2.74			
E1	Pierson Neumann	1	60.0	1.963	0.0084253	0.08	2.078	746	3.20	10.70	8	8	yes
		2		2.393	0.0104776	0.10	2.078	600	2.63	6.92			
		3		2.823	0.0126672	0.12	2.078	496	2.23	4.73			
		4		3.375	0.0157446	0.15	2.078	399	1.86	3.06			
		5		4.541	0.0236349	0.23	2.078	266	1.38	1.36			

Table 4.2C
Description of the JONSWAP Spectral Experiments Using .12 mm Sand

JONSWAP Spectral Wave Experiments using .12 mm sand

Expt ID	Spectrum Simulated	Component #	depth (cm)	frequency (rad/sec)	wavenumber (1/cm)	h/L	amplitude (cm)	wavelength (cm)	period (sec)	Ursell #	# of attenuation measurements flat bed	FDB	Bedform Analysis
F1	JONSWAP	1	50.0	2.270	0.0107219	0.09	2.680	586	2.77	14.73	8	8	yes
		2		2.454	0.0116821	0.09	2.680	538	2.56	12.40			
		3		2.761	0.0133345	0.11	2.680	471	2.28	9.52			
		4		3.375	0.0168777	0.13	2.680	372	1.86	5.94			
		5		4.295	0.0229977	0.18	2.680	273	1.46	3.20			
F2	JONSWAP	1	50.0	2.270	0.0107219	0.09	2.680	586	2.77	14.73	8	8	yes
		2		2.454	0.0116821	0.09	2.680	538	2.56	12.40			
		3		2.761	0.0133345	0.11	2.680	471	2.28	9.52			
		4		3.375	0.0168777	0.13	2.680	372	1.86	5.94			
		5		4.295	0.0229977	0.18	2.680	273	1.46	3.20			
G1	JONSWAP	1	60.0	2.270	0.0098787	0.09	2.078	636	2.77	7.78	8	12	yes
		2		2.454	0.0107812	0.10	2.078	583	2.56	6.54			
		3		2.761	0.0123447	0.12	2.078	509	2.28	4.98			
		4		3.375	0.0157446	0.15	2.078	399	1.86	3.06			
		5		4.295	0.0217794	0.21	2.078	288	1.46	1.60			
H1	JONSWAP	1	50.0	2.270	0.0107219	0.09	2.400	586	2.77	13.19	8	8	no
		2		2.454	0.0116821	0.09	2.400	538	2.56	11.11			
		3		2.761	0.0133345	0.11	2.400	471	2.28	8.53			
		4		3.375	0.0168777	0.13	2.400	372	1.86	5.32			
		5		4.295	0.0229977	0.18	2.400	273	1.46	2.87			
I1	JONSWAP	1	50.0	2.270	0.0107219	0.09	2.828	586	2.77	15.54	8	4	yes
		2		2.454	0.0116821	0.09	2.828	538	2.56	13.09			
		3		2.761	0.0133345	0.11	2.828	471	2.28	10.05			
		4		3.375	0.0168777	0.13	2.828	372	1.86	6.27			
		5		4.295	0.0229977	0.18	2.828	273	1.46	3.38			
J1	JONSWAP	1	50.0	2.270	0.0107219	0.09	3.000	586	2.77	16.48	4	8	no
		2		2.454	0.0116821	0.09	3.000	538	2.56	13.89			
		3		2.761	0.0133345	0.11	3.000	471	2.28	10.66			
		4		3.375	0.0168777	0.13	3.000	372	1.86	6.65			
		5		4.295	0.0229977	0.18	3.000	273	1.46	3.58			

Experiment D. Here, the energy was designed to be that of the typical monochromatic wave to obtain information about spectral dissipation associated with high spectral intensities. Again, two realizations were generated.

Experiment E. In this case, a slightly smaller spectral intensity was studied in an effort to characterize spectral wave/sand interaction for spectral waves of lower energy. The design spectral energy was set equal to three-fifths of that of the typical monochromatic wave. As noted above, the developing bed was analyzed for Experiment E.

Experiment F. For this experiment, a JONSWAP shallow water spectrum was used. All of the previous experiments had shown ψ'/ψ_c to be a useful dimensionless parameter for characterizing the relatively broad Pierson-Neumann spectrum. Therefore, for this case, the purpose was to test the applicability of ψ'/ψ_c for the JONSWAP spectrum. In this case, the design spectral energy was set to equal the energy associated with the typical monochromatic wave and two realizations of the same spectrum were simulated.

Experiment G. This experiment also simulated the JONSWAP spectrum and was completed with the same intention as Experiment F. In this case, however, the spectral energy was set equal to one-half of that associated with the typical monochromatic wave. Here, only one realization was completed.

Experiment H. Here, one realization of a JONSWAP spectrum was simulated. The spectral energy was set at four-fifths of that of the typical monochromatic wave.

Experiment I. For this case, one realization of a JONSWAP spectrum was tested using a design spectral energy of one and one-tenth of that associated with the typical monochromatic wave.

Experiment J. This was the final experiment completed using a JONSWAP spectrum. In this case, the intention was to obtain the highest possible spectral intensity given the constraints of the experimental apparatus. To accomplish this, the input amplitudes for each of the five components were taken to be 3.0 cm and the random seed was chosen to prevent any wave breaking in the flume. The design spectral energy for this experiment was approximately equal to one and one-quarter that of the typical monochromatic wave.

The spectral experiments using the .12-mm sand are summarized in Tables 4.2B and 4.2C. In Table 4.2B, the Pierson-Neumann experiments are presented, while the JONSWAP spectral experiments are summarized in Table 4.2C.

When long waves pass over a flat sediment bed, there will be attenuation of the waves due to bottom friction. As we increase the wave energy, sand grain motion will occur and will eventually lead to development of bedforms in the sediment bed. We would expect these two phenomena to be interrelated, since the bedform characteristics produce a roughness that affects the friction factor associated with the wave attenuation. Ideally, we would hope that, with knowledge of the characteristics of the wave train or spectrum propagating over the sand bed, we would be able to predict bedform geometry, and from this information estimate a relative roughness and friction factor describing wave attenuation. Therefore, in this study, we first consider the bedform characteristics resulting from the waves passing over the bed. In this chapter, the bedform data for the experiments using .12-mm sand, and those completed by M. Rosengaus using the .20-mm sand are compared to an existing relationship summarized in Chapter 2.

5.1 Initiation of Motion

The initial motion mentioned above was experimentally characterized by running waves of increasingly higher amplitude over a completely flat sand bed. Detailed observations were then made in an attempt to define the wave intensity associated with incipient sand grain motion.

A specific initiation of motion condition was actually difficult to define. However, four separate conditions were observed:

1. The "scraper" used to flatten the sand bed occasionally left small longitudinal depressions that were parallel to the wave direction. At relatively low wave intensities, ripples that were less than about 1 mm in height were observed forming in these

depressions. It appeared as though these small ripples consisted of the finer sands of the sediment's grain size distribution. Also, since these ripples did not propagate or grow, they were assumed to be of insignificant importance.

2. At a slightly higher wave intensity, which was quite close to that associated with the critical Shields criterion, a general grain motion was observed at any irregularities in the sand bed (which are infrequent yet unavoidable considering limitations in flattening the sand bed).

3. At a wave intensity that was slightly higher than critical, ripples were found to form at the irregularities noted above and also would propagate (very slowly) in both the downstream and upstream ("downwave" and "upwave") directions.

4. For regions of the bed that were perfectly flat, no motion was observed for the wave intensities tested. It was obvious that the motion associated with these perfectly flat regions would not correspond to Shields criterion. In addition, flat beds of this type would not be found in nature, and, therefore, were not considered further.

To better characterize the first three of the initiation-of-motion conditions, they are plotted against Shields diagram for initiation of motion in Figure 5.1. In this plot, information regarding the .20-mm sand is also included. This information was obtained from observations made during the .20-mm sand experiments, in which the same four conditions were noticed (although a criterion was not defined for Condition No. 1). Basically, review of Figure 5.1 shows a relatively good correspondence with Shields Criterion.
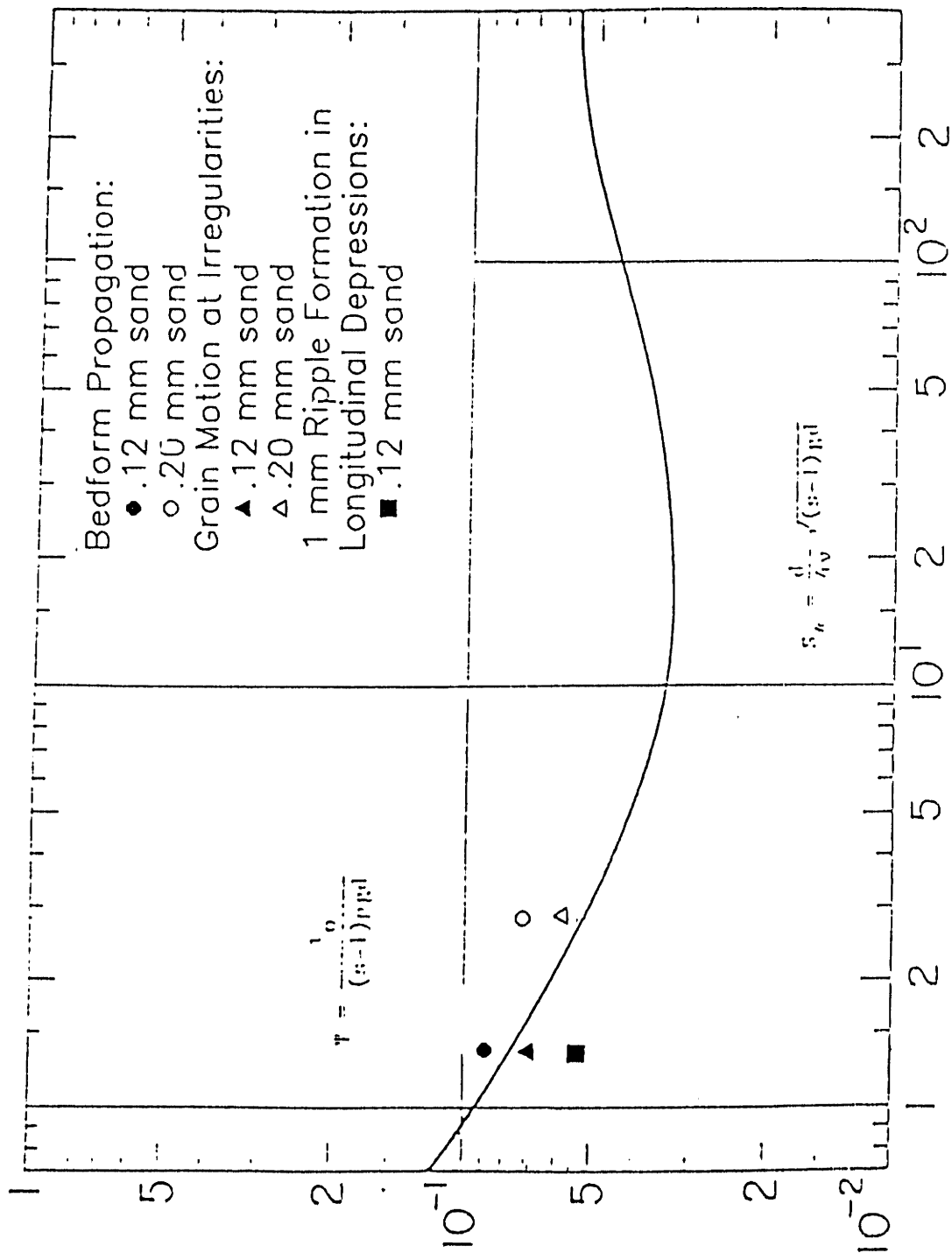
Figure 5.1   Experimental initiation of motion data, plotted against the critical
Shields parameter for initiation of motion in steady flow

5.2 The Developing Bed

As is described in Section 3.7, to characterize the transition between a flat sediment bed and fully developed bed, the growth of ripple "patches" was observed. Two parameters are used to describe this ripple patch growth. The first parameter is the patch propagation speed normalized by the horizontal bottom velocity, C_b/U_b. The second is the time to full development of a single ripple, normalized by the wave period, t_f/T.

The data associated with the first of these parameters, C_b/U_b, is plotted against ψ'/ψ_c in Figure 5.2. In this figure, the filled symbols represent the C_b/U_b for the patch growth in the direction of wave propagation (+X direction). The open symbols represent C_b/U_b for patch growth in the direction opposite to that of wave propagation (-X direction). It is apparent that there is a rather wide scatter in the data, which is expected due to the unavoidable subjectivity the estimates of different observers.

First, review of this figure shows that the ripple patch growth, as expected, is generally larger in the direction of wave propagation. For lower values of ψ'/ψ_c, the differences between patch growth in the +X directions and -X directions are relatively small, which seems reasonable since we would expect linearity to dominate at these lower wave intensities. Also, in general, the relationship between C_b/U_b and ψ'/ψ_c matches relatively well for the two sands, although there is a significant difference between the results of the monochromatic wave experiments for the two sands at higher values of ψ'/ψ_c (greater than a ψ'/ψ_c of 2, say). However, the data at these higher values is limited. In addition, for the experiments with the .12-mm sand, it was found that the measurement of patch growth was extremely difficult because of the rapid rates of growth and spontaneous ripple growth occurring at locations other than the front of the originator ripple. Therefore, based on the available data, no clear
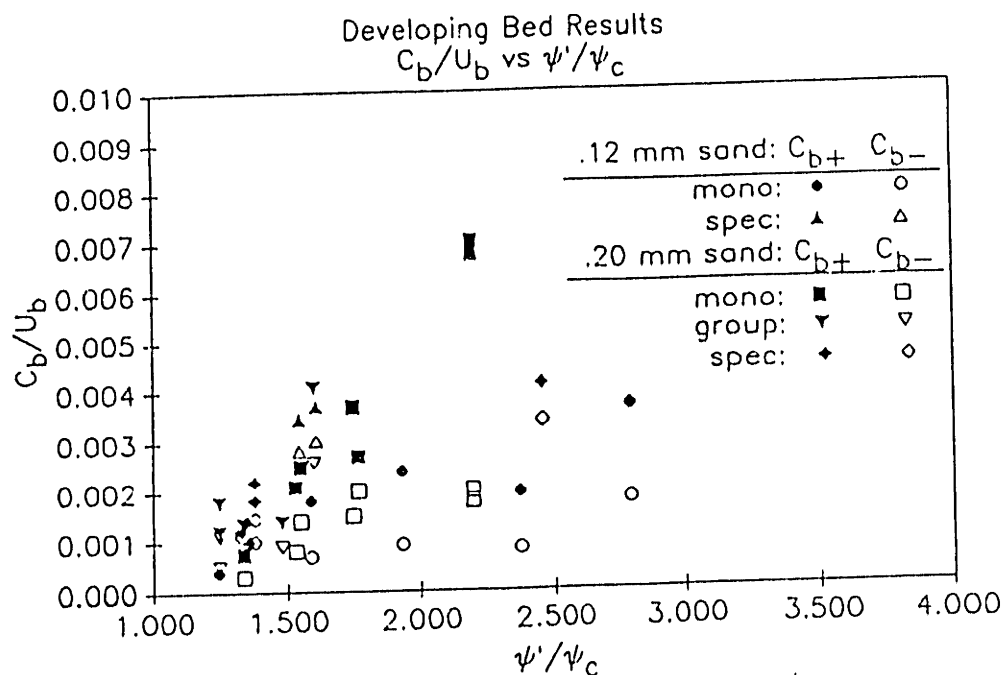
Developing Bed Results
C_b/U_b vs ψ'/ψ_c

Figure 5.2   Observations of C_{b+} and C_{b-} for different wave conditions

Developing Bed Results
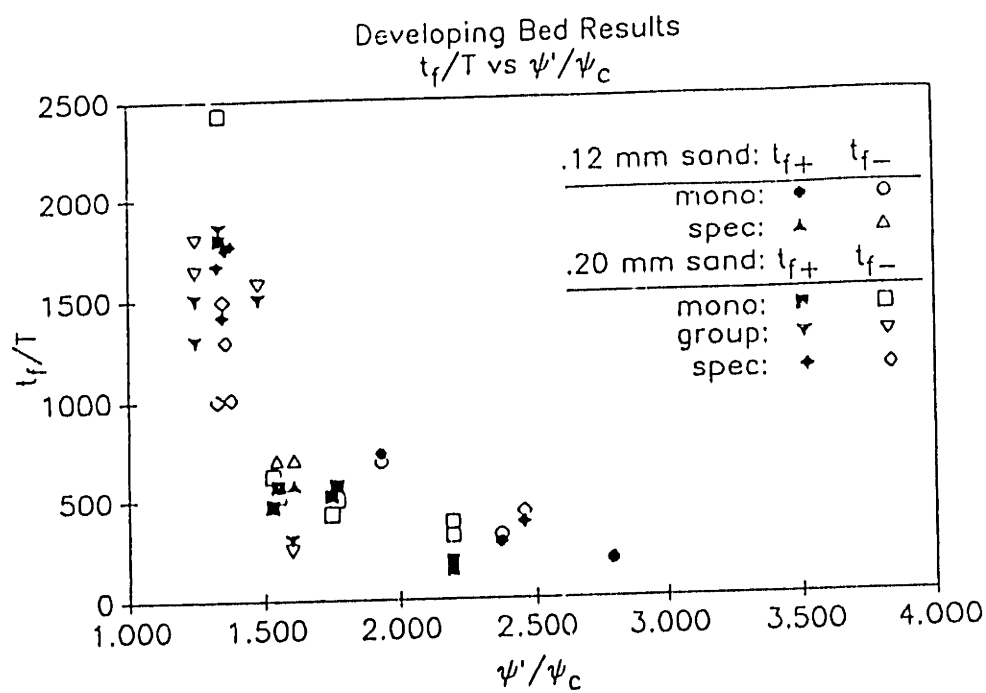## t_f/T vs ψ'/ψ_c

Figure 5.3   Observations of t_{f+} and t_{f-} for different wave conditions

distinction between the results for the two sands can be identified and, for the most part, the Relative Shields Parameter appears to be a good indicator of wave sediment interaction over the developing bed.

Additional review of Figure 5.2 reveals that the spectral results, for which the concepts of the representative Shields Parameter and representative horizontal bottom velocity (discussed in Section 2.2.2.) have been used, generally match the monochromatic results. This implies that the use of the representative monochromatic wave in this manner is appropriate for characterization of the response of the developing sediment bed. Of course, this conclusion is again based on limited data with limited accuracy, especially for the higher wave intensities.

In the next plot, Figure 5.3, t_f/T is plotted against ψ'/ψ_c. In this figure, all data appears to fall on one general curve. Therefore, this figure verifies the conclusions noted in the above paragraphs. Review of this figure shows that the parameter t_f/T asymptotically approaches zero as ψ'/ψ_c gets large. Also, as ψ'/ψ_c approaches 1.2 (approximately), t_f/T appears to go to infinity. This implies that no bedform propagation occurs for values of ψ/ψ_c that are less than 1.2.

In summary, while the developing bed data is widely scattered, some preliminary conclusions can be stated. First, the Representative Shields Parameter provides a reasonably good indicator of wave sediment interaction for a developing bed. Secondly, the use of a representative monochromatic wave to represent a wave spectrum provides an acceptable characterization of the response of a developing bed. Because of the wide scatter in the data, and unavoidable subjectivity in observations and estimates, no relationships are presented to characterize the developing bed at this time. Accurate relationships for the developing bed would require additional research.

5.3 The Fully Developed Bed

5.3.1 Monochromatic Waves

5.3.1.1 Comparison with Existing Relationships

For a reasonably high wave intensity, once we have bedform propagation occurring at the irregularities described in Section 5.1, we expect the associated ripple patches to continue to grow until the bed is completely covered. With a continued steady-state wave motion over the sand bed, the ripples should eventually reach a steady state in which their characteristics are statistically independent of time. For this condition, we refer to the bed as fully developed.

Some common parameters used to characterize fully developed bedform geometry include the bedform height (η), length (λ), steepness (η/λ). In addition, the asymmetry (α) is also occasionally considered. If we define our bedform as being bounded by two troughs, we can define the asymmetry as the ratio of the length between the first trough and the crest of a ripple, to that of this trough to the next trough (the ripple length). Normally the height and length are nondimensionalized by the excursion amplitude, A_b. The nondimensionalized height and steepness have been considered to be the important parameters defining the relative roughness, and therefore are of special interest.

Many previous experiments have shown that the bedform parameters (and attenuation results) will exhibit different behavior for values of ψ'/ψ_c exceeding a particular value, commonly denoted as the "breakoff value". Above this value, in the breakoff range, the ripples were observed to be somewhat shaved off and exhibited a three-dimensional nature. In addition, this breakoff range was estimated in terms of the sediment characteristics as was defined in Equation 2.17.

Stefanick (1979) presented some empirical relationships to relate the fully developed bedform characteristics to the intensity of the waves passing over the sand bed. These relationships, which are discussed in Chapter 2, accounted for the existence of a breakoff range and relate the bedform geometry to Shields Parameter, a dimensionless parameter that has successfully been shown to represent wave-sediment interaction. Since we are interested in verifying the use of this parameter for any sand, the bedform geometry data from both the .12-mm and .20-mm sand experiments were plotted against it.

The random nature associated with the breakoff range appeared to be prevalent for a number of the high intensity monochromatic wave experiments completed in this study. The attenuation results (discussed in the next chapter) also exhibited some type of breakoff. Therefore, one would expect that the parameters defining bedform characteristics would exhibit this breakoff and that the empirical relationships defined in Stefanick's thesis would be appropriate. However, upon plotting the bedform parameters against ψ'/ψ_c, no concrete evidence of the breakoff was found.

For example, Figure 5.4 shows η/A_b plotted against ψ'/ψ_c. For the .12-mm sand, the application of Equations 2.15 through 2.19 provides a reasonable fit to the data. However, for the .20-mm sand, the breakoff point is estimated to be at a higher wave intensity and these equations provide a poor fit to the data. In addition, the data points for the .20-mm sand and .12-mm sand basically fall on a single straight line. Therefore, at this point, the linear curve fit proposed by M. Rosengaus (1987) appears to provide the most accurate representation of the data and the breakoff characteristics defined by Equations 2.15 through 2.19 cannot be substantiated. However, the use of ψ'/ψ_c as a dimensionless parameter representing wave-sediment interaction appears to be verified.
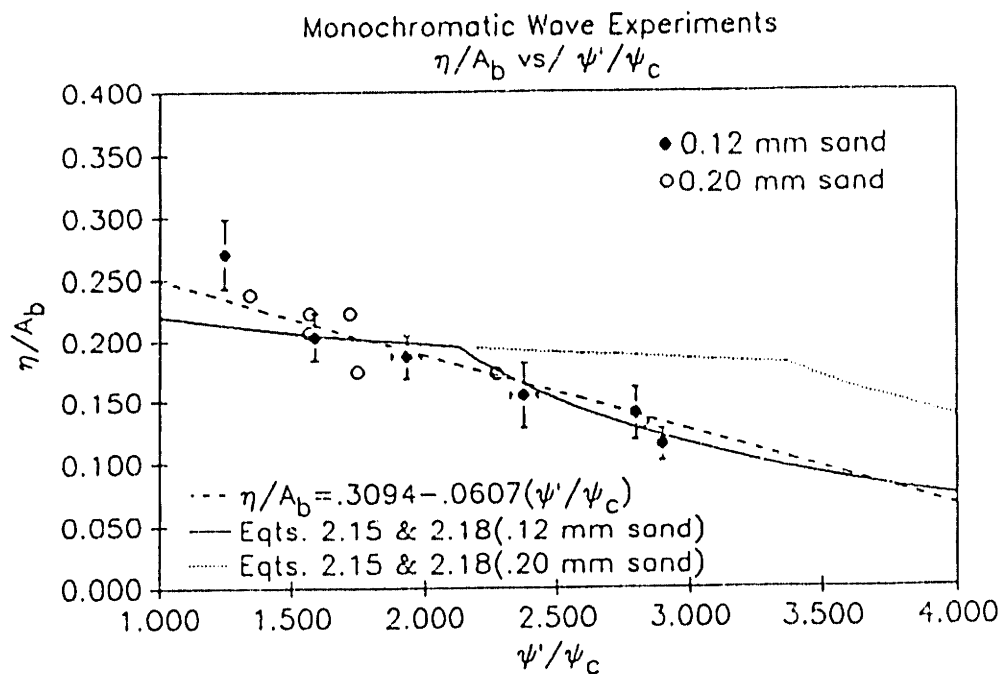
Figure 5.4   Fully developed bedform height for monochromatic waves – Comparison with existing relationships
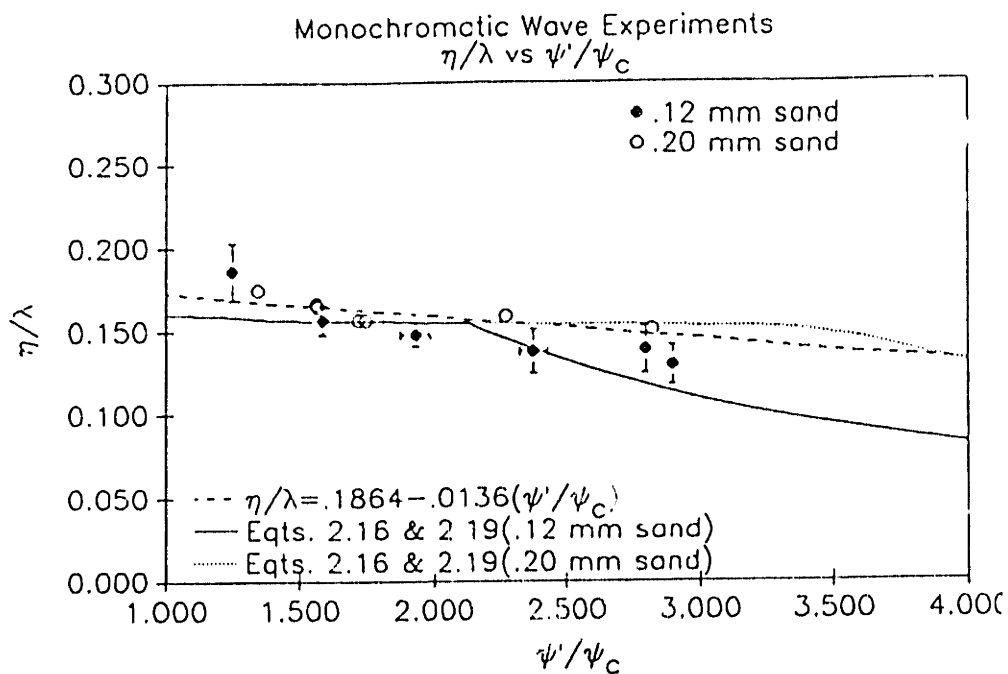

Figure 5.5   Fully developed bedform steepness for monochromatic waves – Comparison with existing relationships

This argument seems to be verified even more in light of the results presented in Figure 5.5, in which η/λ is plotted against ψ'/ψ_c. In this case, we do see a slight difference between the .20-mm sand and .12-mm sand as we move out into the breakoff range. However, the difference is not significant enough to justify a distinction. Moreover, the plot of Equation 2.19 in the breakoff range for the .12-mm sand shows a poor correlation with this data.

The final two plots are those of λ/A_b vs. ψ'/ψ_c and α vs ψ'/ψ_c, shown in Figures 5.6 and 5.7, respectively. While neither of these two parameters are normally used in the calculation of the relative roughness, λ/A_b is obviously associated with η/λ and η/A_b. Therefore, one can simply consider λ/A_b to be the ratio of η/A_b to η/λ. In any event, both curves basically show the data points for the two different sands to lie on a single line and no distinct breakoff point can be confirmed.

5.3.1.2 Proposed Relationships

As stated above, the concept of a breakoff range for the bedform geometry parameters cannot be confirmed with existing data. Therefore, two alternatives have been considered. For the first approach, we can characterize the bedform geometry in terms of linear curve fits as was originally done by M. Rosengaus. In the second approach, we can look more closely at the relationships proposed in Stefanick(1979) to verify the appropriate definition of the breakoff value and associated equations.

5.3.1.2.1 Linear Curve Fits

In this case, the curve fits proposed in Rosengaus (1987) have been modified, since more data have now been included.
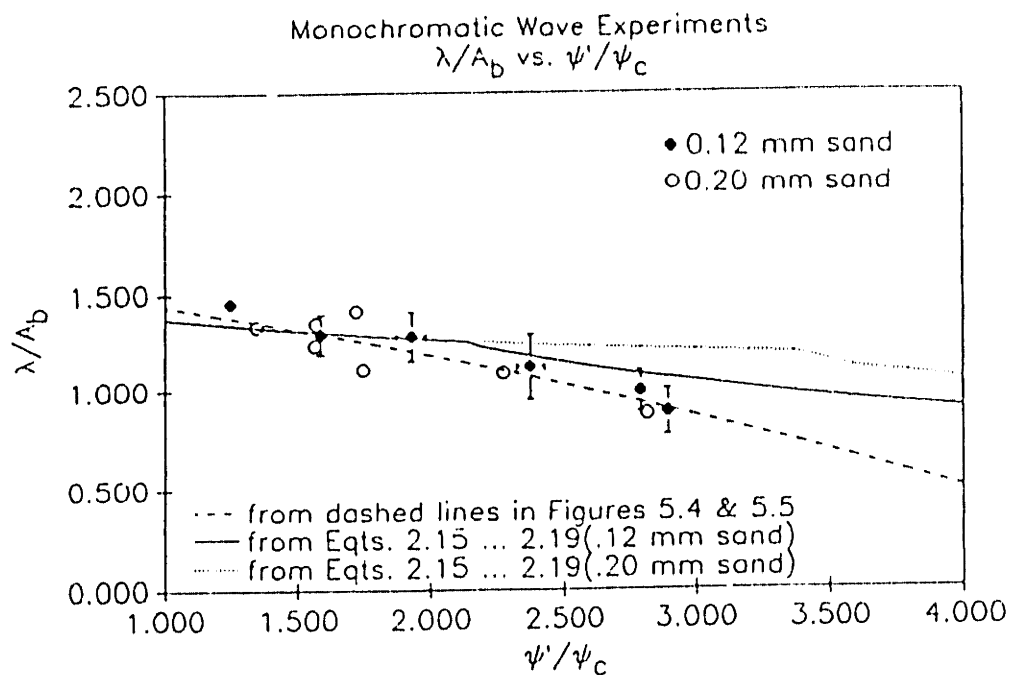
Therefore, we obtain

Figure 5.6   Fully developed bedform length for monochromatic waves – Comparison with existing relationships
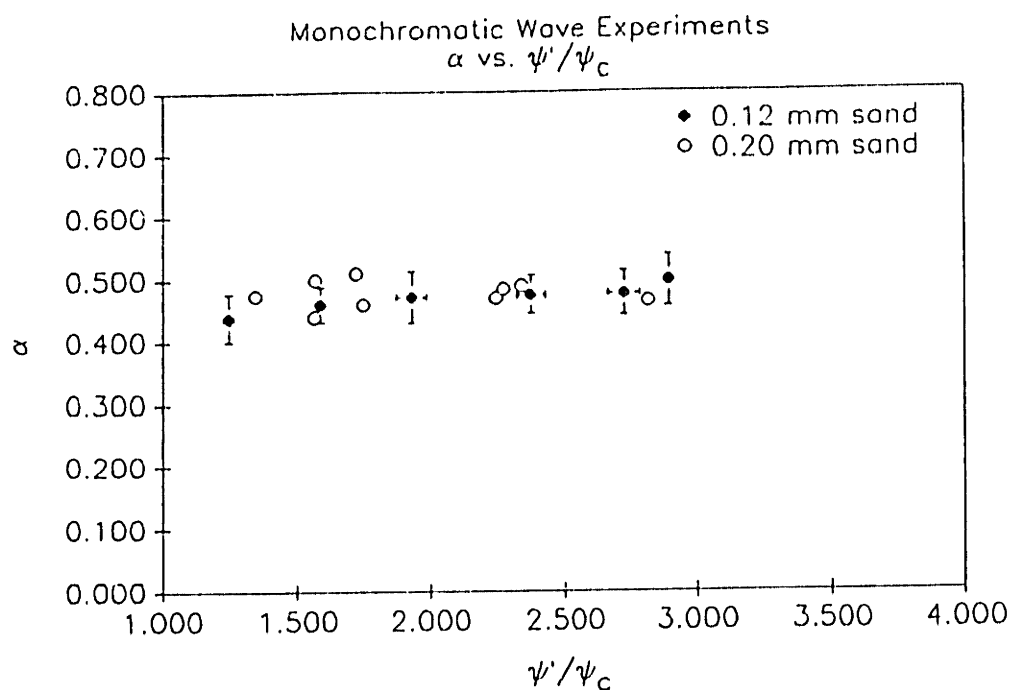

Figure 5.7   Fully developed bedform asymmetry for monochromatic waves

$$\eta/A_b = .3365 - .0751(\psi'/\psi_c) \qquad (5.1)$$

Also,

$$\eta/\lambda = .1904 - .0176(\psi'/\psi_c) \qquad (5.2)$$

Combining these two yields

$$\lambda/A_b = 1.5977 - .1878(\psi'/\psi_c) \qquad (5.3)$$

Finally,

$$\alpha = .4482 + .0129(\psi'/\psi_c) \qquad (5.4)$$

These relationships are plotted in Figures 5.8 through 5.11 along with the data they represent. All of these relationships are very similar to those defined in Rosengaus (1987), which are shown by the dashed lines in Figures 5.8 through 5.11.

5.3.1.2.2 Improvements Based on Updated Breakoff Range

To verify the breakoff values defined by Stefanick, the data summarized in Figures 5.12A and 5.12B (taken from Stefanick,1979) were analysed. In these plots, $(\psi'/\psi_c)_b$ is plotted as a function of S_*. In Figure 5.12A, the experimental breakoff values (or ranges) were defined using ripple steepness data, and Stefanick's breakoff relationship, Equation 2.17, is shown as a dashed line. In Figure 5.12B, this dashed line is also shown and the ranges were defined using ripple height data. Rather than the "visual best fit" obtained by Stefanick, a power law relationship for the data shown in Figures
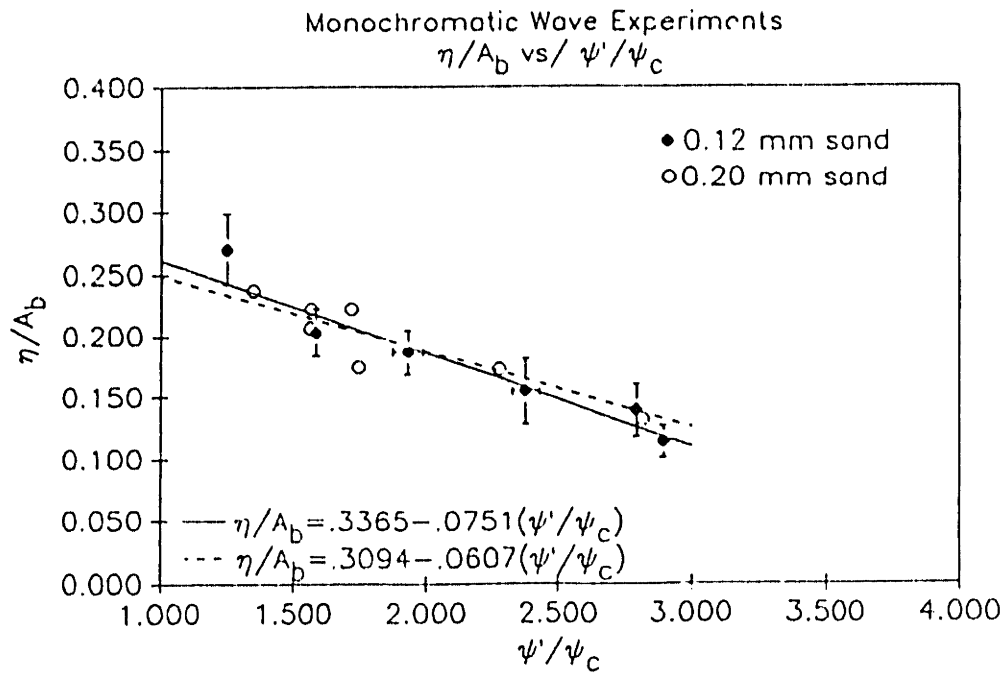
Monochromatic Wave Experiments
η/A_b vs/ ψ'/ψ_c

- 0.12 mm sond
- ○ 0.20 mm sond

$\eta/A_b = .3365 - .0751(\psi'/\psi_c)$

$\eta/A_b = .3094 - .0607(\psi'/\psi_c)$

Figure 5.8   Fully developed bedform height for monochromatic waves – Proposed relationship

Monochromatic Wave Experiments
η/λ vs ψ'/ψ_c

- .12 mm sond
- ○ .20 mm sond

$\eta/\lambda = .1904 - .0176(\psi'/\psi_c)$

$\eta/\lambda = .1864 - .0136(\psi'/\psi_c)$
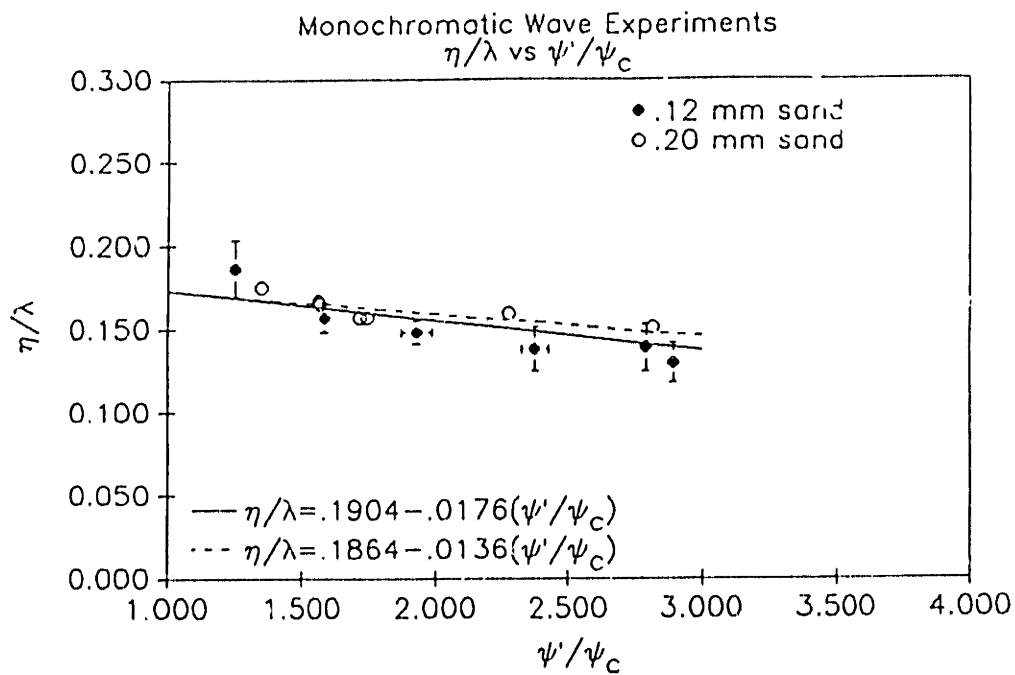
Figure 5.9   Fully developed bedform steepness for monochromatic waves – Proposed relationship
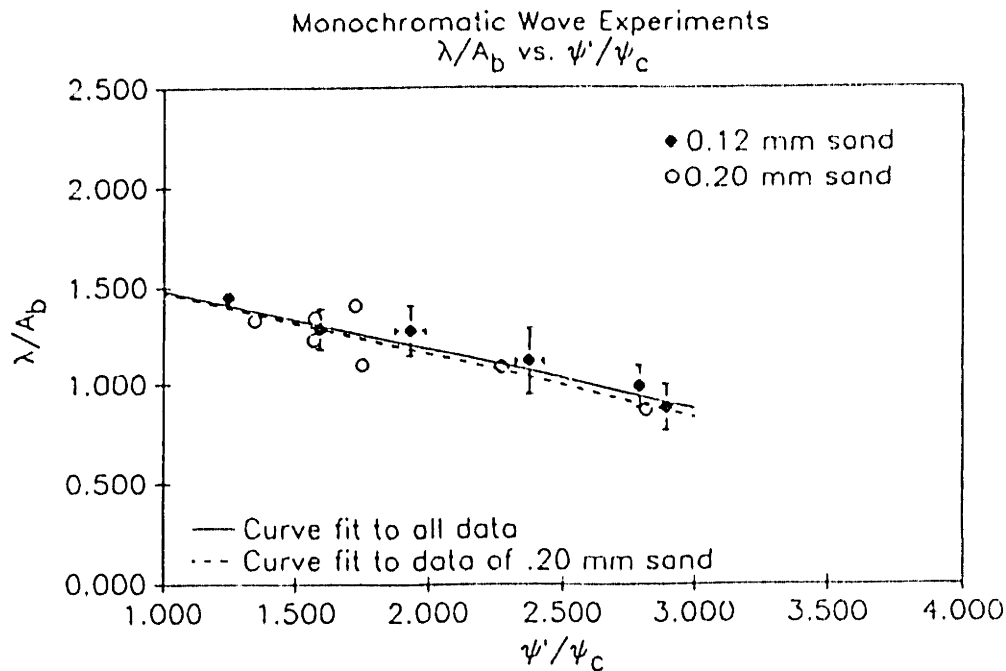
Figure 5.10   Fully developed bedform length for monochromatic waves - Proposed relationship
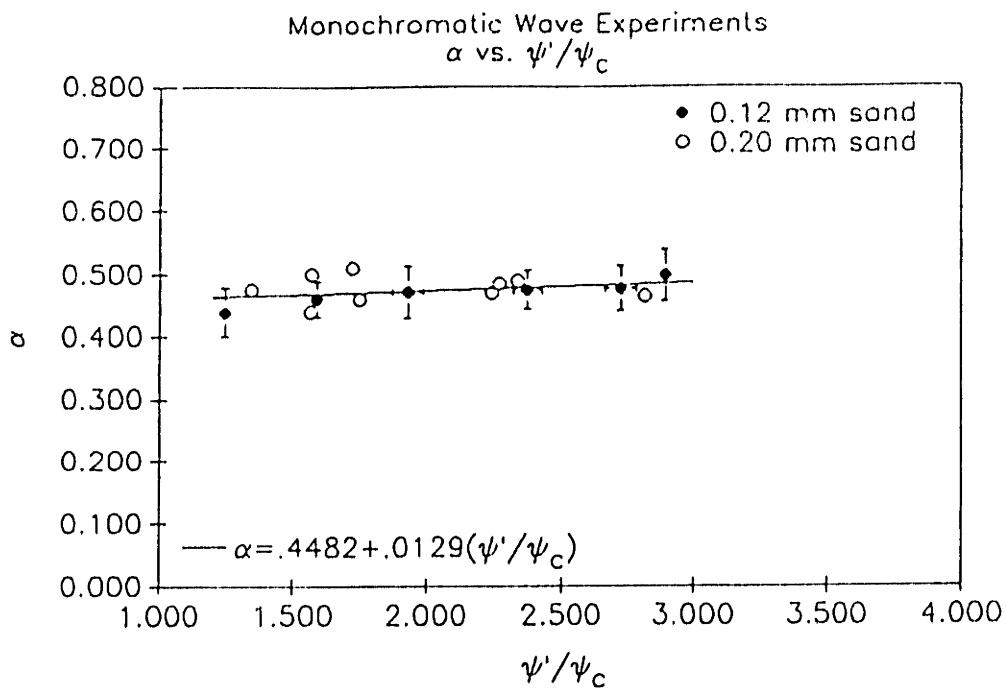

Figure 5.11   Fully developed bedform asymmetry for monochromatic waves - Proposed relationship
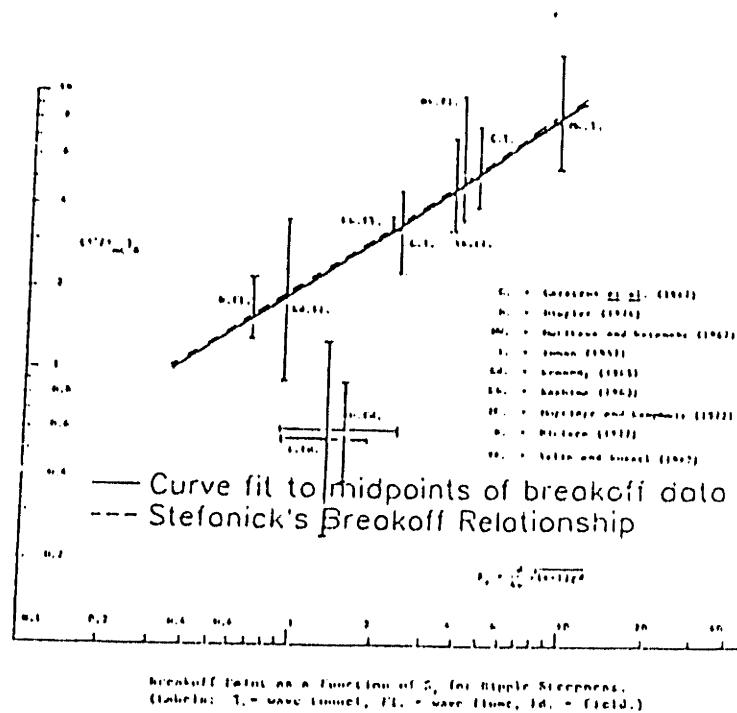
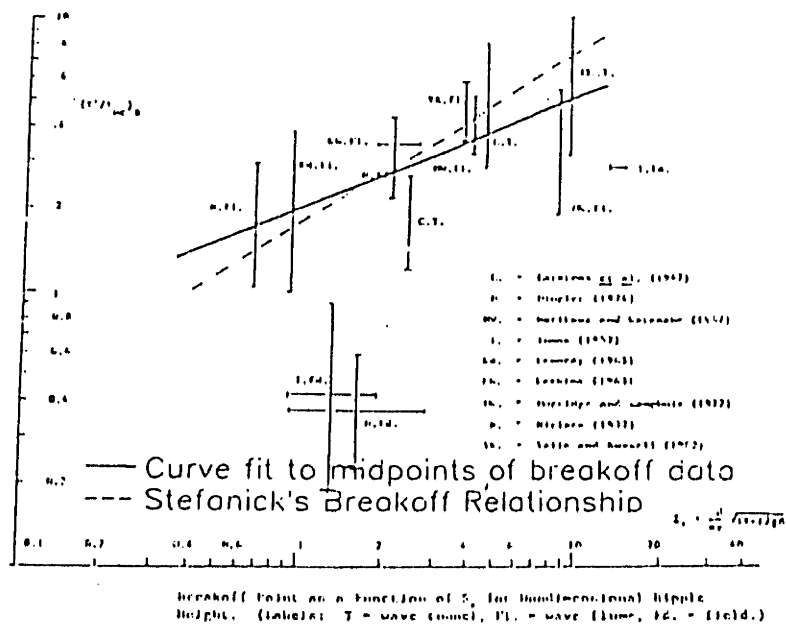Figure 5.12A   Curve fit to ripple steepness breakoff data taken from Stefanick (1979)

Figure 5.12B   Curve fit to nondimensional ripple height breakoff data taken from Stefanick (1979)

5.12A and 5.12B was assumed and best-fit lines were located by making use of the midpoints of all of the data ranges plotted. These more rationally determined relationships are plotted on the figures as the solid lines. In this case, the breakoff value using the ripple steepness data was found to be described by:

$$(\psi'/\psi_c)_{bnl} = 1.8 \, S_*{}^{.6} \tag{5.5}$$

which is the same as that defined by Stefanick. However, the breakoff using the nondimensional ripple height data was found to be:

$$(\psi'/\psi_c)_{bnab} = 2.0 \, S_*{}^{.4} \tag{5.6}$$

which is different from Stefanick's relationship.

While Stefanick had assumed a single value representing the breakoff point for all ripple geometry parameters, this analysis would imply that different bedform geometry parameters might exhibit a breakoff at different values of ψ'/ψ_c. In addition, a physical argument can be presented to justify the possibility of these separate breakoff values. This argument stems from the observation that ripples associated with the higher values of ψ'/ψ_c appear to be shaved off. As we increase the wave intensity to a point at which the tops of the ripples are being shaved off, the slope of the η/A_b curve would get steeper. If the ripple length does not change significantly at this point, then λ/A_b would continue to vary at the same slope. In this case, η/λ would exhibit a breakoff at this point. On the other hand, if the ripple length changes in such a way that the ripple shape is roughly maintained, η/λ may not yet exhibit a breakoff. In this case, a breakoff in ripple steepness, η/λ, might still occur at a higher wave intensity. In

any event, the assumption of a single breakoff value for all bedform parameters is not necessarily the case, and different breakoff values are quite possible.

As noted above, Stefanick's expression for $(\psi'/\psi_c)_b$ matched the curve fit to the η/λ breakoff, and therefore is still considered to be valid for that parameter. Consequently, Stefanick's relationships for η/λ were considered to be valid both below and above the breakoff point. However, the expression obtained for $(\psi'/\psi_c)_b$ using the curve fit to the η/A_b breakoff data was different from that of Stefanick. Therefore, while the same η/A_b expression could be used below the breakoff point, modification of the η/A_b equation above the breakoff point was considered to be preferable.

To accomplish this, the power of ψ'/ψ_c in the η/A_b equation was taken to be the same as that defined by Stefanick, -1.5, leaving two unknowns: an exponent for S_* and a constant coefficient. Then, revised values for these two unknowns could be defined by using the following "power law" form of an equation for η/A_b:

$$\eta/A_b = A \; S_*{}^B \; (\psi'/\psi_c)^{-1.5}$$

along with Equation 5.6. The resulting relationship is:

$$\eta/A_b = .56 \; S_*{}^{.54} \; (\psi'/\psi_c)^{-1.5} \tag{5.7}$$

Now, these revisions may be applied to the .12- and .20-mm sand that was used in the present experiments. First, from Equation 5.5, the breakoff for η/λ, $(\psi'/\psi_c)_{bnl}$, is at a ψ'/ψ_c of 2.128 for the .12-mm sand, and 3.371 for the .20-mm sand. Using Equation 5.6, for η/A_b, $(\psi'/\psi_c)_{bnab}$ can be shown to be 2.236 and 3.038 for the .12- and .20-mm sands, respectively. In addition, the η/A_b plot (Figure 5.4) has been modified using Equations 2.15 and 5.7. The revised plot is shown in Figure 5.13. For
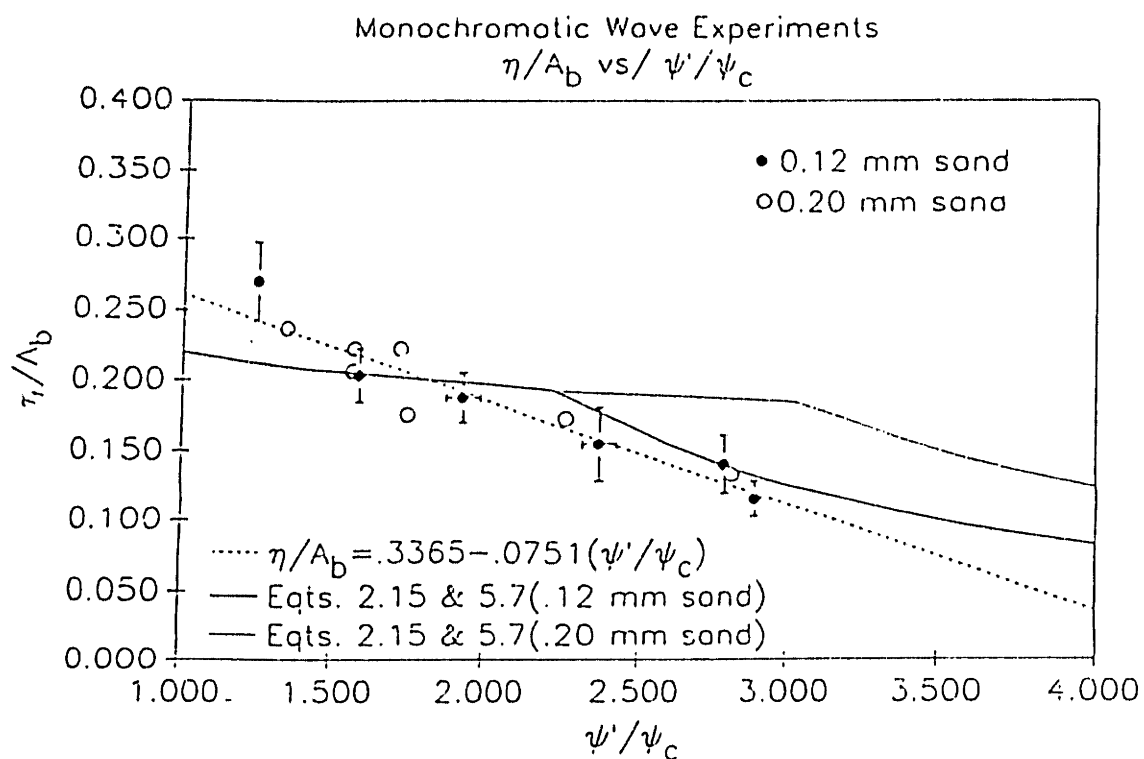
Figure 5.13   Revised plot of fully developed bedform height for monochromatic waves, based on updated breakoff range

values of ψ'/ψ_c that are below any breakoff, there is no change from Figure 5.4. However, the locations of the curves in the breakoff range have changed to reflect the modified breakoff range noted above. Here, the curve for the .12-mm sand still closely matches the data and the curve for the .20-mm sand is shifted back somewhat. Unfortunately, however, this shifted .20-mm curve is still significantly higher than the data point located at a ψ'/ψ_c of about 2.8.

To summarize, this alternative approach does not represent the data as accurately as the use of the linear curve fit discussed in the preceeding section. However, it does improve upon Stefanick's relationship somewhat. In addition, this approach accounts for the concept of a breakoff range. As will be discussed in Chapter 6, the presence of some type of breakoff range makes physical sense and also is justified by experimental data for attenuation of monochromatic waves. Again, the η/A_b can be described using Equation 2.15 if ψ'/ψ_c is below the appropriate breakoff, which is defined by Equation 5.6, and by Equation 5.7, if ψ'/ψ_c is above this breakoff. For η/λ, Equation 2.16 is used below the breakoff, defined using Equation 5.5 (or 2.17, since they are the same), and by Equation 2.19 above the breakoff value.

5.3.2 Spectral Waves

5.3.2.1 Comparison with Existing Relationships

For the Wave Spectra, we would hope that we could define a representative Shields Parameter to characterize the wave-sediment interaction. In addition, we would like to describe the wave spectrum in terms of a monochromatic wave as discussed in Chapter 2. Therefore, the representative horizontal bottom excursion amplitude for the spectrum, A_{brep}, is used to normalize the bedform parameters. Hopefully, the attenuation and bedform characteristics for wave spectra, when represented in this

fashion, can be shown to comply with the relationships for monochromatic waves. If this is the case, then the task of determining wave spectrum attenuation and associated bedform response would be simplified tremendously due to the equations that already exist for the monochromatic waves.

In this study, the use of the equivalent monochromatic wave, defined in Chapter 2, as a representation for spectral attenuation and bedform characteristics could not be verified. However, the representative Shields parameter proved to be an adequate parameter describing wave–sediment interaction for a wave spectrum.

This is apparent in Figure 5.14, which shows of plot of the nondimensionalized bedform height against the representative Shields parameter. In this case, there is a relatively good correlation between the data of the monochromatic wave experiments and spectral wave experiments, although the spectral data does lie slightly below the monochromatic data. In addition, the spectral data for both the .12-mm sand and .20-mm sand correlate quite well, showing that $(\psi'/\psi_c)_{rep}$ is a physically relevant parameter representing wave/sediment interaction.

When the ripple steepness, η/λ, is plotted against ψ'/ψ_c, the spectral data do not correlate very well with the monochromatic wave data, as can be seen in Figure 5.15. Here, the ripples formed by monochromatic waves appear to be steeper than those formed by spectral waves. It appears as though the many components associated with the wave spectrum giving rise to occasionally high near-bottom velocities must somehow limit the growth or the geometry of the bedforms.

The final plots of interest include those parameters that are not commonly considered to be directly related to the relative roughness, which is discussed in Chapter 6. These parameters are λ/A_{brep} and α and are shown in Figures 5.16 and 5.17. A relatively good correspondence between the data of the monochromatic wave
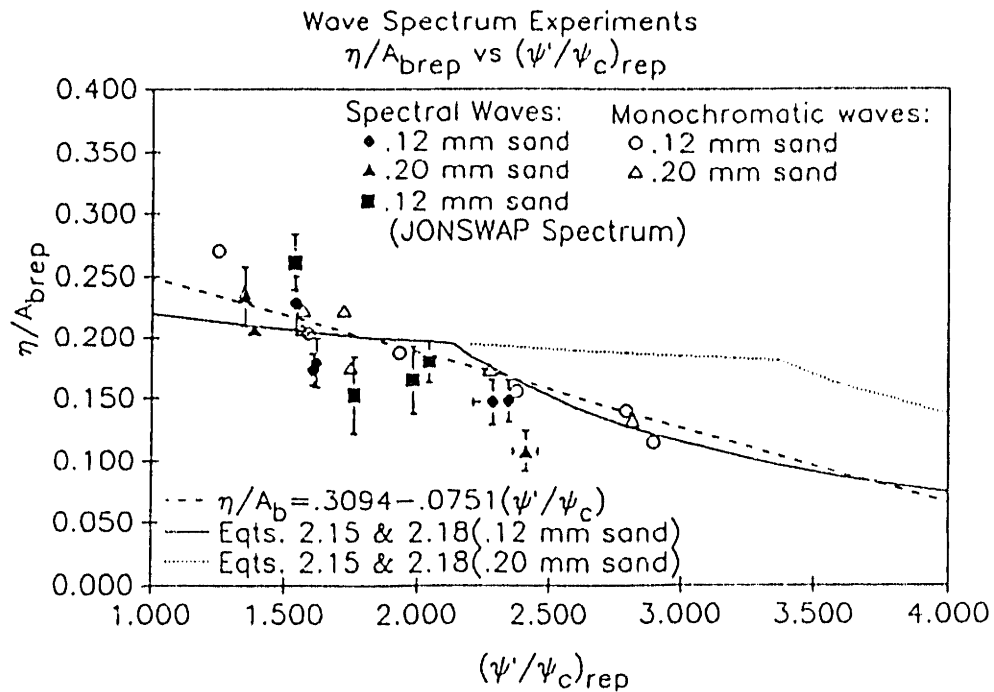
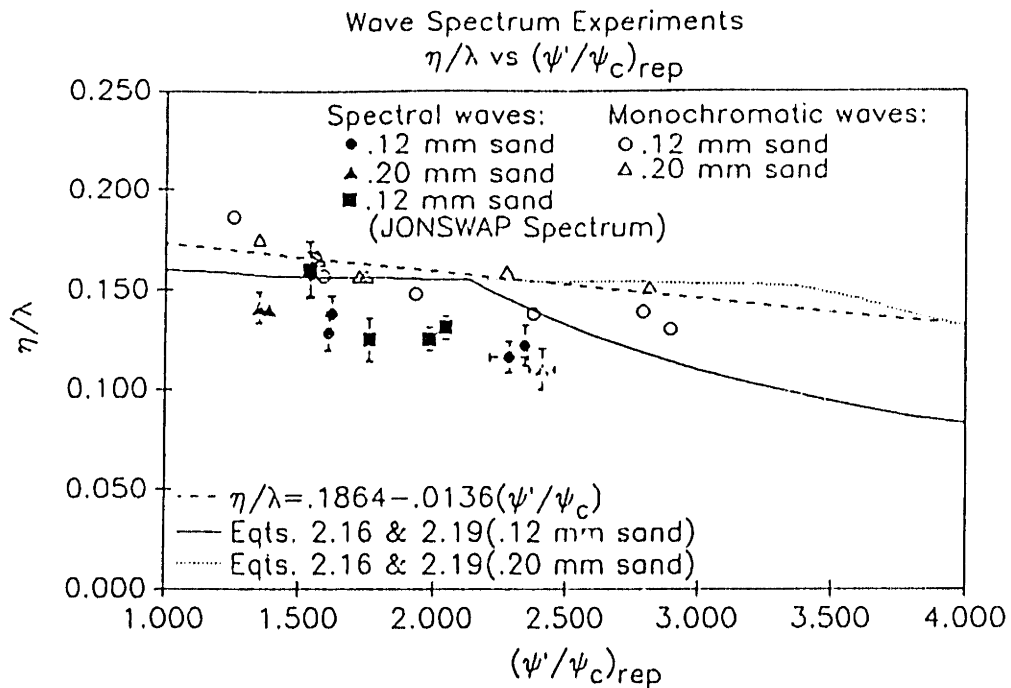Figure 5.14   Fully developed bedform height for spectral waves - Comparison with existing relationships

Figure 5.15   Fully developed bedform steepness for spectral waves - Comparison with existing relationships
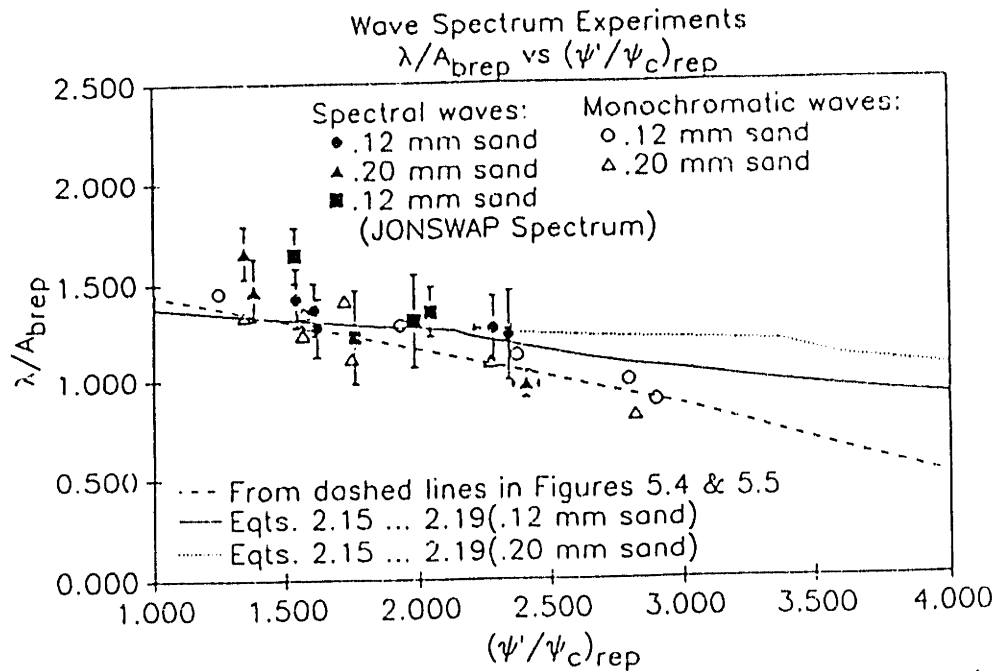
Wave Spectrum Experiments
λ/A_{brep} vs $(\psi'/\psi_c)_{rep}$

Figure 5.16   Fully developed bedform length for spectral waves – Comparison with existing relationships

Wave Spectrum Experiments
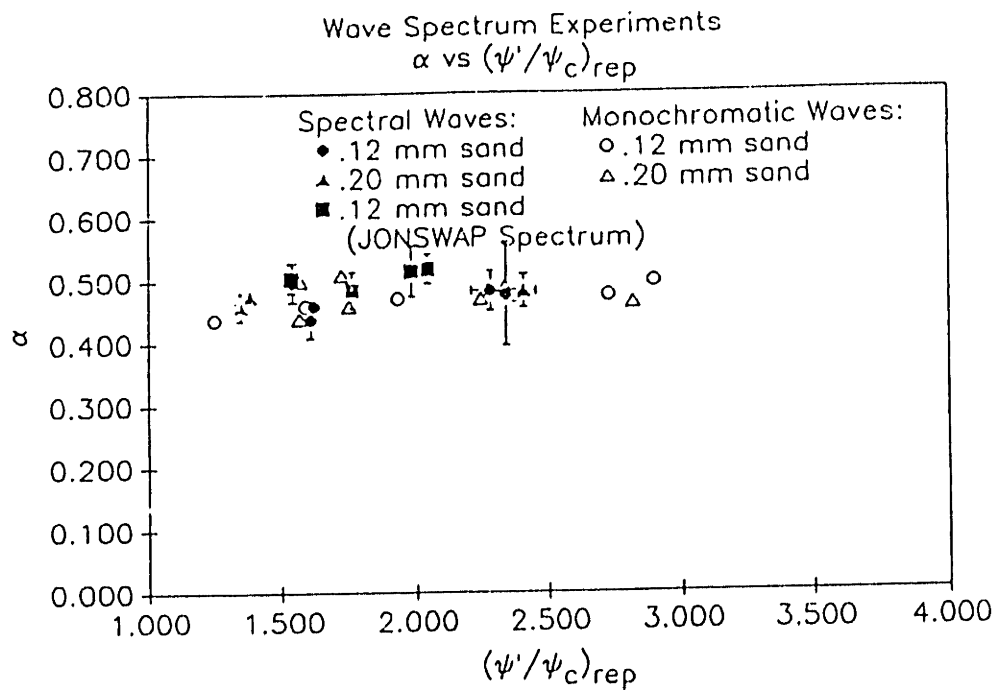### α vs $(\psi'/\psi_c)_{rep}$

Figure 5.17   Fully developed bedform asymmetry for spectral waves

experiments and those of the spectral experiments can be noticed in both of these plots. In Figure 5.16, however, it can be seen that λ/A_b for the spectral experiments is slightly higher than λ/A_b for the monochromatic experiments. This is reasonable when we realize that λ/A_{brep} is indirectly related to the roughness because λ and A_{brep} respectively show up in η/λ and η/A_{brep}.

In summary, $(\psi'/\psi_c)_{rep}$ is applicable to the bedform parameters for both the monochromatic and spectral waves. The bedform parameters for the spectral experiments using the different types of sand correlated quite well, as did those for the monochromatic wave experiments. However, a direct correlation between the monochromatic wave results and spectral wave results was not observed primarily due to the differences in ripple steepness. Of course, any differences in this steepness should show up in both the η/A_b parameters and λ/A_b parameters, since they have common variables. Careful review of Figures 5.14 and 5.16 does show that, for λ/A_b, the spectral results are slightly higher, and for η/A_b, the monochromatic results are slightly higher. Therefore, it appears as though the difference in steepness may be attributed to a slightly lower bedform height and slightly longer bedform length for the wave spectrum experiments.

5.3.2.2 Proposed Relationships

As discussed above, it appears as though previously defined relationships for monochromatic waves cannot justifiably be applied to the bedform characteristics for a wave spectrum. Therefore, the proposed relationships will simply consist of linear line fits though the .12-mm and .20-mm spectral data. First, for the parameters that are commonly considered to be related to the relative roughness, we obtain:

$$\eta/A_{brep} = .3357 - .0869(\psi'/\psi_{crep}) \tag{5.8}$$

and

$$\eta/\lambda = .1864 - .0136(\psi'/\psi_{\mathrm{crep}}) \tag{5.9}$$

Here, we see that the equation for η/A_{brep} is quite similar to Equation 5.1, but η/λ is somewhat different than Equation 5.2. For $\lambda/A_{\mathrm{brep}}$, we find that:

$$\lambda/A_{\mathrm{brep}} = 2.0490 - .3859(\psi'/\psi_{\mathrm{crep}}) \tag{5.10}$$

which is quite similar to Equation 5.3. Finally, the equation for α is simply taken to be that same as Equation 5.4, which was derived for the monochromatic wave experiments

$$\alpha = .4482 + .0129(\psi'/\psi_{\mathrm{crep}}) \tag{5.11}$$

These four relationships are plotted against the data they represent in Figures 5.18 through 5.21.
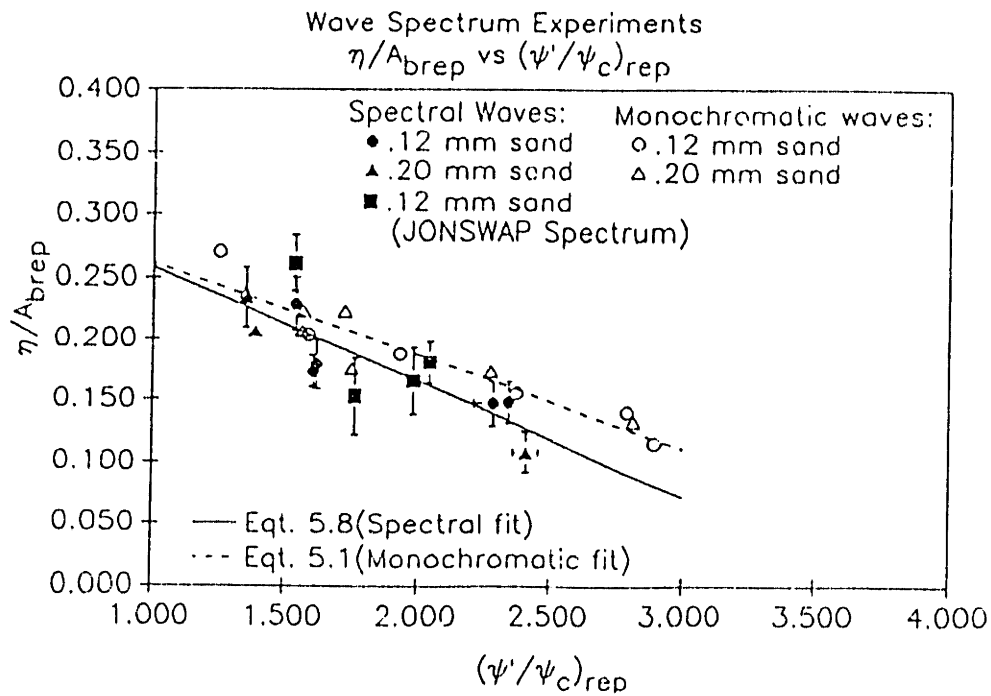
Figure 5.18 Fully developed bedform height for spectral waves – Proposed relationship
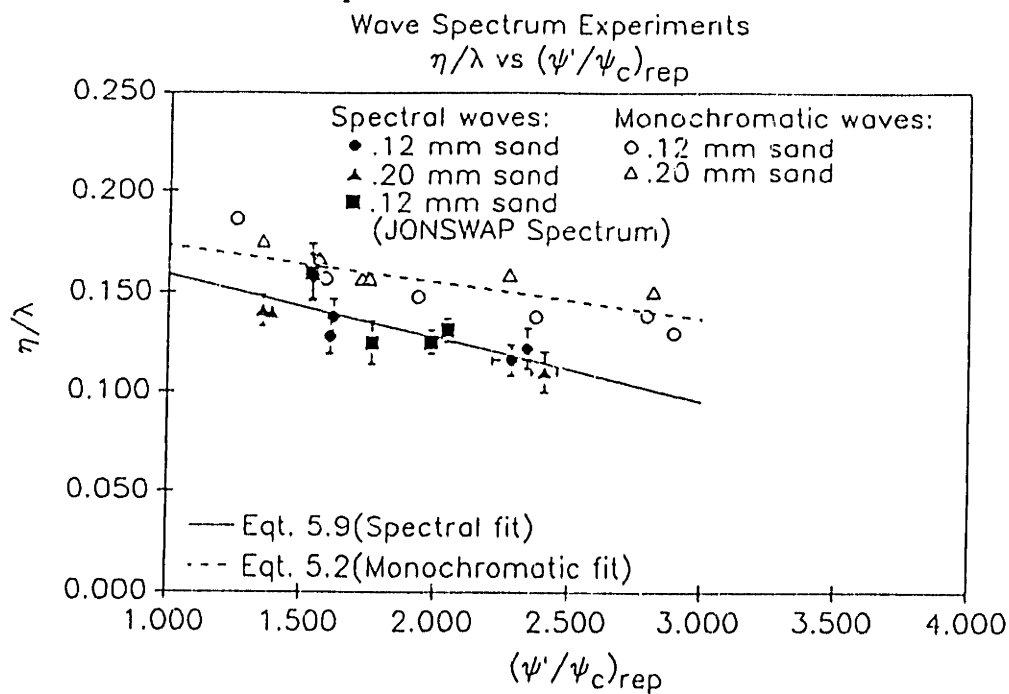

Figure 5.19 Fully developed bedform steepness for spectral waves – Proposed relationship
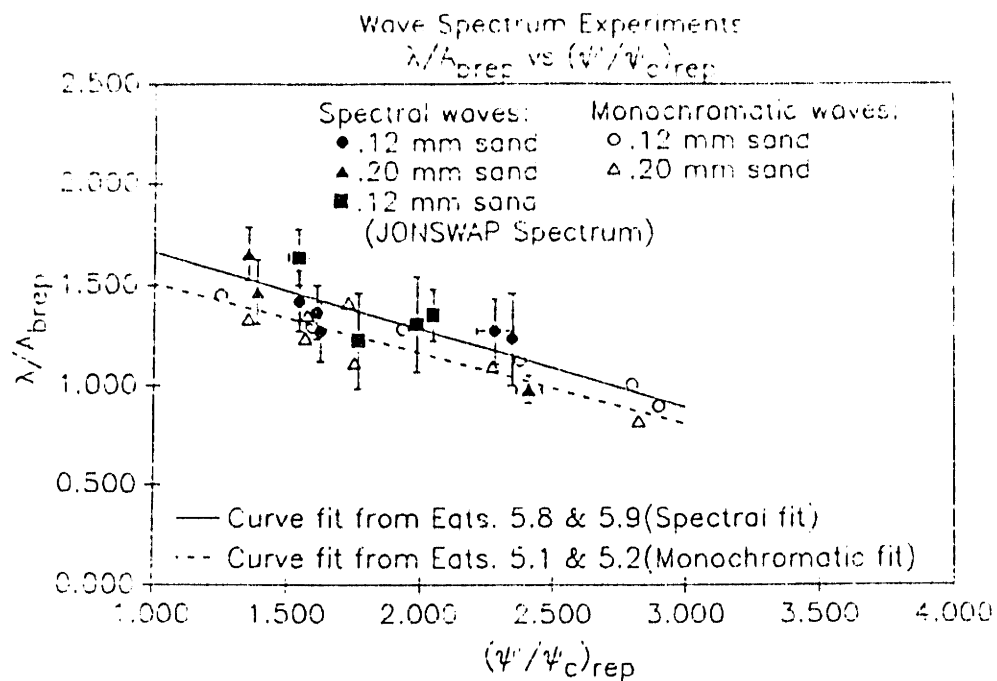
Figure 5.20   Fully developed bedform length for spectral waves – Proposed
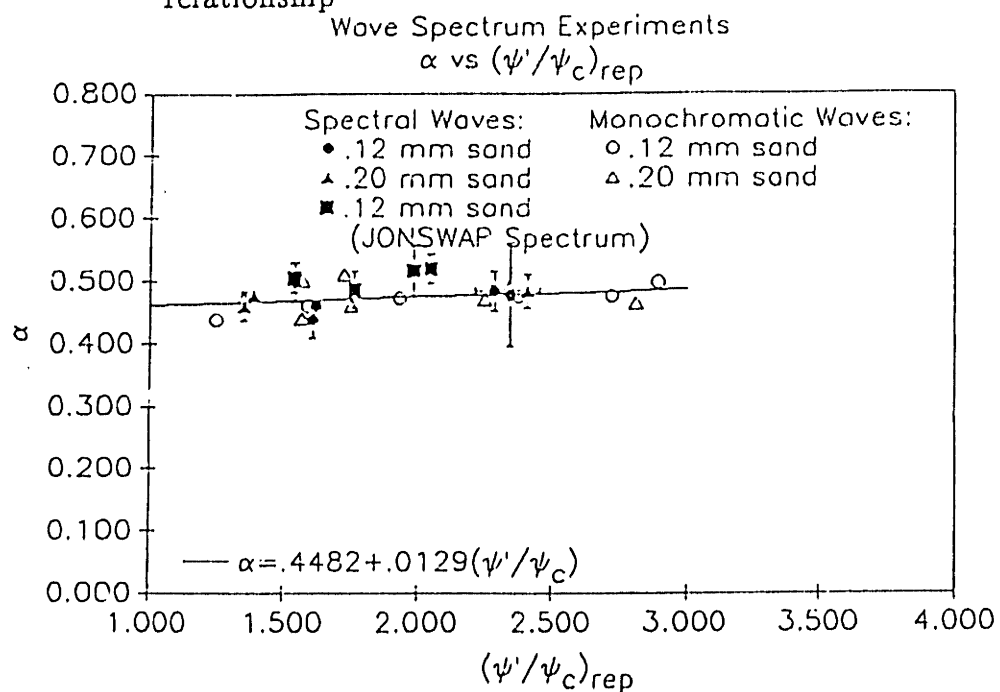relationship

Figure 5.21   Fully developed bedform asymmetry for spectral waves – Proposed
relationship

6 WAVE ATTENUATION OVER A FULLY DEVELOPED BED

6.1 Monochromatic Waves

6.1.1 Comparison with Existing Relationships

As discussed in Chapter 5, when waves pass over a sand bed, bedforms will develop. These bedforms will act as roughness elements which will increase friction over the bed and result in wave attenuation. If we are interested in the wave height or wave energy (possibly for engineering purposes) for a wave train that has passed over a sand bed, this attenuation could be of significant importance. Therefore, the relationships between bedform characteristics, relative roughness, and wave attenuation are desirable.

The experiments completed to study wave attenuation over the sand bed made use of the theory and procedures detailed in Rosengaus (1987). In summary, the procedure is to measure the attenuation and use it to calculate the friction factor. Then, we can use existing relationships between friction factor, f_w, and relative roughness, k_b/A_b, and measurements of bedform geometry to piece together the relationships of interest. Some attenuation results of the experiments completed are summarized in Table 6.1.

As can be seen in that table, no attenuation analysis was completed in Experiment A, which was completed to investigate the initiation of motion for the .12-mm sand. However, attenuation was analyzed in Experiment B and friction factor information for that experiment is included in Table 6.1.

The monochromatic wave attenuation results for Experiment B are summarized in Figure 6.1, which shows the friction factor, f_w, plotted against the Relative Shields parameter, ψ'/ψ_c, for both the .12-mm sand and .20-mm sand. In this figure, three

Table 6.1

Monochromatic FDB Experimental Results

Results of Monochromatic Wave Experiments

Expt ID	Run #	Amplitude at x=0 (cm)	Ursell #	Near bottom Excursion Amplitude (cm)	Near bottom Orbital Velocity (cm/sec)	Near Bottom Reynolds #	Relative Shield's Parameter	Friction Factor	
								Avg.	St.Dev.
A	1	1.58	5.28	2.36	5.65	1333	0.568		
	2	1.99	6.64	2.97	7.10	2110	0.714		
	3	2.39	7.98	3.57	8.54	3049	0.881		
	4	2.72	9.07	4.06	9.71	3939	0.973		
	5	3.14	10.47	4.68	11.20	5245	1.129		
B	1	3.09	10.30	4.61	11.02	5078	1.248	0.193	0.010
	2	4.32	14.40	6.44	15.41	9930	1.589	0.190	0.017
	3	5.36	17.88	8.00	19.13	15306	2.376	0.107	0.008
	4	5.29	20.97	9.39	22.45	21067	2.796	0.094	0.012
	5	6.91	23.02	10.30	24.64	25376	2.898	0.084	0.008
	6	4.72	15.72	7.16	17.12	12252	1.933	0.178	0.008

Monochromatic Wave Experiments
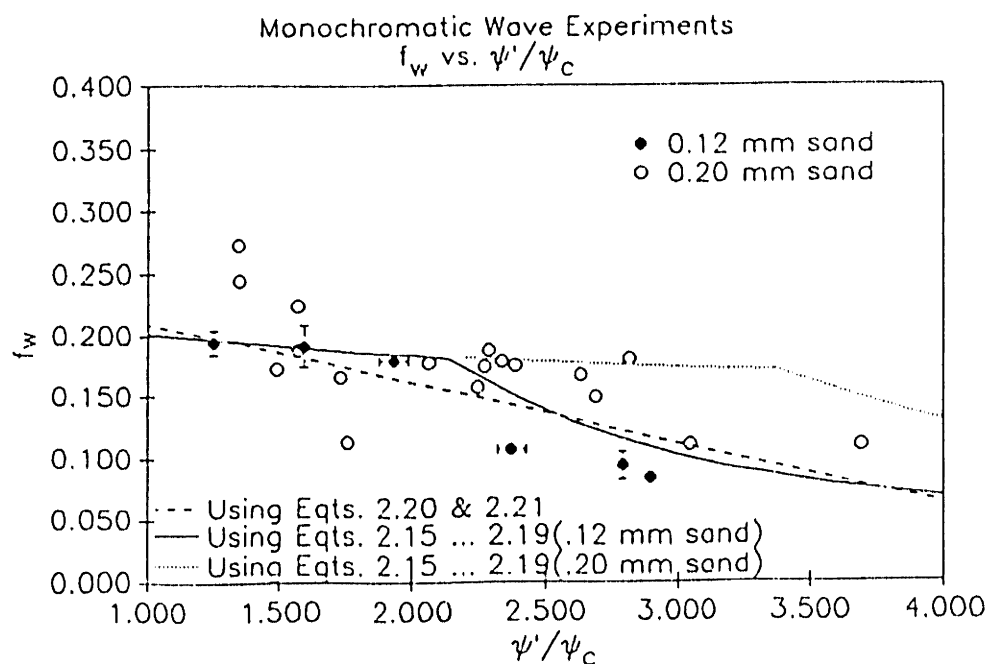f_w vs. ψ'/ψ_c

Figure 6.1   FDB friction factor for monochromatic waves - Comparison with curves based on Stefanick's relationships and linear fits to bedform data (Models 1 and 2)
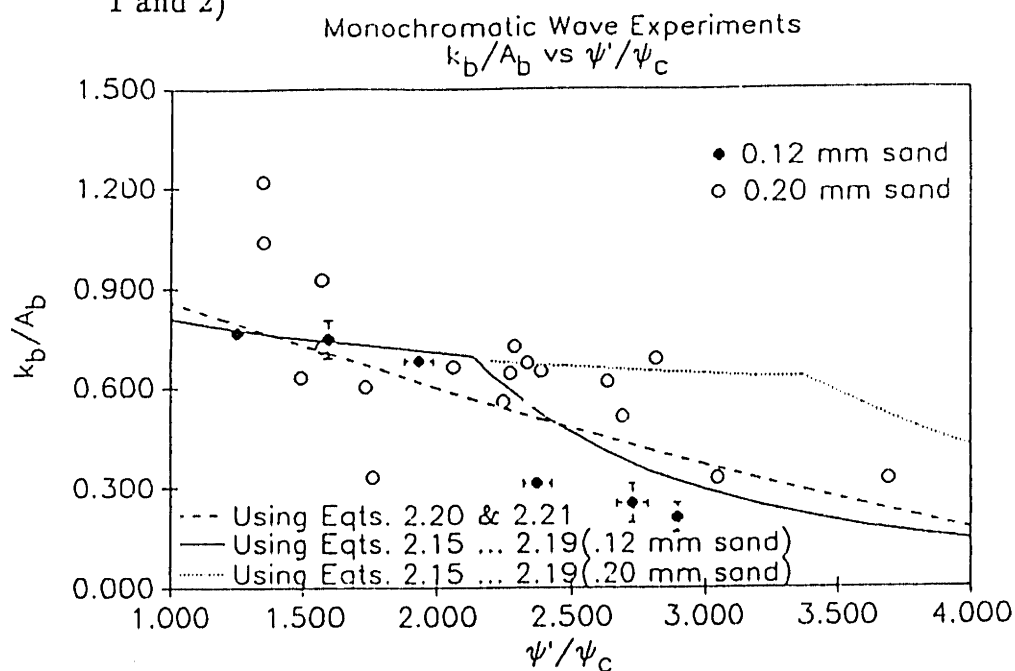
Monochromatic Wave Experiments
k_b/A_b vs ψ'/ψ_c

Figure 6.2   FDB relative roughness for monochromatic waves · Comparison with curves based on Stefanick's relationships and linear fits to bedform data (Models 1 and 2)

curves are plotted—all of which make use of Equation 2.25, the Grant-Madsen relationship between friction factor and relative roughness.

The solid and dotted lines make use of a modified form of Equation 2.22, Grant and Madsen's equation relating bedform geometry to the relative roughness:

$$k_b/A_b = 23(\eta/A_b)(\eta/\lambda)$$
(6.1)

In this form of the equation, the effects of sediment transport have been neglected because of the relatively low flow intensity. Also, the constant, 23, is used instead of the origional constant, 28. This revised constant was proposed by M. Rosengaus based on results of the experiments completed using the .20-mm sand. As can be seen in Figure 6.1, for values of ψ'/ψ_c that are less than about 2.2, the curve based on the relationship above provides an excellent fit to the data for the .12-mm sand. Therefore, the use of this revised constant was considered to be verified in the .12-mm sand experiments.

The geometry parameters in Equation 6.1 were obtained using Stefanick's empirical relationships, Equations 2.15 through 2.19, in which the dependency on ψ'/ψ_c varies depending on whether ψ'/ψ_c is less than or greater than $(\psi'/\psi_c)_b$. As can be seen in Figure 6.1, the breakoff value for the .12-mm sand, according to Stefanick's relationship, is at about 2.3. For the .20-mm sand, it is at about 3.4. The curve denoted by the dashed line also uses Equation 6.1, but uses the linear curve-fits proposed by M. Rosengaus as inputs for the bedform parameters. Therefore, it does not exhibit a breakoff.

Review of Figure 6.1 shows a good correlation between the friction factors for the two types of sands for ψ'/ψ_c less than approximately 2. For higher values of ψ'/ψ_c, the

data points for the .12- and .20-mm sand separate, which would be expected if the concept of a breakoff point, defined in terms of ψ'/ψ_c, is valid. For the .12-mm sand, the actual breakoff value appears to be located at a ψ'/ψ_c of 2.0, which is relatively close to 2.3, the value that is obtained when using Equation 2.17. For the .20-mm sand, an actual breakoff value appears to be located at a ψ'/ψ_c of 2.7, which is much less than the predicted value of 3.4. In addition, the data points for the higher values of ψ'/ψ_c still do not match the predicted curves. At these higher flow intensities, the data points all fall below the curves that are based on Equations 2.15 through 2.19.

The same trends are also evident in Figure 6.2, which shows bottom roughness normalized by the bottom excursion amplitude or relative roughness, k_b/A_b, plotted against ψ'/ψ_c. In this figure, the data points were directly converted from friction factors to relative roughnesses using the Grant-Madsen f_w to k_b/A_b relationship. Again, the relationships match the data quite well for lower values of ψ'/ψ_c and a breakoff range does appear to exist. However, the breakoff values do not appear to be accurately predicted and the relationships for higher values of ψ'/ψ_c do not accurately correlate with the data.

Rosengaus (1987) also considered another interpretation of relative roughness. Instead of normalizing the bottom roughness against the excursion amplitude, he normalized it against the average grain diameter. He found that the relative roughness (k_b/d) data for experiments with the .20-mm sand could be approximated by a constant k_b/d of 275. Then, given A_b, the Grant Madsen f_w to k_b/A_b relationship can be used to define a friction factor. He found that, of the relationships available, this procedure provided the best fit to the friction factor data.

Here, the procedure discussed in the above paragraph was additionally applied to .12-mm sand. The resulting plot of f_w vs. ψ'/ψ_c is shown in Figure 6.3. In this figure,
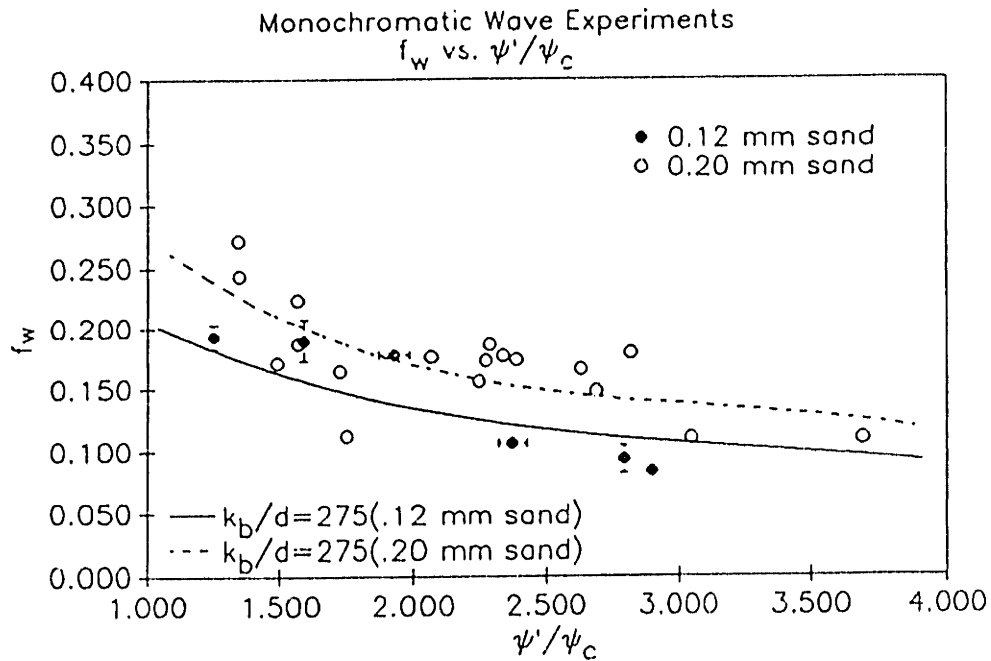
Figure 6.3   FDB friction factor for monochromatic waves - Comparison with curves based on "$k_b/d = 275$" assumption (Model 3)

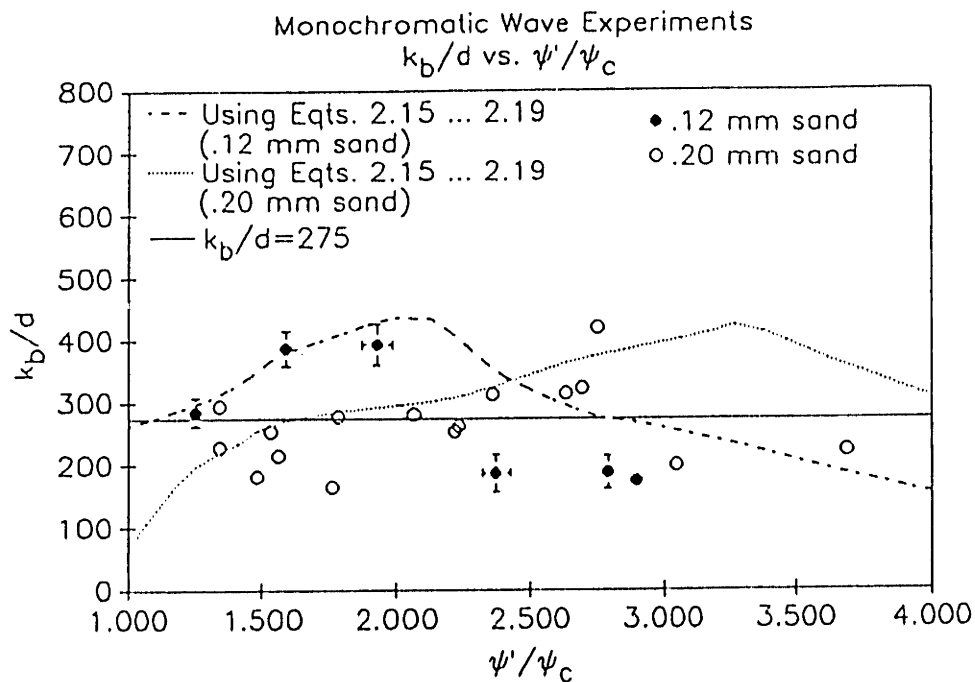
Figure 6.4   FDB relative roughness for monochromatic waves normalized by grain size - Comparison with curves based on Stefanick's relationships and "$k_b/d = 275$" assumption (Model 3)

the solid line represents the friction factor for a k_b/d of 275 for the .12-mm sand, and the dashed line represents the friction factor for the same k_b/d for the .20-mm sand. As can be seen in the figure, the curve provides a reasonable fit to the data for the .20-mm sand. However, for the .12-mm sand, the fit is not as good. For this case, the data points for ψ'/ψ_c less than 2.0 fall well above the .12-mm curve, and data points for higher values of ψ'/ψ_c fall slightly below the .12-mm curve.

This trend is also evident in light of the associated plot of k_b/d vs. ψ'/ψ_c, which can be seen in Figure 6.4. In this figure, the solid line represents the constant k_b/d of 275, the dashed line represents k_b/d for the .12-mm sand, and the dotted line represents the k_b/d for the .20-mm sand. These curves were obtained by making use of Equations 2.15 through 2.19 and the excursion amplitude which can be obtained with knowledge of the Relative Shields Parameter. The data points were obtained directly from friction factors by making use of the Grant Madsen relationship as before.

In this figure, the same trends noted above can be observed. The calculated k_b/d matches the data relatively well for the lower values of ψ'/ψ_c, but provides a relatively poor match for higher values of ψ'/ψ_c, as discussed above. The constant value for k_b/d of 275 is basically representative of the average of all of the data points, but obviously cannot yield any insight into any breakoff characteristics.

In summary, review of the data indicates some type of a breakoff. In addition, a dependence on grain size is observed, with the data for the .12-mm and .20-mm sands breaking off at different values of ψ'/ψ_c and displaying separate trends in these breakoff ranges. Naturally, equations that do not account for these breakoff characteristics would provide a relatively poor fit to the data. Comparison to the data appears to indicate that this is the case. However, the existing equations that do incorporate the concept of a breakoff range dc not accurately match the data either. More specifically,

the predicted breakoff values do not match the observed values, and the predicted relationships do not match the data at higher wave intensities. Therefore, the next step might be to attempt to verify whether there is or is not a breakoff range.

6.1.2 Verification of Breakoff Concepts

There are two concerns involving the concept of a breakoff range. First, there was no clear breakoff range that could be observed in the bedform geometry parameters that were obtained. Second, the breakoff values observed do not match well with the relationship defined by Stefanick (1979).

First, the bedform geometry parameters, discussed in Chapter 5, include the nondimensional bedform height, η/A_b, the ripple steepness, η/λ, the nondimensional bedform length, λ/A_b, and the asymmetry, α. The bedform height and steepness are commonly taken to be the primary factors that affect the equivalent bottom roughness. Since there was no clear observable breakoff value for either of these two parameters, one might suspect that there is some other bedform characteristic influencing the equivalent bottom roughness.

To look at this possibility more closely, two sets of bedform profiles are shown Figures 6.5A and 6.5B. Each set includes six profiles. In Figure 6.5A, the profiles located 10 meters from the wavemaker for all six trials of Experiment B are shown. They are organized with the lowest intensity experiment (B1) at the top and the highest intensity experiment (B5) at the bottom. A similar set of profiles, but at a location 15 meters from the wavemaker, is shown in Figure 6.5B.

Review of these two sets of profiles does indicate that there is a transition that occurs at a ψ'/ψ_c approximately equal to 2.0. This can be seen by comparing the top three profiles (Experiments B1, B2, and B6) with the bottom three profiles
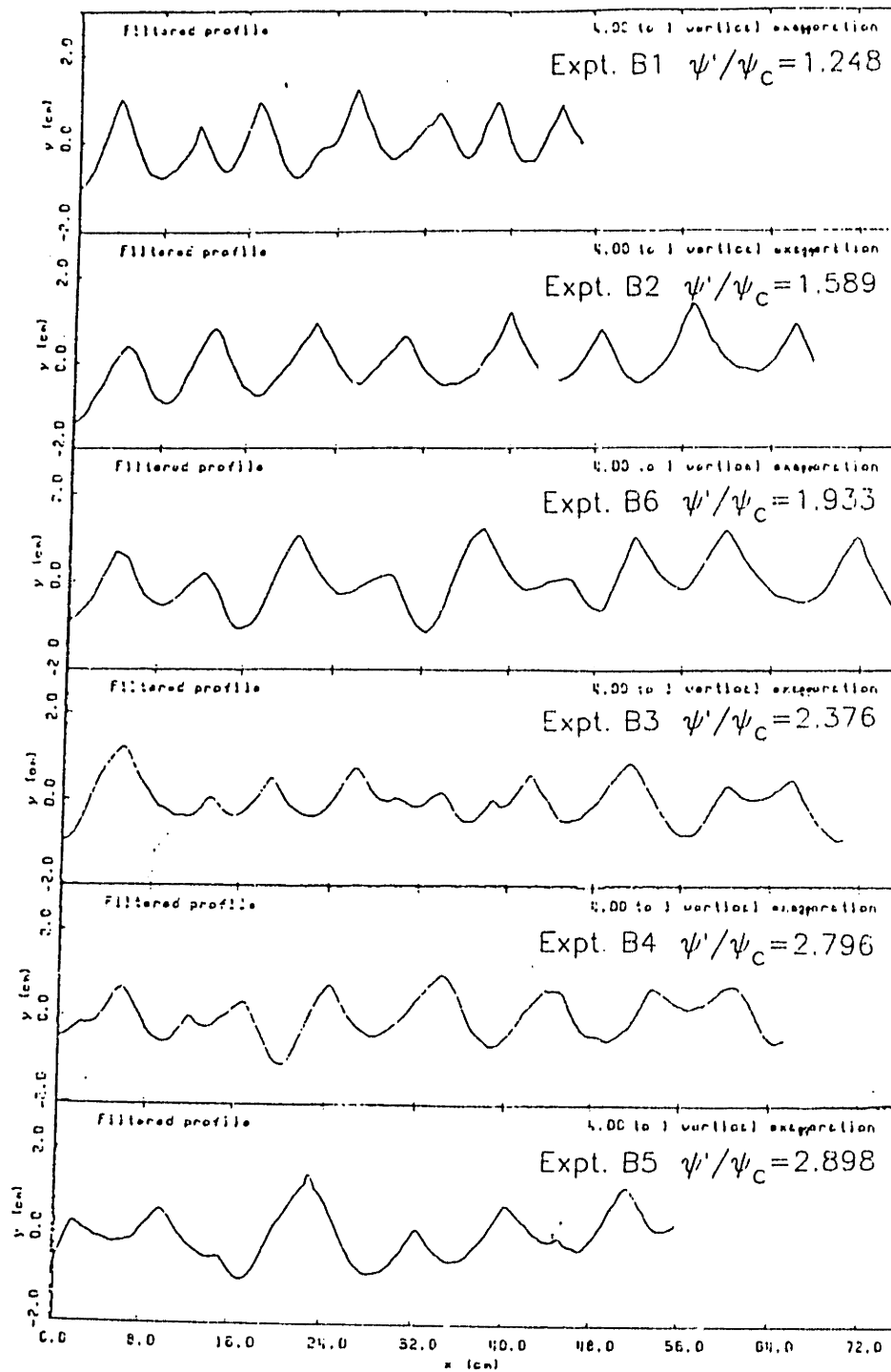
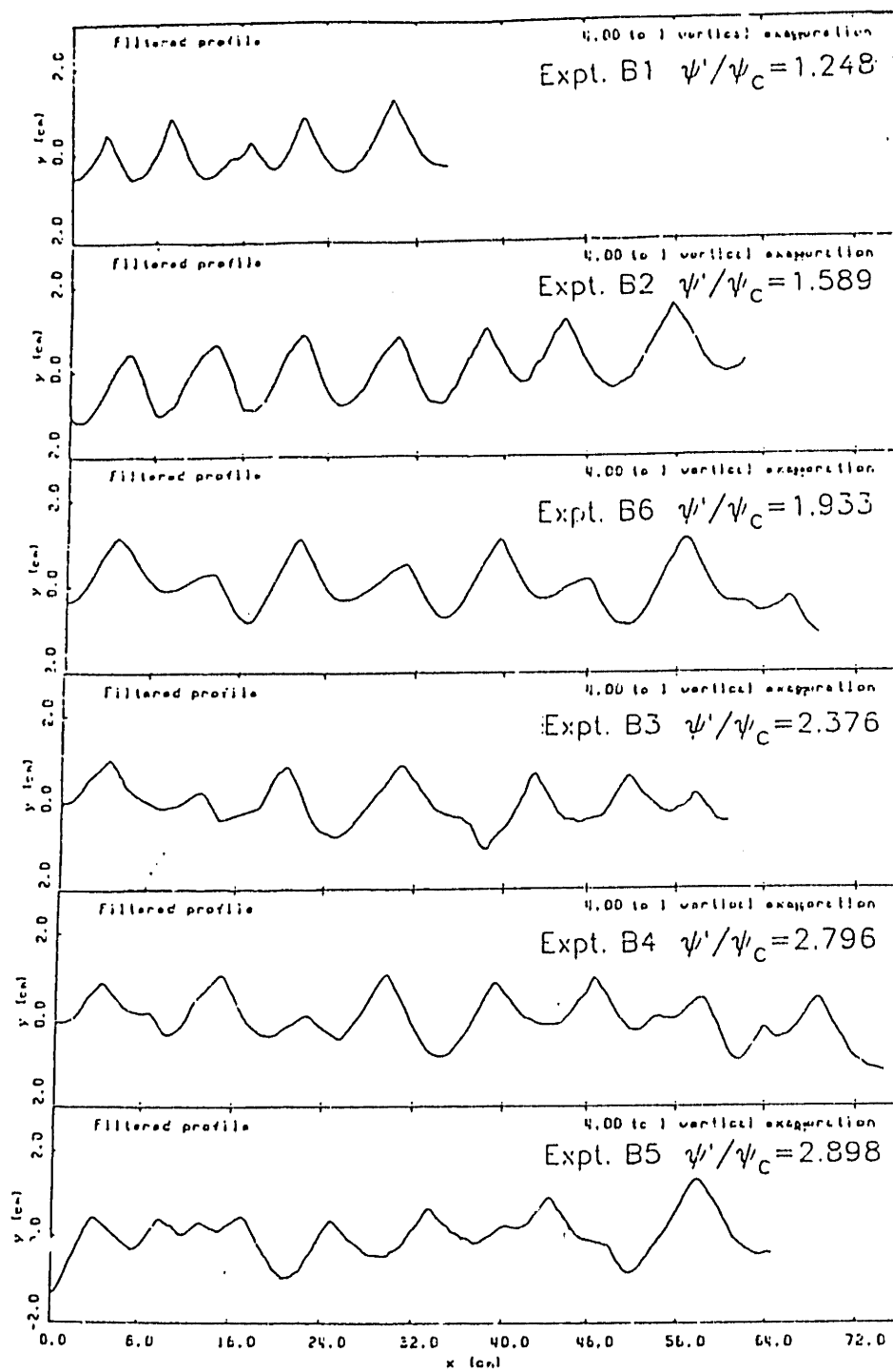Figure 6.5A   Filtered ripple profiles for monochromatic waves, 10.5 meters from the wavemaker

Figure 6.5B Filtered ripple profiles for monochromatic waves, 13.5 meters from wavemaker

- 124 -

(Experiments B3, B4, and B5). It appears as though the bottom three profiles of these two figures are more random in nature. Also, the crests of the ripples for the bottom profiles appear to be less peaked than the top three, as if they have been shaven off. While the difference between the bottom three and top three profiles is rather subtle, a distinction is apparent. This distinction may provide an explanation for the breakoff range observed in the friction factor and relative roughness results.

As previously noted, breakoffs were observed at a ψ'/ψ_c of 2.0 for the .12-mm sand, and a ψ'/ψ_c of 2.7 for the .20-mm sand. These observed breakoff values are both lower than those predicted by Stefanick's relationship (Equation 2.17). In addition, the two values are somewhat lower than any of those values predicted by Equations 5.5 and 5.6, the modified breakoff relationships proposed in Section 5.3.1.2.2.

However, we can compare these breakoff values to the data plotted in Figures 5.10A and 5.10B. As can be seen in those figures, the breakoff data for the bedform geometry parameters are widely scattered, and the observed values noted above fall well within the range of variability of the numerous other experiments. Therefore, the fact that the breakoff value predicted by Stefanick's relationship does not match very well with the observed breakoff values should not be of serious concern.

6.1.3 Improvements Based on Updated Breakoff Range

In Section 5.2.1.2.2, the bedform geometry relationships proposed in Stefanick (1979) were modified to account for the presence of different breakoff characteristics for the different bedform parameters. These modified relationships can be used to develop an improved model for the representation of bottom roughness and wave attenuation in terms of a friction factor.

To accomplish this, the updated bedform relationships, which include Equations 2.16, 2.17, 2.19, and 5.5 through 5.7 are used in conjunction with Equation 6.1 to provide a prediction of relative roughness. The resulting representation of the relative roughness is plotted in Figure 6.6. In this figure, the curve for the .12-mm sand is only slightly affected, while the curve for the .20-mm sand is improved somewhat. Also, while the curve for the .20-mm sand is moved closer to the data points, both curves still lie well above the data points in the breakoff range.

This trend is also reflected in the plot for the friction factor shown in Figure 6.7, where the Grant-Madsen relationship between f_w and k_b/A_b has been used. Again, however, for wave intensities well into the breakoff range, the .20-mm curve does provide a slightly better fit to the data.

6.1.4 Summary of Attenuation Models Evaluated

In the preceding sections, four different predictive models for characterization of wave attenuation over bedforms were presented. To summarize, three of these were based on existing relationships and all of them used Grant and Madsen's equation for relating friction factor to relative roughness. The first of these three models, which we might call Model 1, made use of the relationships first presented in Stefanick (1979), Equations 2.15 through 2.19 to define the bedform geometry and then Equation 6.1 to obtain the relative roughness. In this model, a dependence on the grain size is accounted for in the relationship for the breakoff value and bedform parameters in the breakoff range. The second model, which we can refer to as Model 2, used linear curve fits to the bedform geometry along with Equation 6.1 to define the relative roughness. Here, no possibility of a breakoff range or grain size dependence was accounted for. The resulting attenuation relationships obtained when using Models 1 and 2 are shown in Figures 6.1 and 6.2.
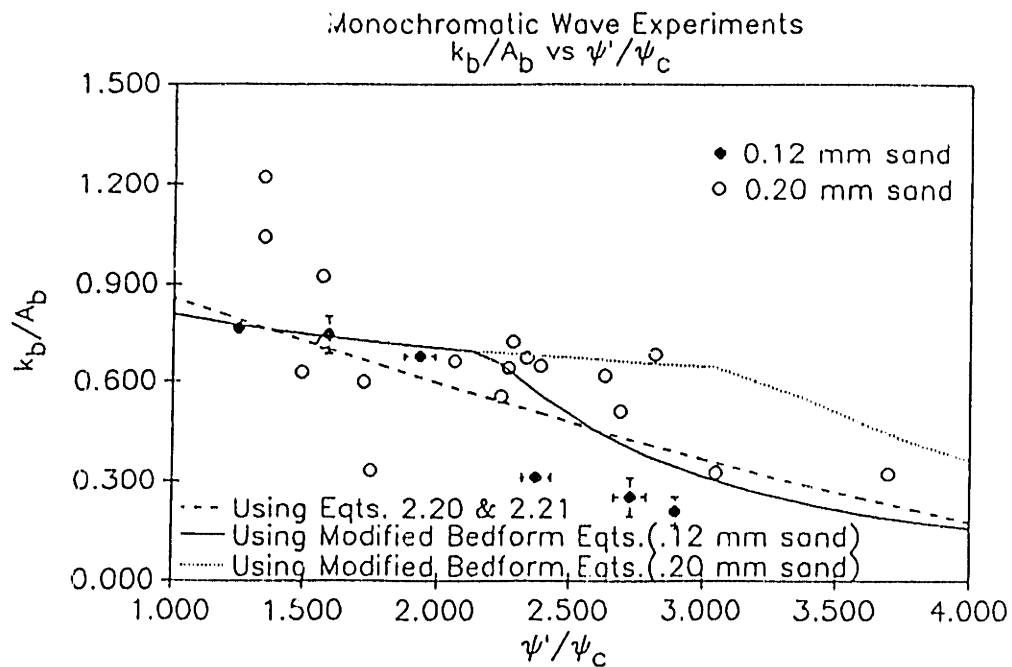
Figure 6.6   FDB relative roughness for monochromatic waves – Comparison with
curves based on updated breakoff range and modified bedform
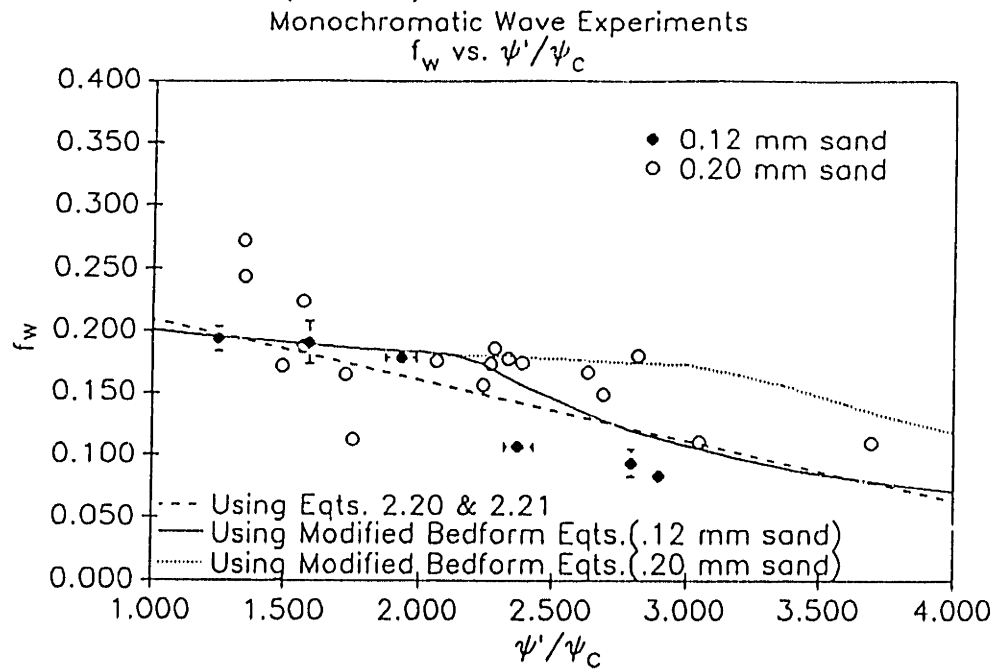relationships (Model 4)

Figure 6.7   FDB friction factor for monochromatic waves – Comparison with curves
based on updated breakoff range and modified bedform relationships
(Model 4)

The next method reviewed was one proposed by Jonsson (1966) and used in Rosengaus (1987). In this model (call it Model 3) the equivalent bottom roughness, k_b, was normalized against the mean grain diameter. Therefore, although no breakoff was accounted for, a grain size dependence was included. Since this parameter, k_b/d, was found to be of the order of 275 for all values of ψ'/ψ_c for the .20-mm sand, this value was taken as constant. Then, with k_b/d taken as 275, and with knowledge of the relationship between the bottom excursion amplitude and ψ'/ψ_c, the distribution of k_b/A_b could be found. This in turn could be used to obtain a predicted distribution for the friction factor, which is shown in Figure 6.3.

The final predictive model proposed, Model 4, was similar to that presented in Stefanick (1979). However, in the modified version, two different breakoff relationships were defined instead of the one relationship used by Stefanick. Therefore, one was associated with η/λ, and another improved relationship was associated with η/A_b, as discussed in the previous section. A revised η/A_b relationship was then defined for use when ψ'/ψ_c exceeded the appropriate value. Again, Equation 6.1 was used to obtain the relative roughness. The attenuation relationships for this model can be found in Figures 6.6 and 6.7.

6.1.5 Proposed Relationships

Of all of the predictive models presented, this final model, Model 4, which makes use of the revised η/A_b relationship, is proposed for use in characterizing wave attenuation. This method is preferable because of two principal reasons. First, it provides a reasonable fit to the data. Secondly, it is physically more realistic because it accounts for the existence of a breakoff range and also includes a dependence on the grain size, which is clearly exhibited by the experimental data.

The advantages of this model can be shown by review of the friction factor results summarized in Figures 6.1, 6.3, and 6.7, which were described in Section 6.1.1. In summary, the use of Stefanick's relationships (Model 1), while not providing an accurate match to data points at higher wave intensities, does account for the presence of a breakoff range. The use of linear curve fits (Model 2), which provides a reasonable match for the .20-mm data, does not provide an accurate match when the additional .12-mm data is included. In addition, this model naturally does not account for a breakoff range or grain size dependence. The constant k_b/d assumption, used in Model 3, while including a grain size dependence, also neglects any possibility of a breakoff. In addition, the distribution predicted by this model provides a reasonable fit to the .20-mm data, but provides a poor fit to the .12-mm data. The final model, which was developed by modifying Stefanick's bedform geometry relationships, still does not provide an accurate match to the data for higher values of ψ'/ψ_c. However, it is a slight improvement over Model 1. Also, it accounts for the presence of a breakoff range, and provides a reasonable overall fit to the data for the .12- and .20-mm sands.

To estimate the accuracy of this fit, we can consider the ratio of a predicted friction factor to the actual measured friction factor, $(f_w)_{pred}/(f_w)_{meas}$, and determining the mean and standard deviation for this parameter. If this is done, the mean is 1.09, indicating that the model overestimates the friction factor slightly. The associated standard deviation for this parameter is .20, implying that the accuracy of the model is approximately ± 20 percent.

6.2 Spectral Waves

6.2.1 Comparison with Existing Relationships

As discussed in Chapter 2, the purpose of the spectral wave experiments was to verify a simple procedure for characterizing spectral attenuation over a movable sediment bed. In this procedure, the spectral attenuation is modeled by the attenuation associated with an equivalent monochromatic wave having the same near-bottom velocity and excursion amplitude as the root-mean-square bottom velocity and excursion amplitude of the wave spectrum. This procedure would provide the benefit of allowing the relationships associated with monochromatic waves, which have been studied extensively, to be applied to wave spectra. The wave spectrum experimental procedures used to accomplish this goal were discussed in detail in Chapter 4.

The attenuation results for these experiments are summarized in Tables 6.2A, 6.2B, and 6.2C. Tables 6.2A and 6.2B include the results of the Pierson-Neumann spectral wave experiments for the .12- and .20-mm sands, respectively. Table 6.2C summarizes the results of the JONSWAP spectral wave experiments. These tables include summaries of wave characteristics and friction factor data for each of the components of the spectral experiments completed. Also, in the rows of the tables entitled "rep," the characteristics associated with the representative monochromatic wave (discussed in Chapter 2) are listed for the various experiments. These rows also include the representative friction factors, associated equivalent bottom roughnesses, and the mean bedform data. The standard deviations associated with these representative values and mean bedform data are summarized in the rows entitled "s.d." Again, these representative values for the spectral characteristics are not simply the means of the values for the associated spectral components. They are obtained by using the procedure detailed in Section 2.2.2. In addition, the standard deviations are associated

Table 6.2A
Spectral FDB Experimental Results for .20 mm Sand

Spectral Wave Experiments using .20 mm sand

Expt ID	Component #	frequency (rad/sec)	wavenumber (1/cm)	Amplitude (cm)	Near Bottom Exc.Amp. (cm)	Near Bottom Orb.Vel. (cm/sec)	Relative Shields Parameter	Friction Factor	Roughness (cm)	Bedform Geometry Height (cm)	Steepness
S1	1	2.011	0.009402	1.45	2.98	6.00		0.297			
	2	2.450	0.011661	1.55	2.51	6.16		0.090			
	3	2.890	0.014517	1.33	1.68	4.86		0.453			
	4	3.456	0.017373	1.41	1.44	4.96		0.114			
	5	4.650	0.025693	1.45	0.87	4.04		0.460			
	rep	2.581	0.012356	3.00	4.56	11.77	1.287	0.230	5.226	NA	NA
	s.d.							0.037	1.172		
S2	1	2.011	0.009402	1.55	3.17	6.37		0.330			
	2	2.450	0.011661	1.64	2.67	6.53		0.101			
	3	2.890	0.014517	1.32	1.66	4.81		0.203			
	4	3.456	0.017373	1.49	1.51	5.23		0.107			
	5	4.650	0.025693	1.56	0.9c	4.36		0.188			
	rep	2.571	0.012302	3.15	4.81	12.36	1.349	0.175	3.428	1.080	0.141
	s.d.							0.023	0.635	0.113	0.008
S3	1	2.011	0.009402	3.04	6.24	12.55		0.042			
	2	2.450	0.011661	2.79	4.53	11.09		0.020			
	3	2.890	0.014517	2.34	2.95	8.54		0.024			
	4	3.456	0.017373	2.32	2.37	8.18		0.187			
	5	4.650	0.025693	2.36	1.42	6.59		-0.012			
	rep	2.480	0.011818	5.43	8.68	21.53	2.456	0.047	0.582	0.950	0.110
	s.d.							0.020	0.547	0.142	0.010
S4	1	1.902	0.008862	2.78	6.08	11.57		0.119			
	2	2.393	0.011360	2.21	3.68	8.82		0.109			
	3	2.823	0.013574	2.08	2.81	7.94		0.039			
	4	3.375	0.016878	1.93	2.03	6.87		0.075			
	5	4.602	0.025318	1.91	1.17	5.40		-0.111			
	rep	2.338	0.011073	4.67	8.01	18.73	1.792	0.033	1.362	NA	NA
	s.d.							0.018	0.397		
S5	1	1.902	0.008862	2.00	4.36	8.29		0.240			
	2	2.393	0.011360	1.73	2.88	6.90		0.184			
	3	2.823	0.013674	1.49	2.02	5.71		0.107			
	4	3.375	0.016878	1.56	1.65	5.56		0.129			
	5	4.602	0.025318	1.52	0.93	4.29		0.130			
	rep	2.377	0.011276	3.52	5.92	14.08	1.381	0.167	3.984	1.183	0.140
	s.d.							0.012	0.265	0.305	0.022

Table 6.2B
Pierson–Neumann Spectral FDB Experimental Results for .12 mm Sand

Pierson-Neumann Spectral Wave Experiments using .12 mm sand

Expt ID	Component #	Frequency (rad/sec)	Wavenumber (1/cm)	Amplitude (cm)	Near Bottom Exc.Amp. (cm)	Near Bottom Orb.Vel. (cm/sec)	Relative Shields Parameter	Friction Factor	Roughness (cm)	Bedform Geometry Height	Steepness
C1	1	1.963	0.008425	2.27	4.31	8.46		0.132			
	2	2.393	0.010478	2.26	3.37	8.06		0.171			
	3	2.823	0.012667	1.82	2.17	6.14		0.051			
	4	3.375	0.015745	1.96	1.80	6.07		0.119			
	5	4.541	0.023635	1.91	0.98	4.45		0.073			
	rep	2.437	0.010695	4.28	6.23	15.19	1.608	0.118	2.710	1.052	0.128
	s.d.							0.034	1.059	0.080	0.009
C2	1	1.963	0.008425	2.28	4.32	8.49		0.109			
	2	2.393	0.010478	2.22	3.31	7.91		0.117			
	3	2.823	0.012667	1.90	2.27	6.41		0.233			
	4	3.375	0.015745	2.07	1.90	6.40		-0.016			
	5	4.541	0.023635	1.88	0.96	4.38		-0.030			
	rep	2.449	0.010755	4.33	6.27	15.36	1.621	0.101	1.818	1.095	0.138
	s.d.							0.034	0.984	0.124	0.009
D1	1	1.963	0.009167	2.58	5.45	10.69		0.112			
	2	2.393	0.011360	2.20	3.67	8.78		0.065			
	3	2.823	0.013737	2.05	2.77	7.81		-0.004			
	4	3.375	0.016878	2.06	2.17	7.33		0.104			
	5	4.541	0.027841	2.00	1.06	4.80		0.030			
	rep	2.435	0.011580	4.56	7.45	18.14	2.282	0.066	1.110	1.087	0.116
	s.d.							0.031	0.886	0.132	0.008
D2	1	1.963	0.009167	2.65	5.59	10.97		0.088			
	2	2.393	0.011360	2.30	3.84	9.20		0.164			
	3	2.823	0.013737	2.07	2.79	7.88		0.011			
	4	3.375	0.016878	1.99	2.10	7.08		0.070			
	5	4.541	0.027841	1.98	1.05	4.75		0.060			
	rep	2.417	0.011485	4.62	7.63	18.43	2.345	0.080	1.694	1.111	0.122
	s.d.							0.025	0.839	0.129	0.010
E1	1	1.963	0.008425	1.98	3.75	7.36		0.156			
	2	2.393	0.010478	1.97	2.94	7.03		0.240			
	3	2.823	0.012667	1.61	1.93	5.44		0.138			
	4	3.375	0.015745	1.84	1.69	5.69		0.100			
	5	4.541	0.023649	1.76	0.91	4.11		-0.036			
	rep	2.462	0.010819	3.82	5.49	13.51	1.544	0.142	2.833	1.218	0.158
	s.d.							0.017	0.483	0.116	0.011

Table 6.2C

JONSWAP Spectral FDB Experimental Results for .12 mm Sand

JONSWAP Spectral Wave Experiments using .12 mm sand

Expt ID	Component #	frequency (rad/sec)	wavenumber (1/cm)	amplitude (cm)	Near Bottom Exc.Amp. (cm)	Near Bottom Orb.Vel. (cm/sec)	Relative Shields Parameter	Friction Factor	Roughness (cm)	Bedform Geometry Height	steepness
F1	1	2.270	0.0107219	2.14	3.81	8.65		0.040			
	2	2.454	0.016821	2.19	3.54	8.69		0.209			
	3	2.761	0.0133345	2.01	2.81	7.75		0.127			
	4	3.375	0.0168777	2.02	2.13	7.18		0.065			
	5	4.295	0.0229977	1.97	1.39	5.97		0.014			
	rep	2.680	0.0128905	4.44	6.44	17.25	1.987	0.102	1.777	1.032	0.125
	s.d.							0.017	0.502	0.171	0.006
F2	1	2.270	0.0107219	2.33	4.14	9.40		0.260			
	2	2.454	0.016821	2.06	3.33	8.17		0.126			
	3	2.761	0.0133345	2.04	2.84	7.84		-0.013			
	4	3.375	0.0168777	2.05	2.16	7.30		-0.021			
	5	4.295	0.0229977	1.98	1.39	5.97		0.312			
	rep	2.666	0.0128144	4.49	6.56	17.48	2.046	0.133	2.560	1.135	0.131
	s.d.							0.019	0.610	0.106	0.006
G1	1	2.270	0.009879	1.78	3.46	7.86		0.283			
	2	2.454	0.010781	1.86	3.29	8.06		0.178			
	3	2.761	0.012345	1.68	2.56	7.08		0.098			
	4	3.375	0.015745	1.68	1.93	6.50		0.092			
	5	4.295	0.021779	1.57	1.19	5.12		0.187			
	rep	2.650	0.011769	3.68	5.91	15.66	1.538	0.174	3.812	1.210	0.160
	s.d.							0.032	1.046	0.100	0.014
H1	1	2.270	0.009879	2.00	3.88	8.82		0.066			
	2	2.454	0.010781	2.06	3.65	8.95		0.306			
	3	2.761	0.012345	1.86	2.82	7.80		0.007			
	4	3.375	0.015745	1.89	2.17	7.31		0.125			
	5	4.295	0.021779	1.83	1.39	5.98		0.076			
	rep	2.677	0.0128727	4.51	6.55	17.54	1.764	0.128	2.653	NA	·
	s.d.							0.017	0.550		
I1	1	2.270	0.009879	2.35	4.56	10.35		0.065			
	2	2.454	0.010781	2.32	4.09	10.05		0.262			
	3	2.761	0.012345	2.07	3.15	8.70		-0.059			
	4	3.375	0.015745	2.21	2.53	8.55		0.140			
	5	4.295	0.021779	2.13	1.62	6.94		0.101			
	rep	2.680	0.0128905	5.18	7.51	20.13	2.284	0.108	2.110	1.022	0.125
	s.d.							0.013	0.451	0.210	0.011
J1	1	2.270	0.009879	2.36	4.58	10.40		0.005			
	2	2.454	0.010781	2.55	4.51	11.07		0.146			
	3	2.761	0.012345	2.23	3.40	9.38		0.296			
	4	3.375	0.015745	2.20	2.53	8.54		-0.001			
	5	4.295	C.021779	2.14	1.62	6.96		0.055			
	rep	2.680	0.0128905	5.40	7.83	20.98	2.484	0.102	2.271	NA	NA
	s.d.							0.009	0.438		

with the scatter of the representative values found from each of the experimental runs completed.

To analyze the attenuation results, the spectral results were compared to the monochromatic results. If the use of the representative monochromatic wave for characterizing bedform geometry and relating it to spectral attenuation is valid, there should be a correspondence between the spectral results and monochromatic results. Unfortunately, as can be seen in Figure 6.8, this correspondence is poor. In that figure, the representative friction factors for the spectral experiments are plotted against the representative Shields Parameter. The monochromatic friction factor results, along with various curves, are also shown. The solid and dotted curves were defined using Equations 2.15 through 2.19, 6.1, and 2.25. Also, it was apparent that use of the linear curve fits to monochromatic bedform geometry along with Equations 6.1 and 2.25 would not provide a fit to the spectral friction factor data. Therefore, the curve fits to the spectral bedform geometry, Equations 5.8 and 5.9, were used along with Equations 6.1 and 2.25. The resulting relationship is plotted as the dashed line in Figure 6.8.

Review of this figure shows that the spectral friction factors generally are less than the monochromatic friction factors. Apparently, any differences between magnitudes of the monochromatic and spectral bedform parameters are insufficient in accounting for the differences in friction factor estimates. Certainly, the curves obtained from the equations noted above have no application to the spectral data. Also, it is obvious that the discrepency is so significant that the modified curves discussed in Section 6.1.3 would not render any reasonable correlation. Therefore, they were not included in this figure.

One of the conclusions of Rosengaus (1987) was that the attenuation characteristics of wave spectra can be accurately represented by the assumption of a single
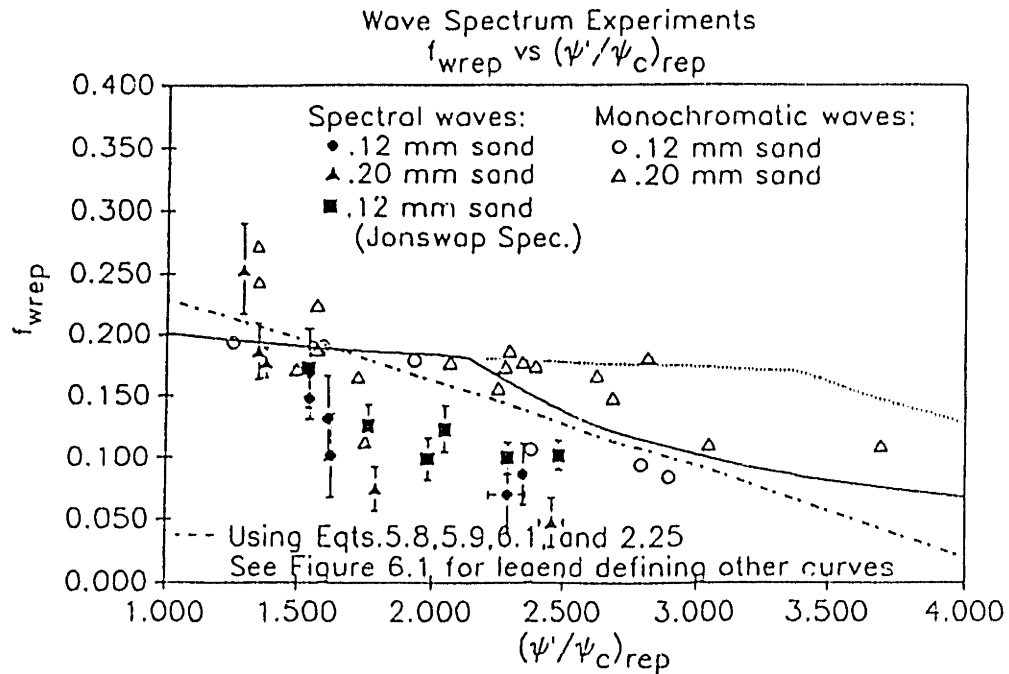
Figure.6.8   FDB friction factor for spectral waves – Comparison with curves based on
Stefanick's relationships and linear curve fits to spectral bedform data
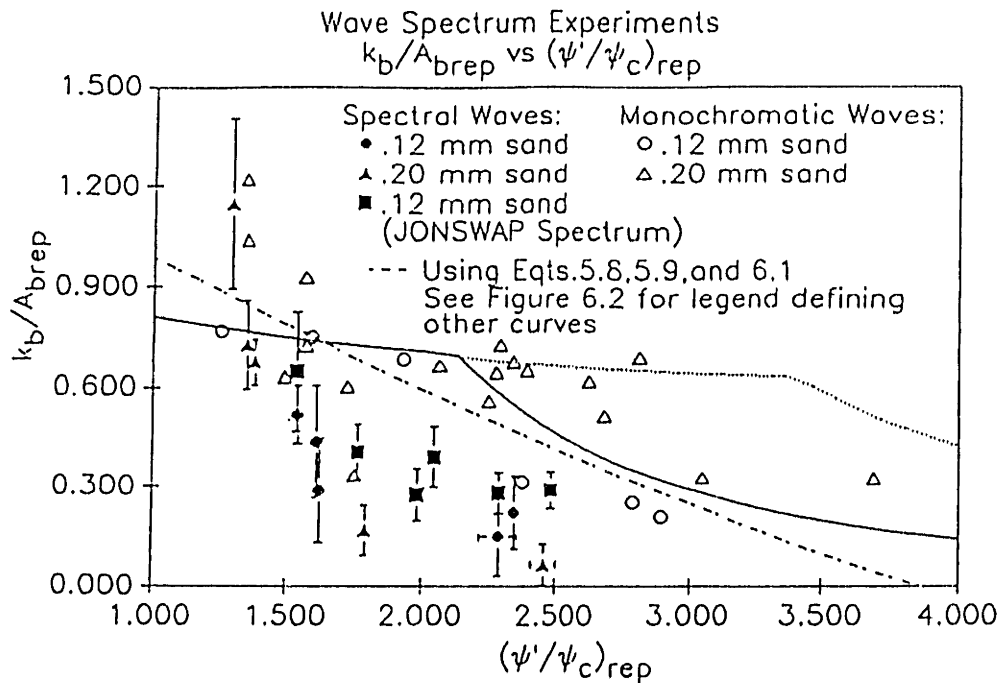

Figure 6.9   FDB relative roughness for spectral waves – Comparison with curves
based on Stefanick's relationships and linear fits to spectral bedform data

monochromatic wave based on an equivalent rms bottom velocity. However, this conclusion was preliminary since it was based on experiments that were of relatively low wave intensity. As is shown by the results plotted in Figure 6.8, the recent experiments, for which much higher spectral wave conditions were also tested, showed that this conclusion is not correct. A single equivalent monochromatic wave cannot be used to represent both the bedform geometry and attenuation characteristics of a wave spectrum.

However, review of the Figure 6.8 reveals that this spectral representation does provide some benefits. First, although the spread in the spectral friction factor data is relatively wide, the data for the .12-mm and .20-mm sands basically fall on the same line. This observation indicates that the use of a representative Shields Parameter to characterize spectral attenuation in terms of a friction factor is reasonable. In addition, no specific breakoff values can be identified, or, if a breakoff does exist its ψ'/ψ_c would be less the ψ'/ψ_c values for the experiments completed. In any event, no spectral breakoff can be justifiably defined using the spectral experimental data available. This would imply that the concept of a breakoff value defined in terms of S_* is not appropriate for spectral waves.

Secondly, while the experiments completed deterministically represented wave spectra of chosen intensity, different phase relationships between the various spectral components, randomly chosen, were simulated. Specifically, for each of Experiments C, D, and F, two realizations of the same spectrum were tested. This means that, for each of these experiments, two different random seeds were chosen to define the phase relationships between different components of the spectrum. If one locates the points for these experiments on Figure 6.8 by making use of the information summarized in Table 6.2, it is apparent that the relative phases of the different components does not have any notable impact on the results.

The final point of interest regarding Figure 6.8 involves the comparison between the friction factor results for the JONSWAP spectra, identified by the filled square symbols, and those for the Pierson–Neumann Spectra, identified by the filled circular and triangular symbols. As discussed in Chapter 3, the JONSWAP spectrum is relatively narrow banded and the Pierson–Neumann spectrum is quite broad banded. Since no significant difference can be noted between friction factors of these two spectral shapes, it is apparent that the attenuation characteristics are independent of spectral shape.

This observation identifies an important concept regarding spectral attenuation. As opposed to considering the wave spectrum in a deterministic sense, we might view it in a stochastic sense. If we consider a stochastic interpretation of a wave spectrum, we would expect that the amplitude of any single frequency component as well as the combined peak values of any wave–associated variable are Rayleigh distributed. Therefore, if we have a narrow-banded spectrum representing an irregular wind sea, we expect the maxima of the near-bottom orbital velocities to be Rayleigh distributed. Thus, we expect that, as the spectral width is reduced towards a single component, the spectral characteristics do not approach the limit of a monochromatic wave. Since the friction factor results appear to be independent of spectral shape, these concepts are verified.

Next, to look at the attenuation characteristics of wave spectra from another angle, the representative relative roughness for the wave spectra is plotted against the representative Shields Parameter in Figure 6.9. In this figure, Equation 2.25 is used to convert the friction factors to relative roughnesses. Here, the monochromatic roughnesses are plotted, along with the curve based on line fits to bedform geometry and curves that make use of Equations 2.15 through 2.19 and 6.1. Again, the same trend is obvious, with the spectral results all located well below the monochromatic results. In summary, it is apparent that the differences between bedform parameters of

the spectral and monochromatic wave experiments are not enough to account for the differences in relative roughness or friction factor results. Therefore, the next step is to attempt to explain these differences.

6.2.2 Discussion of the Difference Between Monochromatic and Spectral Attenuation

6.2.2.1 Comparison of Bedform Geometry

To arrive at a plausible explanation for the difference between the monochromatic and spectral attenuation results, we might first consider the bedform geometry itself. As noted in Chapter 5, differences were apparent between the monochromatic and spectral bedform geometry. First, the η/A_{brep} data for the wave spectra were generally slightly less than the corresponding η/A_b data for the monochromatic waves. In addition, the η/λ spectral data were all significantly lower than the monochromatic η/λ data. However, as noted above, these differences were not enough to explain the reduced friction factors associated with the spectral experiments. Therefore, the next step would be to determine whether a mechanism other than these two parameters may govern the equivalent bottom roughness.

To do this, we can compare the bedform profiles of the various experiments. A number of bedform profiles are shown in Figures 6.10A and 6.10B. In 6.10A, sample profiles for Experiments E1, C1, and D1 are shown. Experiment E1 represents the lowest wave intensity, with a ψ'/ψ_c of 1.544 and Experiment D1 has the highest intensity, with a ψ'/ψ_c of 2.280. All three of these experiments simulated Pierson-Neumann spectra. In Figure 6.10B, some JONSWAP spectral experiments are shown. Included, in order of increasing intensity, are Experiments G1, H1, and I1.

From these two typical sets of profiles, no clear distinction can be identified between the Pierson-Neumann spectra and JONSWAP spectra. This is reasonable since
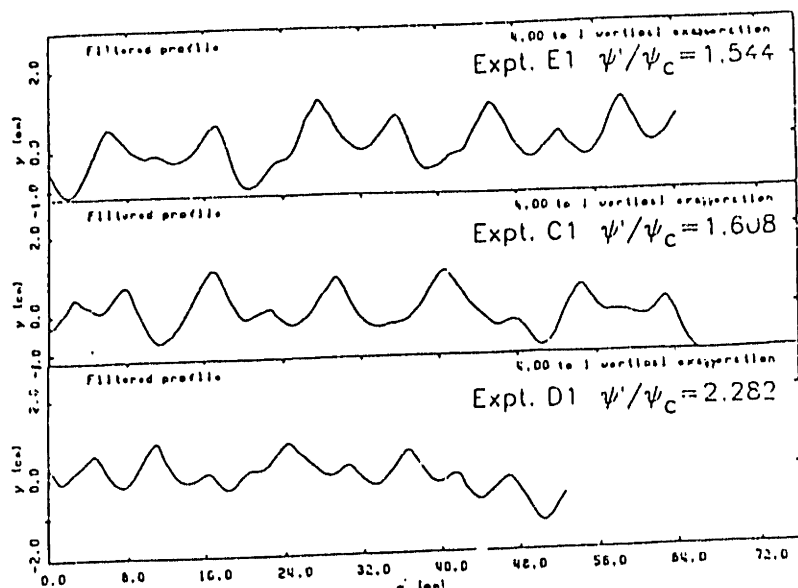
Figure 6.10A Filtered ripple profiles for Pierson-Neumann spectral waves, 13.5 meters from wavemaker
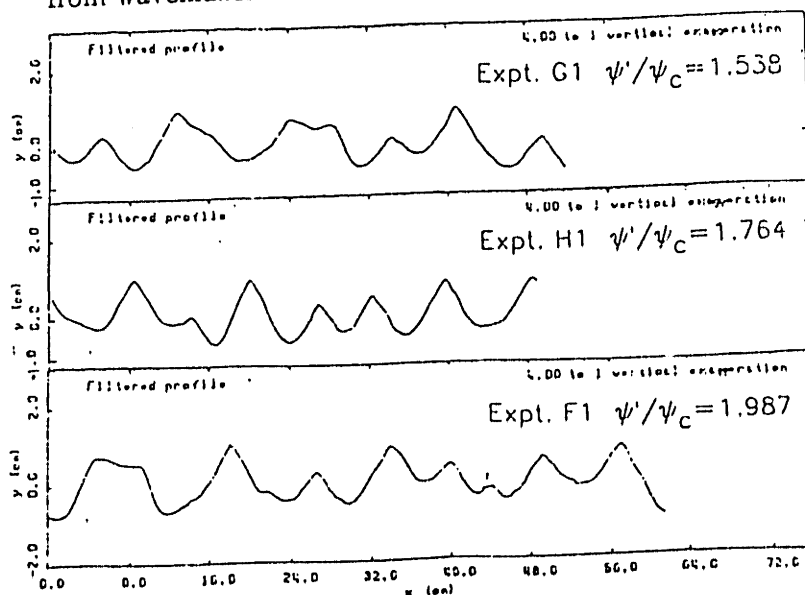

Figure 6.10B Filtered ripple profiles for JONSWAP spectral waves, 13.5 meters from wavemaker

there was no clear distinction between the attenuation characteristics of the Pierson-Neumann and JONSWAP spectra.

However, these two sets of profiles may be compared to those included in Figures 6.5A and 6.5B, the typical monochromatic profiles which were previously discussed in Section 6.1.2. When we compare the profiles of similar spectal intensity (of equal ψ'/ψ_c), a sharp contrast is apparent. For the most part, the crests of the spectral ripples appear to be more rounded than those of the monochromatic ripples. In addition, the ripples associated with the wave spectra appear to more closely resemble the monochromatic ripples that are associated with wave intensities in the breakoff range as discussed in Section 6.1.2 (Experiments B3, B4, and B5), despite the representative value of ψ'/ψ_c being well below the monochromatic breakoff value.

6.2.2.2 Quantification of "Roundedness" of Ripple Crests

To help verify the difference between the monochromatic and spectral ripples, a procedure was developed to quantify this "roundedness" of the ripple crests. In this procedure, an estimate of curvature was made by measuring the bedform surface slope on either side of the ripple crest. More specifically, the measurements were taken at locations where the bedform width was 30 percent of the bedform length, as clarified in Figure 6.11. These two slopes, one positive and one negative, are then used to obtain a parameter that reflects the ripple roundedness. This parameter, $\Delta m/\Delta x$, is defined as:

$$\Delta m/\Delta x = \frac{m_+ - m_-}{.30\lambda} \tag{6.2}$$

and may be interpreted as a rough estimate of the inverse of the radius of curvature. Therefore, we expect that ripples with rounder crests would have lower $\Delta m/\Delta x$ values and ripples with sharper crests would have higher $\Delta m/\Delta x$ values. Keeping this in
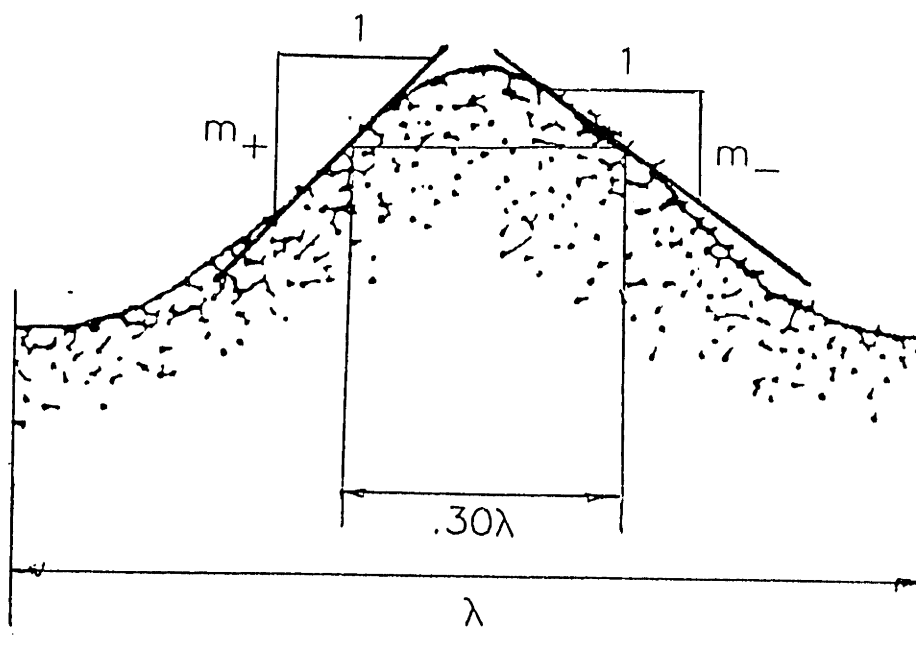
$$\Delta m/\Delta x = \frac{m_+ - m_-}{.30\lambda}$$

Figure 6.11   Schematic to clarify the procedures for developing the "roundedness" parameter, $\Delta m/\Delta x$

mind, the monochromatic and spectral ripples may be compared and any additional effects of roundedness may be clarified.

This investigation, completed by Chris Rehman, the UROP student working on this project, made use of a representative ripple profile from each of the experiments for which bedform geometry was evaluated. A summary of the results is shown in Table 6.3. As can be seen in this table, typical values of $\Delta m / \Delta x$ range from .55 to about .25. The monochromatic experiments noted in the table include Experiments B1 through B6. In general, comparison of monochromatic and spectral results for similar values of $(\psi' / \psi_c)_{rep}$ reveals that the $\Delta m / \Delta x$ values for the spectral ripples are lower than those of the monochromatic ripples. Two exceptions include the $\Delta m / \Delta x$ results for Experiments C2 and E1, which were of relatively low spectral intensity. The results for these two exceptions closely match the result for Experiment B2, which roughly has the same ψ' / ψ_c as the $(\psi' / \psi_c)_{rep}$ values for these spectral experiments.

In general, most spectral $\Delta m / \Delta x$ values are quite similar to the monochromatic $\Delta m / \Delta x$ values associated with the observed monochromatic breakoff range. Of course, this same general trend was prevalent in the ripple steepness (η / λ) results discussed in Section 5.3.2. However, as discussed in Section 6.2.1, the differences between the monochromatic and spectral bedform geometry are not enough to account for the differences observed in monochromatic and spectal wave attenuation. Therefore, while the behavior of this roundedness parameter would naturally be reflected in the η / λ results, the parameter shows that, in addition to the difference in η / λ, there is a definite difference between the monochromatic and spectral bedform geometry when we look more closely at the ripple crests.

Table 6.3

Ripple Roundedness Data

expt	ψ' / ψ_c	$\Delta m / \Delta x$ mean	$\Delta m / \Delta x$ st.dev.
B1	1.25	.55	.03
B2	1.59	.42	.07
E1	1.54	.41	.09
C2	1.62	.41	.07
G1	1.54	.39	.08
S2	1.35	.38	.04
B6	1.93	.35	.02
I1	2.28	.35	.14
D1	2.28	.34	.13
F1	1.99	.34	.08
B3	2.38	.31	.04
C1	1.61	.30	.10
B4	2.80	.30	.08
F2	2.05	.28	.07
B5	2.90	.29	.10
D2	2.34	.27	.02
S3	2.46	.26	.01

6.2.2.3 Physical Explanations and Implications

If we consider the characteristics of spectral wave motion over a rippled sand bed, an explanation can be developed for this phenomenon. The underlying concepts associated with this explanation involve the variety of individual waves that make up the spectrum. While smaller waves may be predominant in the surface profile, the few large waves may still dominate the bedform interaction. It is hypothesized (and to some extent supported by the bed profiles in Figures 6.10A and 6.10B) that the influence of the occasionally large waves on the bottom bedform geometry would be to round off the crests of the ripples, and therefore reduce the effectiveness of these crests as energy dissipators. With the crests of the ripples smoothed out, the turbulent eddies and associated energy dissipation would be reduced. Basically, the time scales required to redevelop any sharper peaks of the ripples appear to be longer than the time scales associated with the occurence of these larger waves. In summary, this reduction in spectral energy dissipation associated with the rounding of the crests of the ripples can explain the difference between the monochromatic and spectral results.

From this physical reasoning, it would appear that, when the root-mean-square (rms) bottom velocity and representative excursion amplitude (defined in Chapter 2) are used to represent the spectral characteristics, the larger waves are not weighted enough. One approach to handle this problem would be somehow place more weight on these larger waves. As an example, one might empirically accomplish this by using what might be called a "significant bottom velocity" as a representative value. For this representative value, the average of the highest one-third of the component bottom velocities could be used.

Unfortunately, a procedure such as this is not really justified. First, while it would still allow us to define a representative monochromatic wave, it would not properly

account for any breakoff range. The breakoff values, which were found to vary for different bedform parameters and values of S_* for monochromatic waves, were not observed in the spectral experiments. In addition, the breakoff concept as discussed in Section 6.1.2 does not appear to be appropriate for spectral waves since, for most values of ψ'/ψ_c, the crests of the ripples are rounded or shaved off due to the effect of larger waves. This means that the idea of ripples being shaved off purely by the wave intensity (as in the monochromatic breakoff range) does not appear to apply for spectral waves. In effect, because of the absence of distinct breakoffs in the spectral data for either of the two sands, any modifications to representative parameters describing spectral characteristics would appear to be inappropriate.

The idea also simply would not work well because of the bedform characteristics. The procedure might shift the attenuation data (f_w and k_b/A_b) so that it is relatively close to the monochromatic curves. However, if this is done, the bedform geometry data, especially η/λ, for which the spectral data is well below the monochromatic data, cannot be appropriately represented.

To summarize, the spectral attenuation and bedform characteristics cannot be simultaneously represented by the attenuation and bedform characteristics of a single monochromatic wave. The inadequacy of the use of a representative monochromatic wave in this manner results due to the important effect of the larger waves of the spectrum, which round off the crests of bedforms and therefore reduce the effectiveness of these bedforms as energy dissipators.

6.2.3 Proposed Relationships

Since the concepts of a single representative monochromatic wave cannot be used to relate bedform geometry to attenuation characteristics for a wave spectrum, the best we can do is define curve fits to the data.

Therefore, two possibilities for representing the spectral friction factor results are considered: a linear curve fit and a power law fit.

The linear curve fit to the spectral friction factor data yields the following relationship:

$$f_{w,rep} = .3157 - .1025 \ (\psi'/\psi_{c,rep}) \tag{6.3}$$

This relationship is shown as the dashed line in Figure 6.12. The power law relationship was found to be:

$$f_{w,rep} = .293 \ (\psi'/\psi_{c,rep})^{-1.56} \tag{6.4}$$

This relationship is also shown on Figure 6.12 as the curved solid line.

Of these two empirical relationships, the preferred one is the power law relationship. It is the better alternative because use of the linear relationship results in negative friction factors for values of $\psi'/\psi_{c,rep}$ that are greater than about 3.0, which, for obvious reasons is unreasonable. Equation 6.4 results in a friction factor of .034 at a $\psi'/\psi_{c,rep}$ of 4.0, which does not appear unreasonable. Of course, one must keep in mind that Equation 6.4 was obtained using data valid for $\psi'/\psi_{c,rep}$ less than about 2.5 and therefore, strictly speaking, can only be valid for this range.
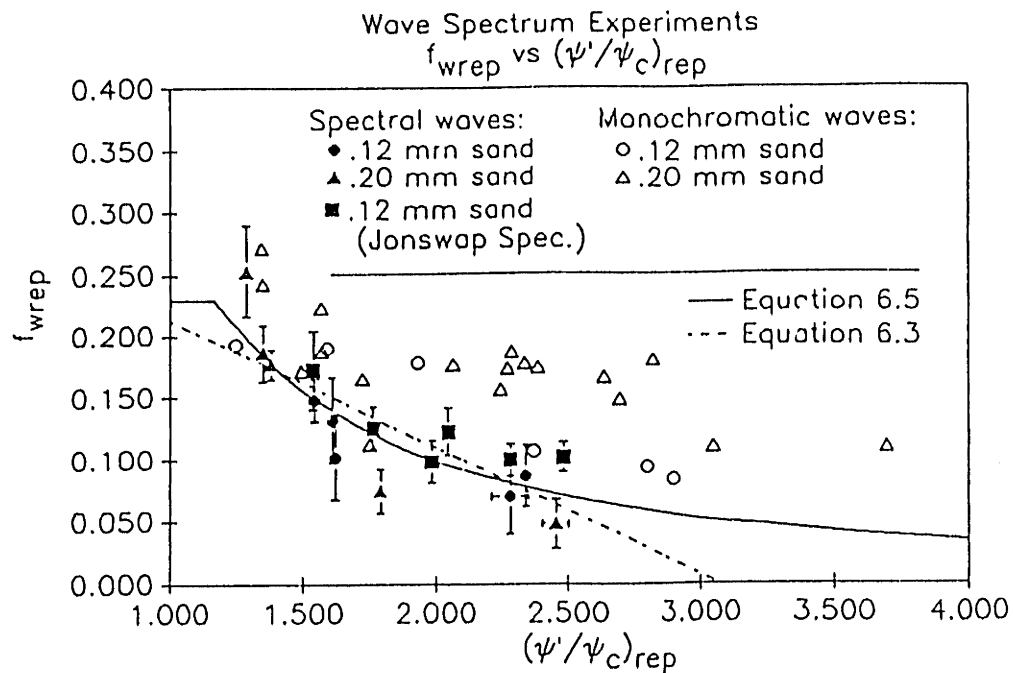
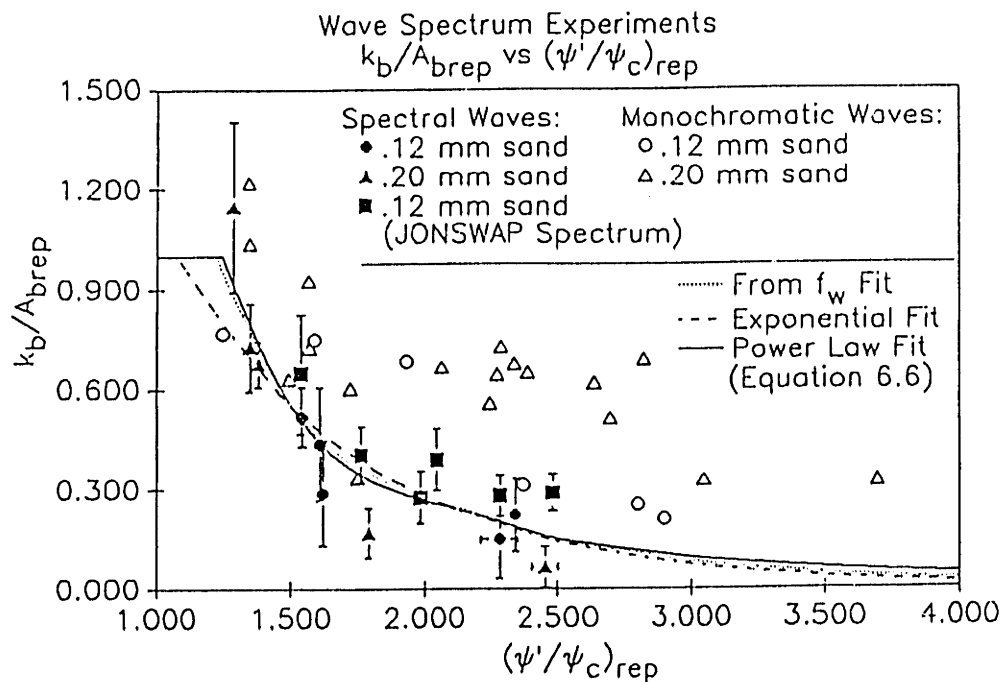Figure 6.12   FDB friction factor for spectral waves – Proposed relationship

Figure 6.13   FDB relative roughness for spectral waves – Proposed relationship

Once a relationship is defined to determine the friction factor in terms of wave intensity, it is desirable to also characterize the wave attenuation in terms of a bottom roughness. To accomplish this, we can use Equation 2.25, Grant and Madsen's relationship to relate friction factor to bottom roughness. However, the use of Equation 2.25 assumes the turbulent eddies in the bottom boundary layer to be scaled by the bottom roughness, k_b. If k_b/A_b is greater than 1, the excursion amplitude, A_b, becomes the length scale of the turbulent eddies. In this case, the friction factor must be constant and can be taken as .23, the value associated with a k_b/A_b of 1.0. Therefore, to appropriately model spectral wave attenuation, Equation 6.4 must be modified by incorporating the constant friction factor of .23 for k_b/A_b greater than 1.0. This modification, which was included in Figure 6.12, yields the proposed friction factor relationship:

$$f_w = \begin{cases} .23 & \text{for} \quad \psi'/\psi_{c,rep} < 1.17 \\ .293 \, (\psi'/\psi_{c,rep})^{-1.58} & \text{for} \quad \psi'/\psi_{c,rep} \geq 1.17 \end{cases} \tag{6.5}$$

To evaluate the accuracy of this relationship, the ratio of the predicted friction factor to the measured friction factor, $(f_w)_{pred}/(f_w)_{meas}$, was taken for all data points. The mean value standard deviation for this ratio were found to be 1.027 and .099, respectively. This indicates that Equation 6.5 can be used to estimate the spectral friction factor with a relative error of about 10 percent.

Next, since many coastal models use the relative roughness as an input parameter, it is desirable to define a separate empirical equation to represent that parameter. This was accomplished by converting all of the friction factor data to relative roughnesses using Equation 2.25 and fitting a curve to this data. Two curve fits were tested: a power law fit and an exponential fit. These two relationships are plotted against the relative roughness data in Figure 6.13 as the solid line (power law relationship) and

dashed line (exponential relationship). In addition, the curve fit for the friction factor data, transformed according to Equation 2.25, is plotted in this figure as the dotted line. Since, as is apparent in that figure, the empirical power law fit matches this transformed curve extremely well and is slightly more accurate than the exponential fit, it was considered to be the preferred alternative. Here, because of scaling argument summarized above, the $k_b/A_{b,rep}$ is taken to be 1.0 for values of $\psi'/\psi_{c,rep}$ that are less than 1.17. The resulting relationship is:

$$k_b/A_{b,rep} = \begin{cases} 1.0 & \text{for} \quad \psi'/\psi_{c,rep} < 1.17 \\ 1.549(\psi'/\psi_{c,rep})^{-2.54} & \text{for} \quad \psi'/\psi_{c,rep} \geq 1.17 \end{cases} \tag{6.6}$$

Use of this relationship to define the relative roughness, in addition to Equation 2.25, will provide friction factor estimates with an approximate accuracy of ± 10 percent.

7 CONCLUSIONS

In conclusion, the purpose of this thesis was to resolve a number of unresolved questions and problems that still remained after completion of the experimental study presented in Rosengaus (1987). In addition, the desire was to provide additional information regarding the use of existing dimensionless parameters and relationships to characterize wave/sediment interaction.

First, the questions and problems noted above, which mostly pertained to the experimental apparatus, included some limitations imposed by the wavemaker output capacity. These limitations were overcome by making adjustments to the wavemaker and by recalibrating the wavemaker system, as is discussed in Chapter 3. In addition, a sampling problem and a number of concerns related to the general accuracy of the data acquisition system required attention. These concerns were resolved by updating the sampling software and by completing a general accuracy analysis, which is also presented in Chapter 3. Therefore, it was determined that the experimental setup could be used to provide accurate experimental results that could be used to characterize wave/sediment interaction for a wide range of wave conditions.

Once accuracy of the experimental setup was verified, some more experiments were completed using the same .20-mm sand as for Rosengaus (1987). In addition, experiments were completed using a finer .12-mm sand. The associated experimental results were then analyzed to assist in quantifying relationships associated with:

1   Initiation of motion and ripple formation on an initially flat bed subjected to both monochromatic and spectral waves,

2   Geometry, height, and length of bedforms as a function of wave and sediment characteristics,

3   The equivalent hydraulic roughness of wave generated ripples, and the rate of dissipation of wave energy in the bottom boundary layer and corresponding wave attenuation.

To summarize, conclusions can be stated for the initiation of motion of sediment particles and characteristics of the developing bed, and characteristics of the fully developed bed, for which the relationship between bedform geometry and wave attenuation has been explored.

7.1 Initiation of Motion

Three separate initiation of motion conditions are notable. The first of these corresponded quite closely to that predicted by the Critical Shields Criterion for Initiation of Motion (ψ_c). In this case, the grain motion was observed at irregularities in the sediment bed. The second initiation of motion condition was that associated with bedform propagation, which occurred at values of ψ' that were slightly higher than ψ_c. Finally, a separate initiation of motion criterion was observed for regions of the sand bed that were perfectly flat. This condition was significantly higher than Shields Criterion and was not quantified.

7.2 The Developing Bed

The data obtained for the parameters characterizing the developing bed exhibited a wide scatter. However, these parameters for both the .12- and .20-mm sands, when plotted against ψ'/ψ_c , generally displayed similar developing bed characteristics and any differences between results for the two sands could not be verified because of the unavoidable subjectivity of the observations. Therefore, based on available data, the Relative Shields Parameter provides a good characterization of the bedform response for

fine sands. In addition, the spectral results were represented by making use of a representative monochromatic wave, as is clarified more in Section 7.3.2. Analysis showed that, in general, the spectral results corresponded favorably with the monochromatic results, indicating that the use of the representative monochromatic wave in this manner provides a reasonable characterization of spectral wave/sediment interaction for a developing bed.

7.3 The fully developed bed

7.3.1 Monochromatic Waves

As noted above, the purpose of the monochromatic wave experiments was to define relationships characterizing fully developed bedform geometry, and then use these relationships to determine the wave attenuation in terms of the hydraulic roughness of the sediment bed, from which a friction factor can be defined.

7.3.1.1 Bedform Geometry

To quantify bedform relationships, various bedform parameters were plotted against the Relative Shields Parameter. When plotted against ψ'/ψ_c, the data for the bedform parameters for the .12- and .20-mm sands, generally lined up on a single line, and were quite well represented by a linear curve fit. Review of these parameters for the monochromatic wave experiments revealed no distinct breakoff characteristics. In addition, the bedform geometry relationships proposed in Stefanick (1979), which account for the presence of a breakoff range, provided a relatively poor fit to the bedform geometry parameters.

Although Stefanick's relationships provided a relatively poor fit to the data when considering both the .12- and .20-mm sands, review of breakoff data plotted in

Stefanick (1979) revealed that the match could be slightly improved. This was done by allowing for different breakoff values for different bedform parameters. While the relationship for the breakoff for η/λ was the same as that proposed by Stefanick, his breakoff for η/A_b was modified by reanalyzing his data. Therefore, the relationship for η/A_b to be used when ψ'/ψ_c is greater than $(\psi'/\psi_c)_{bnab}$ was accordingly modified.

This summary above leaves us with two sets of relationships for characterizing the bedform geometry parameters of interest. First, the linear curve fits, which provide the best correlation with the data, are as follows:

$$\eta/A_b = .3365 - .0751(\psi'/\psi_c) \tag{7.1}$$

and

$$\eta/\lambda = .1904 - .0176(\psi'/\psi_c) \tag{7.2}$$

The second set of relationships for these parameters makes use of the two relationships for the breakoff values. First, for η/A_b, the breakoff value is defined by:

$$(\psi'/\psi_c)_{bnab} = 2.0S_*^{0.4} \tag{7.3}$$

Then, η/A_b is determined by:

$$\eta/A_b = \begin{cases} .22(\psi'/\psi_c)^{-.16} & ; \quad (\psi'/\psi_c) \leq (\psi'/\psi_c)_{bnab} \\ .56S_*^{.54}(\psi'/\psi_c)^{-1.5} & ; \quad (\psi'/\psi_c) > (\psi'/\psi_c)_{bnab} \end{cases} \tag{7.4}$$

For η/λ, the relationships are the same as those defined in Stefanick (1979). The breakoff is defined by:

$$(\psi'/\psi_c)_{bnl} = 1.85_*^{0.6} \tag{7.5}$$

and η/λ is determined by:

$$\eta/\lambda = \begin{cases} .16(\psi'/\psi_c)^{-.04} & ; \quad (\psi'/\psi_c) \le (\psi'/\psi_c)_{bnab} \\ .28S_*{}^{.59}(\psi'/\psi_c)^{-1.0} & ; \quad (\psi'/\psi_c) > (\psi'/\psi_c)_{bnab} \end{cases} \tag{7.6}$$

These relationships, while not as accurate as the linear curve fits, do account for a breakoff range. Accounting for a breakoff range is preferable since the existence of the breakoff range has been demonstrated by previous investigations of wave-generated bedforms and also is evident in the attenuation results of this study. In addition, the use of these equations provides the best overall physically reasonable model when we link attenuation, bottom roughness, and bedform geometry in a single quantitative model.

Additional bedform parameters that are normally not considered to be associated with the hydraulic bottom roughness include λ/A_b and the asymmetry, α. λ/A_b can be determined using the equations summarized above. The asymmetry, α, can be determined by the following relationship:

$$\alpha = .4482 + .0129(\psi'/\psi_c) \tag{7.7}$$

7.3.1.2 Wave Attenuation

As mentioned above, the wave attenuation results, expressed in terms of a friction factor, exhibited a breakoff. This breakoff was verified by review of some typical bedform profiles and was also shown to be reasonable when compared with data from Stefanick (1979). As previously noted, while the bedform parameters did not display the clear breakoff that showed up in the attenuation data, a reasonable explanation was found. Here, we maintain that, at the higher flow intensities associated with the

breakoff range, the crests of the ripples are rounded or shaved off. This phenomenon changes the hydrodynamics of flow in the bottom boundary layer and reduces the effectiveness of the ripples as energy dissipators.

To represent these attenuation results, a number of predictive relationships were compared. It was determined that the use of relationships developed by modifying those from Steřanick (1979) provided a reasonable fit to the data. Moreover, these relationships maintain a sound physical basis by accounting for the breakoff. Therefore, the proposed procedure for modeling the response of a sediment bed to wave agitation and associated wave attenuation makes use of Equations 7.3 through 7.6, listed above, to characterize the bedform geometry. Then, the relative bottom roughness for lower wave intensities can be determined using the following equation:

$$k_b/A_b = 23(\eta/A_b)(\eta/\lambda) \tag{7.8}$$

This equation is a simplified form of an equation originally proposed by Grant and Madsen (1982). Here, the original constant proposed by Grant and Madsen, 28, has been changed to 23 as was suggested by Rosengaus (1987). This modification provides an improved fit to the data. In addition, the effects of sediment transport have been neglected, implying that this relationship should only be used in cases of relatively low wave intensity (for, say, ψ'/ψ_c less than about 4.0). For higher flows, Equation 2.22, with the constant taken to be 23, may be used. Finally, the friction factor may be obtained by using Equation 2.25, Grant and Madsen's expression relating the friction factor to relative roughness, which is shown in Figure 2.4. Use of this model will predict the friction factor within an accuracy of ± 10 percent.

7.3.2 Spectral Waves

As for the monochromatic wave experiments, the primary goal of the spectral experiments was simply to obtain quantitative relationships characterizing bedform response to spectral wave agitation and the associated spectral attenuation due to bottom friction. Specifically, the desired objective was to verify that this task could be accomplished by making use of an equivalent monochromatic wave to characterize a wave spectrum. This equivalent wave is defined as a monochromatic wave that has the same horizontal bottom velocity and excursion amplitude as the respective root-mean-squared values for the wave spectrum. If this procedure is successful, attenuation relationships based on data from many monochromatic wave experiments could be applied to spectral attenuation. Therefore, the approach was to compare the monochromatic and spectral results when plotted against a representative Relative Shields Parameter.

7.3.2.1 Bedform Geometry

First, the spectral and monochromatic bedform geometry data were plotted against $(\psi'/\psi_c)_{rep}$ and analyzed. It was found that, while the data for nondimensional bedform height for the spectral experiments were relatively similar to that of the monochromatic experiments, the bedform steepness clearly differed, with the data generally falling below that of the monochromatic experiments. In addition, as for the monochromatic bedform data, no clear breakoff characteristic could be observed. Consequently, Stefanick's relationships could not be used to model the spectral data.

However, the spectral bedform data for the .12- and .20-mm sands, when plotted against $(\psi'/\psi_c)_{rep}$ generally fall on a single line. This implies that the use of a representative Relative Shields Parameter provides a good characterization of bedform

response to spectral wave agitation. Therefore, a number of empirical relationships were developed to represent the spectral bedform geometry.

These relationships, developed by making use of linear curve fits, are:

$$\eta/A_{brep} = .3357 - .0869(\psi'/\psi_c)_{rep} \tag{7.9}$$

and

$$\eta/\lambda = .1864 - .0136(\psi'/\psi_c)_{rep} \tag{7.10}$$

Values for λ/A_{brep} can be obtained from Equations 7.9 and 7.10 above. In addition, the spectral asymmetry, α, was quite similar to the monochromatic asymmetry and can be well represented by Equation 7.8.

7.3.2.2 Spectral Attenuation

The results presented in Rosengaus (1987) showed that the representative monochromatic wave could be used to characterize spectral bedform geometry in terms of commonly accepted bedform parameters. In addition, the use of this representative wave was also shown to successfully relate these bedform geometry parameters to the spectral wave attenuation. However, this result was based on experiments that were limited to wave conditions of relatively low intensity. Additional experiments completed, of higher wave intensity, have shown that the representative monochromatic wave can be used to separately characterize spectral bedform geometry and spectral wave attenuation in the same manner as used for monochromatic waves. However, these additional experiments have proved that the spectral bedform geometry cannot be related to the spectral wave attenuation. This fact became quite evident upon comparing the monochromatic and spectral friction factor data, from which it was clear that all spectral friction factors were clearly lower than the monochromatic friction

factors. Therefore, the spectral friction factor, defined in terms of a representative monochromatic wave, does not correlate with the monochromatic wave friction factors. In addition, no breakoff value was evident in the spectral attenuation data.

Since the spectral bedform data were generally lower than the corresponding monochromatic data, linear curve fits to the spectral bedform data were used to obtain predicted friction factors. However, these predicted friction factors still were not low enough to reasonably represent the spectral friction factor data. To further explore this, bedform profiles were inspected and compared to corresponding profiles for the monochromatic wave experiments. This comparison revealed that the ripple crests that are formed by spectral waves are more rounded (or shaved off) than their monochromatic counterparts. This rounding effect is attributed to the occasionally very large near bottom velocities that occur when a spectrum of many components propagates through shallow water. Basically, the rounded ripple crests change the hydrodynamics of the flow in the bottom boundary layer resulting in the lower spectral friction factors.

While the spectral experiments refuted any ideas of implementing a representative monochromatic wave to simultaneously model bedform geometry and spectral attenuation, a number of new conclusions were drawn from the spectral results. First, the spectral friction factor results, when plotted against $(\psi'/\psi_c)_{rep}$ for the .12-mm sand and .20-mm sand, generally fell on a single curve, again verifying the effectiveness of the Representative Shields Parameter for characterizing spectral wave/sediment interaction. In addition, experiments completed using the same spectrum but with different phases for all of the spectral components showed that the spectral attenuation characteristics for the experiments were independent of phase. Finally, the Pierson-Neumann (broad-banded) and JONSWAP (narrow-banded) spectral results also fell on a single curve. This indicates that the spectral attenuation characteristics are

independent of spectral shape. Thus, we expect that, if we hypothetically decrease the bandwidth of a wave spectrum towards zero, such that almost all of the spectral energy gets concentrated on a single frequency, the limit in terms of attenuation will not be the characteristics of a monochromatic wave. Instead, the spectral characteristics should be maintained. This lack of dependency of f_w on spectral shape also provides additional support for the explanation of the rounding effect, in which the dissipative characteristics of the spectrum are attributed to occasionally large near-bottom orbital velocities.

In summary, the success of the Representative Shields Parameter in characterizing spectral wave attenuation provides the opportunity to define a simple empirically based model for spectral wave attenuation. As opposed to the model for monochromatic wave attenuation, however, bedform geometry relationships cannot be related to $k_b/A_{b,rep}$, since the experimental results did not verify any relationship between these parameters. Therefore, it is apparent that η/A_b and η/λ are not enough to characterize the equivalent bottom roughness. The crest roundedness, which is not normally reported, plays a major role in the dissipation process. A relationship between bedform geometry and spectral relative roughness would require more research that is not included in the scope of this thesis.

Therefore, an empirical power law relationship is proposed for the friction factor in terms of the Representative Shields Parameter. This relationship is:

$$f_w = \begin{cases} .23 & ; (\psi'/\psi_c)_{rep} < 1.17 \\ .293(\psi'/\psi_c)_{rep}^{-1.56} & ; (\psi'/\psi_c)_{rep} \geq 1.17 \end{cases} \tag{7.11}$$

which will predict the friction factor within ± 10 percent. A relationship for the relative roughness, which is often assumed to be known for coastal computer models, was

determined by using a power law fit to the k_b/A_b data obtained by transforming experimental friction factor data using Equation 2.25. This relationship is:

$$\frac{k_b}{A_b} = \begin{cases} 1.0 & ; (\psi'/\psi_c)_{rep} < 1.17 \\ 1.549(\psi'/\psi_c)_{rep}^{-2.54} & ; (\psi'/\psi_c)_{rep} \geq 1.17 \end{cases} \tag{7.12}$$

7.4 Recommendations for Future Research

While the analysis of data for the .12- and .20-mm sands provided a tremendous amount of insight into wave/sediment interaction for a wide range of wave conditions, much more work is necessary. To gain a better understanding of the wave/sediment interaction in the coastal environment, additional analytical, experimental, and field-based research is essential.

For example, a number of analytical questions were raised by some of the experimental observations noted in this study. These pertain to the hydrodynamics of the flow in the turbulent bottom layer and its relationship to the the monochromatic ripple characteristics as delineated by the breakoff value. In addition, more study regarding the boundary layer hydrodynamics and its relationship to the ripple "roundedness" that was observed in the spectral bedform geometry is necessary. An in-depth analysis of the boundary layer hydrodynamics could also help to improve the understanding of the relationship between bedform geometry and the equivalent bottom roughness resulting in wave attenuation.

In the laboratory, a number of areas could use more investigation. One example is the developing bed and bedform response to changing wave conditions. Specific experiments designed for this purpose would help to characterize the bedform response. In addition to the developing bed, more study of the fully developed bed would be advantageous. For example, the spectral experiments completed used only five

components to represent a wave spectrum, which is an extremely coarse representation. Additional experiments with finer resolution of the frequency domain and spectral attenuation would be quite beneficial in verifying some of the conclusions noted in this study.

Again, one cannot overemphasize the importance of verification of the laboratory results in the field. Naturally, the field investigations related to the interaction of waves and bedforms are extremely difficult and quite expensive. However, since the purpose of characterizing the wave/sediment interaction is to apply the concepts to coastal problems, the benefits would be well worth the costs.

8 REFERENCES

Bagnold, R. A. 1946. Motion of waves in shallow water: Interaction between waves and sand bottom. *Proceedings of the Royal Society* (Ser. A) 187:1-15.

Biésel, F., F. Suquet. 1951. Les appareils générateurs de houle en laboratoire. *La Houille Blanche* 6(2):147-165.

Carstens, M. R., F. M. Nielson, H. D. Altinbek. 1969. Bedforms generated in the laboratory under oscillatory flow: Analytical and experimental study. U.S. Army Corps of Engineers, CERC Technical Memorandum No. 28.

Grant, W. D., O. S. Madsen. 1979. Combined wave and current interaction with a rough bottom. *Journal of Geophysical Research* 79(C4):1797-1807.

Grant, W. D., O. S. Madsen. 1982. Movable bed roughness in unsteady oscillatory flow. *Journal of Geophysical Research* 87(C1):469-481.

Hunt, J. N. 1952. Viscous damping of waves. *Le Houille Blanche* 7:836-842.

Ippen, A. T. (ed.) 1966. *Estuary and coastal hydrodynamics.* McGraw-Hill.

Jonsson, I. G. 1966. Wave boundary layers and friction factors. In *Proceedings 10th Conference on Coastal Engineering, ASCE,* 1:127-148.

Kajiura, K. 1968. A model of bottom boundary layer in water waves. *Bulletin of the Earthquake Research Institute* (University of Tokyo) 46:75-123.

Kamphuis, J. W. 1975. Friction factor under oscillatory waves. *Journal of the Waterways, Harbors and Coastal Division, ASCE,* 101(WW2):135-144.

Madsen, O. S. 1971. On the generation of long waves. *Journal of Geophysical Research* 76(36):8672-8683.

Madsen, O. S., W. D. Grant. 1975. The threshold of sediment movement under oscillatory waves: A discussion. *Journal of Sedimentary Petrology* 45(1):360-361.

Madsen, O. S., W. D. Grant. 1976. Sediment transport in the coastal environment. R. M. Parsons Laboratory, Department of Civil Engineering, MIT, Technical Report No. 209.

Madsen, O. S., W. D. Grant. 1977. Quantitative description of sediment transport by waves. Proceedings 15th Conference on Coastal Engineering. ASCE 2:1093-1112.

Rosengaus, M. R. 1987. Experimental Study on wave generated bedforms and resulting wave attenuation. Sc.D. Thesis, MIT.

Shore protection manual. 1977. U.S. Army Corps of Engineers, CERC.

Stefanick, T. A. 1979. A realistic model of wave attenuation due to bottom friction. M.S. thesis, MIT.